

Characterization of a PEM electrolyzer for ozone generation in ultrapure and drinking water applications

Dissertation

zur

Erlangung des Doktorgrades (Dr. rer. nat.)

der

Mathematisch-Naturwissenschaftlichen Fakultät

der

Rheinischen Friedrich-Wilhelms-Universität Bonn

vorgelegt von

Roman Grimmig

aus

Dresden

Bonn 2024

Angefertigt mit Genehmigung der Mathematisch-Naturwissenschaftlichen Fakultät
der Rheinischen Friedrich-Wilhelms-Universität Bonn

Gutachter/Betreuer: Prof. Dr. Helmut Baltruschat

Gutachter: Prof. Dr. Klaus Günther

Tag der Promotion: 30.09.2024

Erscheinungsjahr: 2024

"So eine Arbeit wird eigentlich nie fertig, man muss sie für fertig erklären, wenn man nach der Zeit und den Umständen das Möglichste getan hat."

Johann Wolfgang von Goethe

Abstract

The electrolytic *in situ* generation of oxidants is an increasingly widespread technique for producing sanitized and thus safe process water in ultrapure water distribution systems. In particular, the anodic production of ozone on functionalized electrodes is a commercially available option for providing pharmaceutical-grade water. The present work therefore investigates the use of a newly developed electrolyzer with a polymer electrolyte membrane (PEM) and lead dioxide (PbO_2) electrodes for drinking and ultrapure water treatment.

The selective analysis of electrolytically generated oxidizing agents or reactive oxygen species such as ozone (O_3), hydrogen peroxide (H_2O_2) and hydroxyl radicals ($\cdot\text{OH}$) is often impeded by cross-sensitivities of commonly used photometric assays. To account for these imperfections, a step-by-step procedure to consolidate different analytical methods was developed. Depending on the applied current density, different electrolytically generated species can be detected selectively and enable the observation that the electrolytic generation of ozone only increases significantly for current densities above 0.5 A cm^{-2} . In addition, the evolution of H_2O_2 only occurs in significant amounts in the presence of an organic impurity. The resulting, rapid decomposition of ozone *via* the peroxone process requires several equivalents of H_2O_2 , depending on the present amount of dissolved O_3 .

In order to provide a sensitive in- or on-line detection for ozone in ultrapure water, electrode materials based on Pt-functionalized ionomers were developed using a modified impregnation-reduction process. The metal loading on the sensor material was determined satisfactorily using a non-destructive approach by means of computed tomography (CT). Different synthesis conditions led to different sensor properties in terms of sensitivity and applicable concentration range. After evaluation of different models by an objective information criterion, the potentiometric sensor behavior is best described by a Langmuir pseudo-isotherm. On average, $2.9 \mu\text{g L}^{-1}$ of dissolved ozone was found as the detection limit for all sensor materials produced, which is comparable to complex reference analysis.

Extending the application range for PEM electrolysis to the drinking water sector was evaluated by exposing the analytic feed to different water hardness levels. The electroosmosis of water is a direct function of the current density and can be estimated at $95 \pm 2 \text{ mmol A}^{-1} \text{ h}^{-1}$. The transport rates of sodium, potassium, calcium and magnesium ions were modeled as a function of the current density and water hardness and were directly related to the ion mobility, independent of the water quality. Permeation leads to higher pH values of the catholyte within a few minutes and consequently to insoluble hydroxides and carbonates of the formerly

dissolved hardeners. The introduction of an auxiliary cathode in the anode compartment was able to reduce tap water cation permeation indiscriminately by $18 \pm 4 \%$.

The results show that the selected methods are suitable and directly applicable for the sensitive and selective detection of *in situ* produced disinfectants, in particular electrolytically generated ozone in the aqueous phase. An initial transfer of this PEM electrolyzer into the tap and drinking water environment is showcased the example of temporarily stagnant water with a constructive solution for suppressing unwanted ion crossover.

Zusammenfassung

Die *in situ* Erzeugung von Oxidationsmitteln durch Elektrolyseure ist eine zunehmend verbreitete Technik, um keimfreie und damit sichere Prozesswässer im Reinstwasserbereich herzustellen und energieeffizient zu lagern. Insbesondere die anodische Herstellung von Ozon an funktionalisierten Elektroden stellt dabei eine kommerziell verfügbare Option dar, um Wasser von pharmazeutischer Qualität bereitzustellen. In der vorliegenden Arbeit wird daher die Anwendung eines neu entwickelten Elektrolyseurs mit Feststoffelektrolyt (PEM) und Bleidioxid (PbO_2) Elektroden für die Bereiche der Trink- und Reinstwasseraufbereitung untersucht.

Die selektive Analytik von elektrolytisch erzeugten Oxidationsmitteln bzw. reaktiven Sauerstoffspezies wie Ozon (O_3), Wasserstoffperoxid (H_2O_2) und Hydroxylradikalen ($\cdot\text{OH}$) ist oft von Querempfindlichkeiten erschwert und wurde in ein schrittweises Verfahren überführt, welches die Querempfindlichkeiten zwischen den analytischen Verfahren berücksichtigt. Daraus können abhängig von der applizierten Stromdichte die elektrolytisch entstehenden Spezies gezielt erfasst werden, was die Beobachtung erlaubt, dass erst ab einer Stromdichte über 0.5 A cm^{-2} die elektrolytische Erzeugung von Ozon signifikant ansteigt. Zudem kann gezeigt werden, dass H_2O_2 im Reinstwasser erst in Gegenwart von organischen Verunreinigungen entsteht und der dadurch induzierte, schnelle Zerfall von Ozon konzentrationsabhängig unterschiedliche Äquivalente H_2O_2 erfordert.

Um eine empfindliche in- oder on-line Sensorik für Ozon im Reinstwasser darzustellen, wurden Elektrodenmaterialien auf Basis von Pt-funktionalisierten Ionomeren über ein modifiziertes impregnation-reduction-Verfahren entwickelt. Die Metallbeladung auf dem Sensormaterial kann hierbei zufriedenstellend über einen zerstörungsfreien Ansatz aus der Computertomographie (CT) ermittelt werden. Durch verschiedene Synthesebedingungen können verschiedene Sensoreigenschaften hinsichtlich Empfindlichkeit und nutzbarem Konzentrationsbereich erreicht werden. Das Sensorverhalten wird nach Evaluation verschiedener Modelle und einem objektiven Informationskriterium am ehesten gemäß einer Langmuir-Pseudoisotherme beschrieben. Die Nachweisgrenze für Ozon liegt im Mittel über alle hergestellten Sensormaterialien bei $2.9 \mu\text{g L}^{-1}$, was in der Größenordnung von aufwändiger Referenzanalytik liegt.

Eine Erweiterung der Anwendung PEM-Elektrolyse für den Trinkwasserbereich wurde unter Verwendung verschiedener Wasserhärten im analytischen Zufluss realisiert. Die für die Anwendung relevante Elektroosmose von Wasser stellt eine direkte Funktion der Stromdichte dar und kann auf $95 \pm 2 \text{ mmol A}^{-1} \text{ h}^{-1}$ beziffert werden. Die Transportraten von Natrium-, Kalium-, Calcium- und Magnesiumionen wurden in Abhängigkeit der Stromdichte und Wasserhärte modelliert und konnten dabei unabhängig von der Wasserqualität in einen

direkten Zusammenhang mit der Ionenbeweglichkeit gebracht werden. Durch Permeation entstehen kathodenseitig innerhalb weniger Minuten höhere pH-Werte und in dessen Folge unlösliche Hydroxide und Carbonate von Härtebildnern. Die Einführung einer zusätzlichen Kathode im Anodenraum konnte die Permeation von wassertypischen Kationen um $18 \pm 4 \%$ verringern.

Die Ergebnisse zeigen, dass die gewählten Methoden unmittelbar geeignet sind, um *in situ* hergestellte Desinfektionsmittel, insbesondere elektrolytisch entstehendes Ozon in der wässrigen Phase empfindlich und selektiv zu erfassen. Ein erster Transfer dieses PEM-Elektrolyseurs von der Reinstwasser- in die Leitungs- und Trinkwasserumgebung ist am Beispiel von zeitweilig stehenden Wässern präsentiert und zeigt eine konstruktive Lösung auf, die unerwünschte Ladungsträger aus Trinkwasser zurückhält.

Eidesstattliche Erklärung

Hiermit erkläre ich, dass diese Dissertation von mir selbst und ohne unerlaubte Hilfe angefertigt wurde. Es wurden keine anderen als die angegebenen Hilfsmittel benutzt. Ferner erkläre ich, dass die vorliegende Arbeit an keiner anderen Universität als Dissertation eingereicht wurde.

Roman Grimmig

Table of Content

Chapter 1: Introduction	1
1.1 Hygienic preparation of drinking and ultrapure water	1
1.2 Ozone in ultrapure water production	6
1.3 Ozone production for ultrapure water production and storage.....	8
1.4 Electrolytic ozone production for ultrapure water production and storage	10
1.5 Ozone detection in the context of process analysis.....	16
1.6 Objectives.....	20
1.7 Thesis.....	22
Chapter 2: Challenges in the determination of reactive oxygen species evolving during PEM water electrolysis for in situ ozone production.....	23
Abstract:	24
2.1 Introduction.....	25
2.2 Materials and methods	28
2.2.1 Experimental setup	28
2.2.2 Analytical procedures.....	29
2.2.3 ORP measurements	31
2.3 Results and Discussion	32
2.3.1. Evaluation of the analytical performance of colorimetric ROS determination methods and their cross-sensitivities	32
2.3.2 ROS evolution during PEM electrolysis.....	37
2.3.3 Correlation of ORP signals with ROS concentrations.....	41
2.4 Conclusion.....	43
Chapter 3: Evaluating Platinum-Based Ionic Polymer Metal Composites as Potentiometric Sensors for Dissolved Ozone in Ultrapure Water Systems	45
Summary of the publication:	46
Chapter 4: Operating an ozone-evolving PEM electrolyser in tap water: A case study of water and ion transport	49
Summary of the publication:	50

Chapter 5: Discussion and Conclusion	53
5.1 Discussion	53
5.2 Conclusion.....	56
Bibliography	57
Annex.....	i
Paper: Evaluating Platinum-Based Ionic Polymer Metal Composites as Potentiometric Sensors for Dissolved Ozone in Ultrapure Water Systems	i
Paper: Operating an ozone-evolving PEM electrolyser in tap water: A case study of water and ion transport.....	xv

Chapter 1: Introduction

Each chapter and published paper that is part of this work provides an individual introduction and discussion section that puts the results reported in the respective paper in context with the literature. Therefore, no exhaustive literature survey is given in this section of the thesis to avoid redundancies.

At this point of the thesis, it is useful to put the present work into its application-related context of ultrapure water production and storage.

1.1 Hygienic preparation of drinking and ultrapure water

‘Trinkwasser ist das wichtigste Lebensmittel, es kann nicht ersetzt werden.’

Translation: ‘Drinking water is the most important foodstuff, it cannot be replaced.’

With these words the German standard for centralized drinking water supply introduces its guiding principles for the requirements for water supply systems [1]. Although the supply of potable water is almost as old as mankind, a conscious hygienic treatment of water does not have such a long history. It is documented that sand filtration of water and subsequent treatment with charcoal led to a significant improvement in water quality and was therefore applied from 500 BC until at least 1500 AD as the main treatment [2,3]. Other practices to achieve acceptable water quality was exposure to sunlight or boiling and subsequently storing the water in pots made of metals such as copper, iron and silver with an antimicrobial effect [4,5]. And yet it was not until the 19th century that biological substances in water were observed and linked to negative effects on physical health [6]. Later on, this led to purification and drinking water treatment plants which can produce tap water in our present understanding of tap water quality [7]. It was only comparatively late that the specific physical, chemical and biological requirements for drinking water quality were laid down in a binding form, e.g. in the Drinking Water Ordinance (German: Trinkwasserverordnung, TrinkwV) in 1975 as an example of a national standard [8].

Although drinking water provided today is of absolutely safe quality for human consumption, due to technological development increasing quality requirements for industrial have emerged over the years in which the quality of ordinary drinking or tap water is insufficient in terms of purity, and therefore require ultrapure water (UPW) [9].

A prominent application for UPW can be found in the pharmaceutical industry, where a special water quality and constitution is demanded compared to tap water [10]. In order to manufacture

medical products of a reliable quality, strict limits apply for chemical and biological substances in the used water. In addition to international standards, there are also various pharmacopoeias worldwide, depending on the area of responsibility and market, which determine and define the specific limit values for critical water quality parameters. In the *Pharmacopoeia Europaea* (Ph. Eur.), the pharmacopoeia that is binding for Europe, the highest water qualities are purified water denoted *aqua purificata* (AP) and water for injection (WFI) denoted *aqua ad injectabilia* [11]. In the United States, the qualities in their pharmacopoeia are defined by the associated standard test method (ASTM) for purified water ASTM D1193. A supra-regional ISO standard sets similar limit values [12–14] (see Table 1-1).

Table 1-1. Critical water parameters of internationally differing definitions for ultrapure water qualities. The two highest ultrapure water qualities of each UPW definition are compared to the tap water quality provided by the German Drinking Water Ordinance (TrinkwV). Empty cells refer to non-listed parameters, a dash (-) represents a listed, unspecified parameter.

Regulation	TrinkwV	Ph. Eur.		ASTM D1193		ISO 3696	
Water type	Drinking water	WFI	AP	Type I	Type II	Grade 1	Grade 2
pH	6.5 – 9.5	-	-	-	-	-	-
Conductivity / $\mu\text{S cm}^{-1}$	2,790	1.1	4.3	0.056	1.0	0.1	1.0
HTC / CFU mL^{-1}	100	0.1	100	0.01	0.1		
Absorbance at 254 nm (1 cm optical path length) / a.u.						0.001	0.01
Endotoxins / E.U. mL^{-1}		0.25		0.03	0.25		
TOC / $\mu\text{g L}^{-1}$	‘without abnormal change’	500	500	10	50		
Oxidizable matter / mg L^{-1}							0.08
Heavy metals (e.g. Pb) / mg L^{-1}	0.01		0.1				
Silicon (SiO_2) / mg L^{-1}	1			0.003	0.003	0.01	0.02
Residue after evaporation / mg kg^{-1}						-	1

In this context, several ordinances refer to similar water quality criteria, but are described with different approaches using varying physico-chemical parameters. For instance, the TrinkwV, Ph. Eur. and ASTM require a heterotrophic cell count (HTC), quantified in colony forming units (CFU) for microbial pollution and partially even a distinct endotoxin analysis, numbered as endotoxin units (E.U.). In contrast to that, the ISO standard uses a spectroscopic value that non-specifically detects organic and potentially viable impurities. For the highest water qualities, the individual pollution with heavy metals is not resolved to actual concentrations but condensed to non-specific sum parameters such as conductivity or the evaporation residue. Dissolved and charged particles contribute to the measurable conductance by their individual concentration, charge and ion mobility in the water, and thus form a macroscopically measurable sum parameter for the mineral content. The 'evaporation residue' can be understood as a conceptually related parameter for the mineral content of pharmaceutical water of the respective quality, which (here deliberately neglecting many other constituents such as dissolved organic compounds) already hints at the conventional treatment method for this type of water.

Historically, the thermal treatment of water by (sometimes multiple) distillation was the favored method of simultaneous purification and water disinfection. However, due to the high heat capacity of water, distillation is an energy- and cost-intensive form of hygienic treatment, especially on an industrial scale. As a result, alternative preparation processes for ultrapure water were developed and have proven effective, involving cold-acting, mostly oxidative disinfectants [15–17]. Such cold-produced and stored ultrapure water has to be adequately protected against contamination to counteract the formation and growth of bacteria and biofilms. The latter impurity poses a particular risk to the water quality as it consists of a resistant form of accumulated microorganisms and their metabolites [18–21].

A distinction is often made between passive and active measures to protect such UPW storage systems against contamination, with the passive one being taken as a discontinuous measure [10]. After the use of suitable disinfectant chemicals, residuals are rinsed out before the production of ultrapure water can be resumed. As an alternative, active measures protect against microbial contamination and are installed and planned as a routine measure. The aim is to achieve a permanent and reliable reduction in microbial growth and the removal of other organic impurities.

Potential oxidants that may serve as cleaning agents are listed in Table 1-2 below.

Table 1-2. Commonly used oxidants and their respective standard electrode potentials in aqueous medium. Values taken from [22,23]. The figure to the right visualizes the potentials of all reactions. Suitable oxidants for the UPW preparation are only comprised of hydrogen and oxygen and are highlighted in red.

Oxidizer	Reduction reaction	E° / V		
Fluorine	$F_2(g) + 2H^+ + 2e^- \rightarrow 2HF$ $F_2(g) + 2e^- \rightarrow 2F^-$	3.05	3.0	● F_2 / F^-
Hydroxyl radical	$\cdot OH + H^+ + e^- \rightarrow H_2O$	2.73		● $\cdot OH / H_2O$
Sulfate radical anion	$SO_4^{\bullet-} + e^- \rightarrow SO_4^{2-}$	2.60		● $SO_4^{\bullet-} / SO_4^{2-}$
Ferrate	$FeO_4^{2-} + 8H^+ + 3e^- \rightarrow Fe^{3+} + 4H_2O$	2.20	2.5	● FeO_4^{2-} / Fe^{3+}
Ozone	$O_3(g) + 2H^+ + e^- \rightarrow O_2(g) + H_2O$	2.08		● O_3 / O_2
Peroxodisulfate	$S_2O_8^{2-} + 2H^+ \rightarrow 2SO_4^{2-}$	2.01		● $S_2O_8^{2-} / SO_4^{2-}$
Hydrogen peroxide	$H_2O_2 + 2H^+ + 2e^- \rightarrow 2H_2O$	1.76		● H_2O_2 / H_2O
Permanganate (a)	$MnO_4^- + 4H^+ + 3e^- \rightarrow MnO_2(s) + 2H_2O$	1.67	2.0	● MnO_4^- / MnO_2
Hydroperoxyl radical (a)	$HO_2^{\bullet} + 3H^+ + 3e^- \rightarrow 2H_2O$	1.65		● HO_2^{\bullet} / H_2O
Permanganate (b)	$MnO_4^- + 8H^+ + 5e^- \rightarrow Mn^{2+} + 4H_2O$	1.51		● MnO_4^- / Mn^{2+}
Hydroperoxyl radical (b)	$HO_2^{\bullet} + H^+ + e^- \rightarrow H_2O_2$	1.44		● HO_2^{\bullet} / H_2O_2
Dichromate	$Cr_2O_7^{2-} + 14H^+ + 6e^- \rightarrow 2Cr^{3+} + 7H_2O$	1.36	1.5	● $Cr_2O_7^{2-} / Cr^{3+}$
Chlorine	$Cl_2(g) + 2e^- \rightarrow 2Cl^-$	1.36		● Cl_2 / Cl^-
Manganese dioxide	$MnO_2 + 4H^+ + 4e^- \rightarrow Mn^{2+} + 2H_2O$	1.23		● MnO_2 / Mn^{2+}
Oxygen	$O_2(g) + 4H^+ + 4e^- \rightarrow 2H_2O$	1.23		● O_2 / H_2O
Bromine	$Br_2(l) + 2e^- \rightarrow 2Br^-$	1.07		● Br_2 / Br^-

Oxidative processes are often used to reduce a possible organic or microbial pollution by an attempted mineralization. Consequently, remaining hydrocarbons are anticipated to be fully converted to water and carbon dioxide molecules.

By means of ozonation, unsaturated compounds react with the ozone molecule (Criegee's reaction) and form a molozonide (primary ozonide) intermediate, leading to a carbonyl and carbonyl oxide [24,25], as indicated in Fig. 1-1.

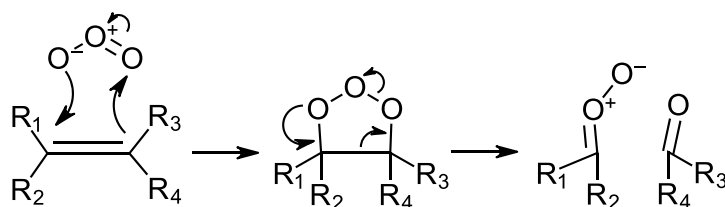
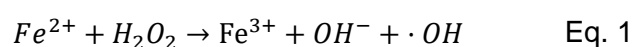


Fig. 1-1. Reaction pathway of unsaturated compounds with ozone. In a 1+3 cycloaddition, the intermediate molozonide is formed. The subsequent retro 1+3 cycloaddition leads to carbonyl and the carbonyl oxide molecules (Criegee intermediates). Own drawing, adapted from [24].

The carbonyl oxide molecule can subsequently undergo reactions in a broad variety of different reaction pathways [26].

The oxidation potential is often used to characterize the oxidative capability of these partially radical and short-lived compounds. The selection in Table 1-2 shows that many of the oxidative compounds with a high reduction potential (= high oxidation potential towards other compounds) are either not intended for use in the treatment of ultrapure or drinking water – due to the presence of heavy metals and other heteroatoms besides oxygen – or are of little technical use due to their short-lived nature. For instance, hydroxyl radicals ($\cdot\text{OH}$) show a lifespan in the range of nanoseconds [27] which makes it necessary to locally produce them *in situ* by means of e.g. Fenton's reaction [28,29] (Eq. 1).



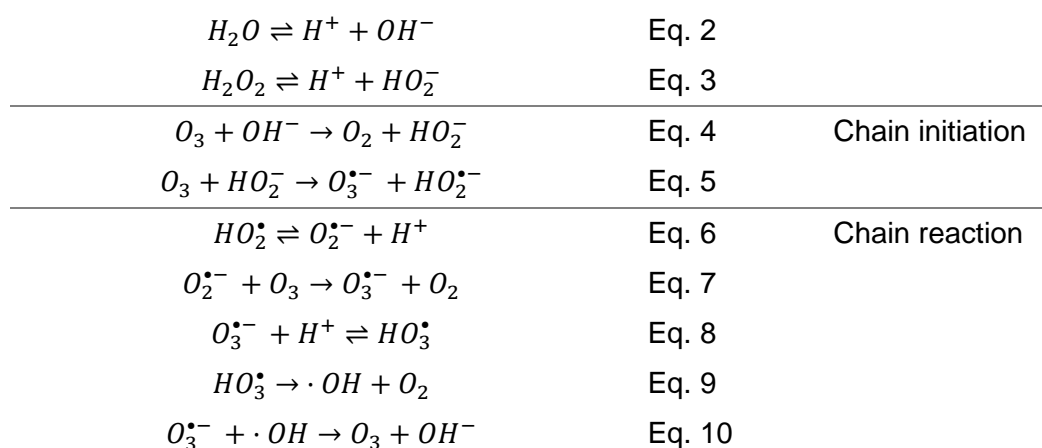
The high standard potential for $\cdot\text{OH}$ ($E^0 = 2.73 \text{ V}$) is due to the way standard potentials are obtained, i.e. a concentration of 1 mol/L, a temperature of 298.15 K and 1013.25 mbar pressure [30] and allows for a relative comparison. However, on boron-doped diamond electrodes at high current densities, the steady-state concentration for electro-generated $\cdot\text{OH}$ is only in the range of 10^{-5} mol / L [31]. With this adjustment, the Nernst equation yields a potential of 2.4 V, which is similar to the standard potential obtained from thermodynamic data for $\cdot\text{OH}$ formation of 2.38 V [32].

In the application of ultrapure water treatment and storage, some of the stable chemical compounds are often not compatible with the requirements specified in the pharmacopoeias. The most obvious reason is using unsuitable compounds that would be detected *via* the resulting conductivity of the water. Consequently, oxidizing agents purely based on hydrogen and oxygen are favored. Ozone (O_3) is an effective disinfectant of increasing importance, as it combines a high oxidizing power with a technical feasibility.

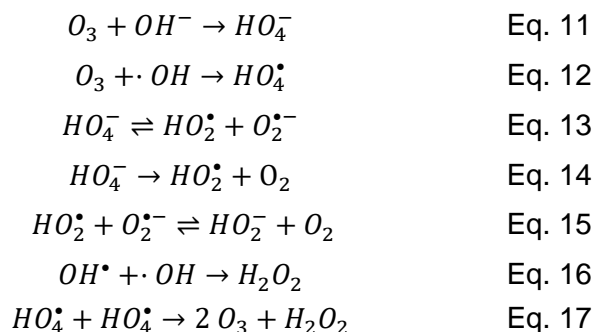
1.2 Ozone in ultrapure water production

Dissolved ozone is particularly suitable and interesting as an oxidizing agent as it is an unstable compound despite mesomeric stabilization. Depending on the conditions, ozone as the triatomic allotrope of oxygen can decompose into the diatomic molecule. While a half-life of 72 h is found for gaseous ozone, the half-lives in the aqueous phase at pH of approx. 7 are reported to be in a range of 10 to 60 minutes [33]. This pH range is of particular relevance for ultrapure water treatment, as the absence of impeding impurities is required in this environment.

In contrast to neutral media, a significant extension of the half-life up to 8 hours can be achieved in acidic media at pH 2 [34]. On the other hand, an alkaline environment leads to a significant reduction in the half-life (100 ms at pH 12 [35]), which provides an indication of the reaction mechanism underlying ozone decomposition and – in a subsequent approach – can be well described via the peroxone process [36–38]:



It has to be noted that the initiation reaction of ozone with OH^- (Eq. 2) obscures that other adducts known from the literature may occur [37,39–41]:



From Eq. 2 it can be easily seen that the pH value and thus the concentration of hydroxide ions is the main cause for the decomposition reaction of ozone and thus also for the observed

periods of stability in aqueous phase. In an ideal ultrapure water (and therefore the absence of impurities) the concentration of hydroxide ions is limited to autoprotolysis.

By adding hydrogen peroxide, its subsequent deprotonation (Eq. 3) can also specifically initiate the chain reaction by means of the well-known peroxone process (Fig. 1-2).

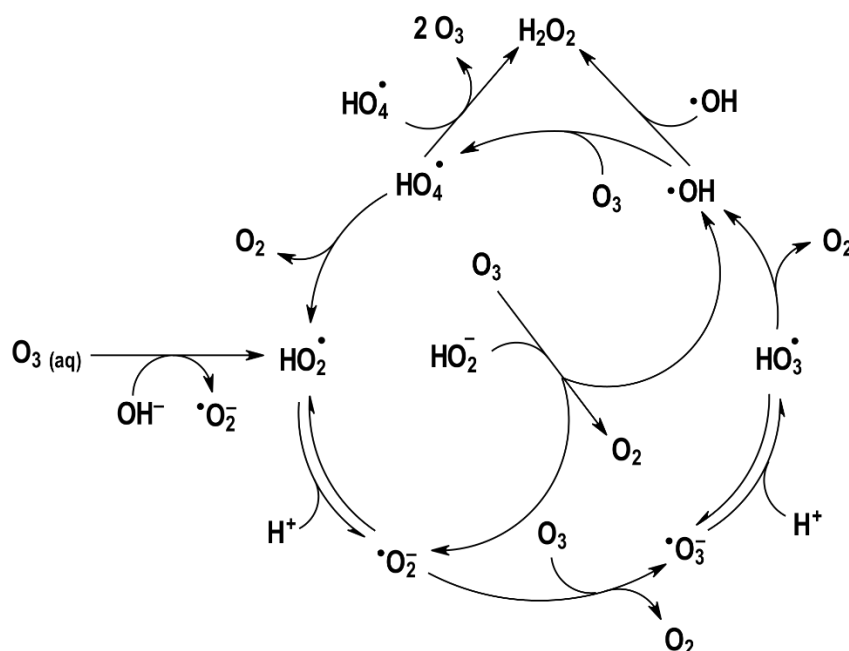


Fig. 1-2. Non-exhaustive scheme of ozone decay caused by hydroxide ions (OH^-) and hydroperoxide ions (HO_2^-) according to [36,42–45]. Diatomic oxygen and hydrogen peroxide can be identified as the main degradation by-products resulting from ozone decay.

As a result of the chain reaction, a large number of radical intermediates is formed, which eventually react to diatomic oxygen. $\cdot OH$ is also formed as an intermediate, which can interact as a potent reactive oxygen species (ROS) with organic pollutants itself or – during the reaction termination (Eq. 16) – take part in reactions forming hydrogen peroxide.

With $70 \text{ M}^{-1} \text{ s}^{-1}$, the rate constant of the reaction of O_3 with OH^- (Eq. 2) is considerably lower than for the reaction with HO_2^- (Eq. 3, $k = 2.8 \cdot 10^6 \text{ M}^{-1} \text{ s}^{-1}$) [45], which is why the reaction with hydrogen peroxide is primarily used as a deliberate *in situ* generation of hydroxyl radicals and therefore ozone is not necessarily used as the intended oxidant, but rather as a reactant. When not ozone itself acts as the oxidizing molecule (direct ozonation), but a decomposition product of ozone, this is referred to as indirect ozonation.

1.3 Ozone production for ultrapure water production and storage

Two different methods have been established for the production of ozone as an oxidizing and disinfecting agent, particularly for ultrapure water applications. One well-known method is silent electrical discharge. In this process, oxygen or an oxygen-containing gas such as air is passed between two electrodes, with at least one of the electrodes being covered by a dielectric [46,47] (Fig. 1-3).

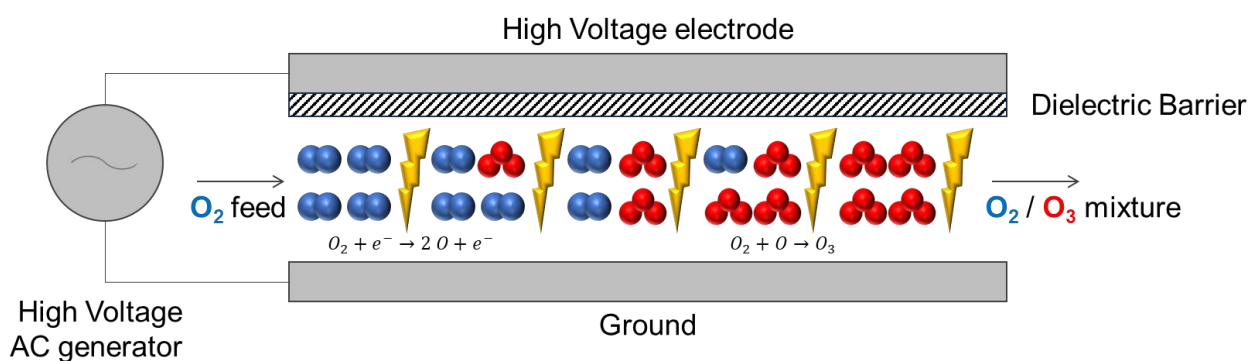
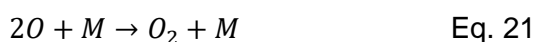
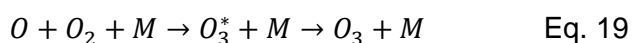


Fig. 1-3. Schematic structure and function of an ozone generator based on the principle of silent electrical discharge (own drawing, adapted from [48]).

Applying a high-frequency voltage source enables charge exchange by means of microdischarge channels. In a simplified model, the temporarily high density of electrons in the discharge gap between the electrodes ensures the initial reaction with oxygen, which subsequently leads to the formation of ozone [49–51]:



M = assisting collision partner: O , O_2 , O_3 , electrode walls

In the high-frequency field, molecular oxygen dissociates into oxygen atoms (Eq. 18), which can subsequently react with another oxygen molecule and a suitable impact partner to form ozone (Eq. 19), which is the actual formation reaction of ozone. In this part of the reaction the generated and excited O_3^* molecule is subjected to energetic stabilization. This energy is absorbed by the M molecule and releases heat into the system which is the main cause for the introduction of a cooling system. However, atomic oxygen is also able to decompose existing ozone molecules into diatomic oxygen molecules (Eq. 20) without the assistance of

another collision partner, consequently reducing the ozone yield. Single oxygen atoms can react with a collision partner to eventually form diatomic oxygen (Eq. 21) and may not proceed to any further reactions with diatomic oxygen to form ozone. Hence, when operating the ozone generator, excessive formation of dissociated oxygen molecules needs to be avoided in order to reach a satisfactory ozone yield (Eq. 22).

In the presence of other gas molecules apart from oxygen, decomposition reactions occur in a similar way, especially when using pressurized, ambient air containing only 21% oxygen and 78% nitrogen. The reaction sequence leads to the formation of nitrogenous by-products such as nitrous oxide (N_2O) and nitrogen monoxide (NO), where the latter can be oxidized to even higher oxidation levels in the presence of ozone and oxygen atoms [49,52].

Ozone production by means of silent electrical discharge is the most common method for synthesizing sufficient quantities of ozone with relatively low energy input (9 – 20 kWh kg⁻¹ O₃ [53], compared to 40 – 80 kWh kg⁻¹ electrolytically produced O₃ [54]). Depending on the type of supplied gas flow, weight percentages between 3 % (based on conventional compressed air) and 18% (based on pure oxygen) can be achieved in the exhaust air flow [46].

In the presence of air humidity or by introducing the exhaust gases containing ozone and nitrous compounds into water, acidic compounds such as nitrous and nitric acid are formed. To avoid these acidic compounds, ozone generation for ultrapure water disinfection by means of silent electrical discharge should only be considered, when an oxygen generator (i.e. based on pressure swing adsorption [55]) is implemented as part of the system.

1.4 Electrolytic ozone production for ultrapure water production and storage

The second method to produce ozone as an oxidizing and disinfecting agent is the electrolytic ozone generation, which can be adopted to provide ozone *in situ* from the process water itself. In this application of water electrolysis, the anodic oxygen evolution reaction (OER) (Eq. 23) is accompanied by the electrochemical ozone production (EOP), which occurs in considerable quantities (Eq. 24) [42,56,57].



The formation of diatomic oxygen is favored over the formation of ozone at the anode. Using a catalytic material that provides a sufficient overvoltage for oxygen generation therefore has an essential effect on ozone generation [58]. Another advantageous property of a suitable anode material providing a high electrical conductivity is chemical resistance to the *in situ* generated oxidizers and the resulting H^+ concentration (locally acting as acid). This can be achieved by the production of thin catalytic layers where an anode material is applied onto a suitable and partially porous carrier material as a dimensionally stable anode (DSA) in order to create a large electrochemical active surface. In this setup the electrode material will not be consumed as a bulk material. (Fig. 1-4).

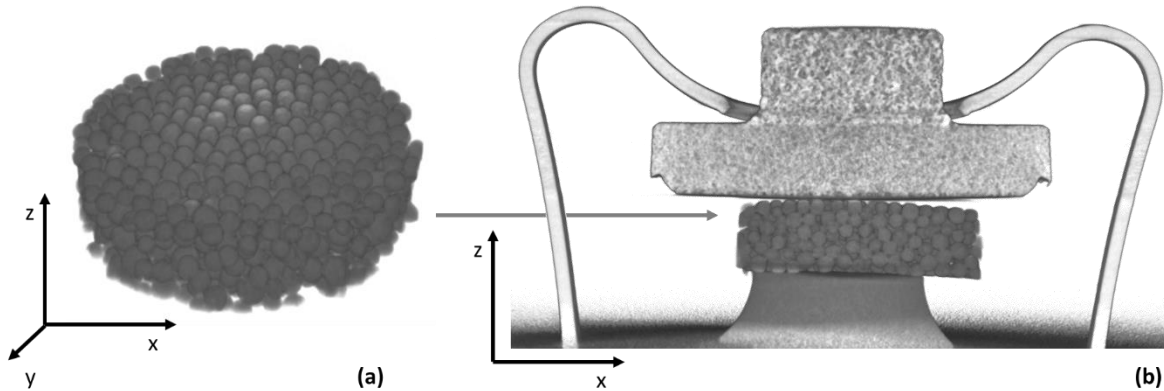


Fig. 1-4. (a) Computed tomography of a dimensionally stable anode (DSA) intended for ozone evolution (diameter approx. 5.2 mm) with a porous structure, isometric view. **(b)** Computed tomography of the DSA assembled to a functional with a porous cathode, cross section.

Suitable and widely discussed anode materials that were identified in the literature are platinum [58–60], PbO₂ ([9,16,68,58,61–67], boron-doped diamond electrodes (BDD) [31,69–74] and modified SnO₂ [58,75,76]. Platinum was primarily used as an ozone-evolving anode material due to its high overvoltage for oxygen until the early 1980s, when significantly higher current efficiencies of BDD and modified SnO₂ were documented [54]. The current efficiency (Faradaic efficiency) describes the yield of the electrochemically formed target compound. For electrolysis with the intention of ozone production, this equals the ratio of all charges that have contributed to the formation of ozone molecules $Q_{target\ molecule}$ in relation to the total charge that has passed (Eq. 26).

$$current\ efficiency = \frac{Q_{target\ molecule}}{Q_{total}} \quad Eq. 26$$

Since the amount of flowed charge is proportional to the amount of substance produced (Faraday's Law Eq. 27, with $F = 96485\ mol/C$, $C = \text{Coulomb}$), the current efficiency for the electrolytic production of ozone from the $z = 6$ electron process (Eq. 24) can also be described directly by the current I and experimental time (Eq. 28 and 29).

$$Q_{target\ molecule} = n * z * F \quad Eq. 27$$

$$Q_{total} = I * t \quad Eq. 28$$

$$current\ efficiency = \frac{n(O_3) * 6 * F}{I * t} \quad Eq. 29$$

Whereas only current efficiencies of 0.5 % were observed for platinum [58] at room temperature, significantly higher values of up to 21 % were observed for PbO₂ [61,62] and even up to 30 % for BDD electrodes [77]. The degree of doping with boron during production plays a particularly important role, as this can reduce the resistance of the usually insulating substrate from $10^{14}\ \Omega\ cm$ down to $10^{-3}\ \Omega\ cm$ ($10^{20}\ B\ cm^{-3} = \text{molar ratio boron to carbon } 0.1 - 5.0\ \%$) [77–80]. However, the high boron content is known to result in high mechanical stresses in the diamond matrix, which can lead to weakening on the electrode substrate and significantly reduce lifetime due to spalling. Similar to the other materials, SnO₂ as an anode material also shows high current yields in mineral acids, which can be increased to up to 36% by doping with antimony and cobalt [58,76,81]. However, as the materials were not stable over time and disintegrated, their use in ultrapure water is not considered.

Currently, PbO₂ is the favored anode material in electrochemical ozone generators. In addition to its comparatively simple production and high chemical stability, this material provides both a high electrical conductivity and overvoltage for oxygen, making it suitable as a catalyst

[82,83]. A distinction is made between the orthorhombic α -PbO₂ and the tetragonal β -PbO₂ (Fig. 1-5).

In the α -phase, PbO₂ crystallizes in an orthorhombic structure and has a significantly lower current yield for ozone production than the β -phase with its rutile structure [58]. Subsequently, in order to obtain the preferred β -PbO₂, synthesis parameters are specifically varied during electrochemical deposition from acidic solution [83,84]. To optimize adhesion to an electrode substrate and thus ensure long-term ozone production, certain dopants such as fluoride anions or Fe³⁺ can be used during synthesis of the lead dioxide layer [85].

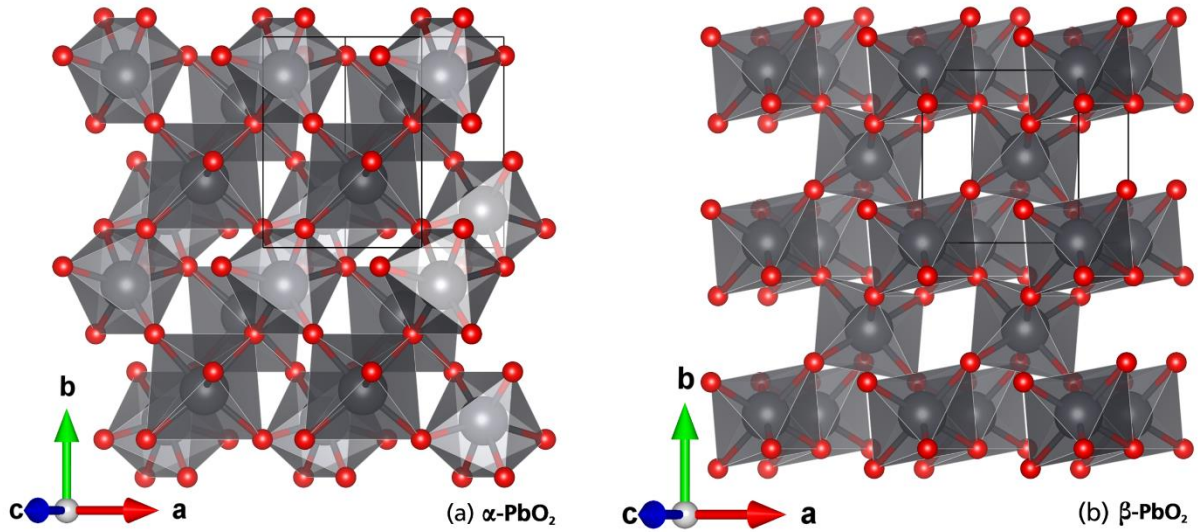
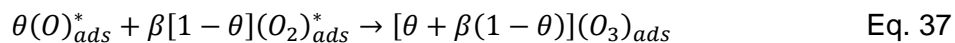
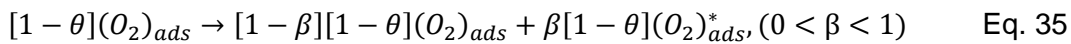
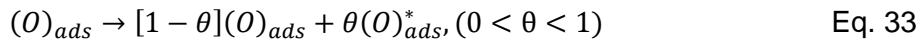
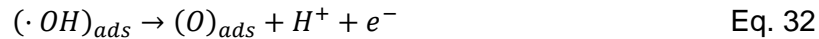
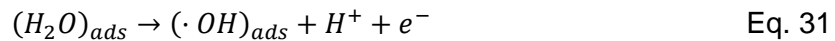


Fig. 1-5. Crystal structures of the ozone-generating PbO₂ phases visualized with VESTA [86]. **(a)** The α -phase of PbO₂ (Scrutinyite, COD 9009091 [87]) crystallizes in the orthorhombic system (space group Pbcn) with the lattice parameters $a = 4.97 \text{ \AA}$, $b = 5.95 \text{ \AA}$, $c = 5.50 \text{ \AA}$, $Z = 4$. **(b)** β -PbO₂ (Plattnerite, COD 9014175 [88]) crystallizes in the tetragonal lattice (space group P4₂/mmn) with the lattice parameters $a = 4.91 \text{ \AA}$, $c = 3.38 \text{ \AA}$, $Z = 2$.

Electrochemical ozone production on PbO₂ surface takes place according to the following, reaction scheme [43,63,64,89] (Eq. 30 - 38).



In a first, rate-determining step, water adsorption occurs on the surface of the catalytic β -PbO₂ layer and leads to the subsequent formation of adsorbed hydroxyl radicals (Eq. 31), which are further oxidized to adsorbed oxygen atoms (Eq. 32). A certain proportion θ of these intermediately adsorbed oxygen atoms participate in the reaction to form ozone (Eq. 33), while the remaining proportion $(1 - \theta)$ initially reacts further to form diatomic oxygen (Eq. 34). Again, a proportion β (Eq. 35) is involved in the ozone formation reaction (Eq. 30), while the remaining proportion $(1 - \beta)$ desorbs from the surface as O₂, being an electrochemical by-product (Eq. 36). Sequentially, θ and β represent the proportions of the reactants from Eq. 30 to Eq. 37 and can desorb from the electrode surface as O₃ molecule (Eq. 38) in order to act as the intended disinfectant in water.

As the cathodic reaction (Eq. 25) occurs equivalently during EOP, hydrogen is formed in addition to the anodic formation of oxygen or ozone. However, potentially pressurized mixtures of oxygen and hydrogen may pose a massive safety risk as oxyhydrogen gas in piping systems, the use of undivided electrolysis cells for the purpose of ultrapure water disinfection by means of ozone should be suspended. A constructive approach is to use electrolysis cells with a spatial, gas-tight separation of the anolytic and catholytic compartments by introducing a solid electrolyte [90]. For this, a stack of an anode, polymer electrolyte membrane (PEM) and a cathode in a zero-gap arrangement, also known as a membrane electrode assembly (MEA), is particularly efficient (Fig. 1-6).

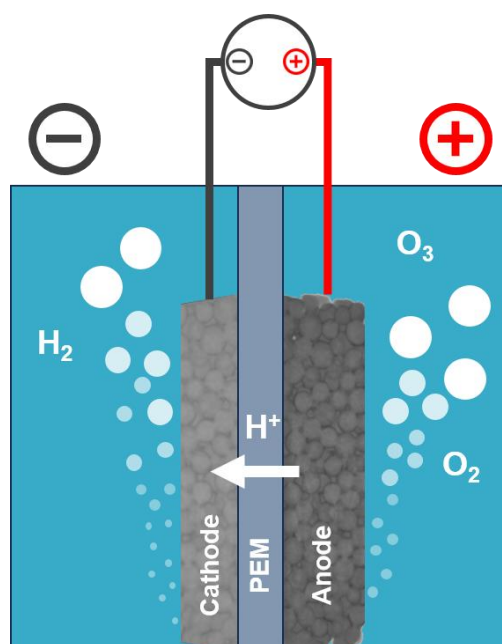


Fig. 1-6. Schematic diagram of a PEM water electrolyzer for ozone production. The polymer electrolyte membrane (PEM) separates the anodic compartment from the cathodic compartment but allows protons to pass as charge carriers. EOP and OER occur on the anode during water electrolysis, while hydrogen is produced on the cathode. Water reaches the catalytic PbO₂ surface through the porous DSA structure and gaseous products are reliably removed.

A PEM can be interpreted as a polymer electrolyte membrane, indicating its structural composition, or as a proton exchange membrane, which emphasizes its function as a cation exchanger. Usually, the components of a PEM are based on materials such as polytetrafluoroethylene (PTFE) or polyether ether ketone (PEEK), which are modified to cation exchangers by a targeted functionalization with sulfonic acid groups (e.g. sulfonated PEEK = SPEEK) [91–93]. Widespread, and to some extent used as a reference PEM in this study, perfluorinated and sulfonic acid derivatized compounds are available under the trade name Nafion™. The products differ in terms of varying material thicknesses and equivalence weights, which is the molar mass per functional sulphonic acid group. Low equivalent weights are therefore associated with a higher density of functional groups and result in a more efficient ion exchanger (Fig 1-7).

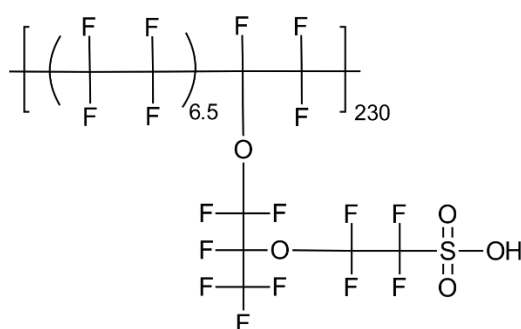


Fig. 1-7. Chemical structure of Nafion™ for equivalent weight of 1100 g/mol, as used in Nafion™ 117 [93–95].

Nafion™ forms a characteristic channel-pore structure that serves as ion channels through which protons as charge carriers can be transported by various mechanisms. These mechanisms strongly depend on the degree of hydration of the ionomer [96,97]. This allows for the construction of spatially separated electrolysis cells [98] that use functionalized anodes while the hydrogen is safely produced in a spatially separated compartment.

Therefore, this design has become established as the favored technology for the *in situ* production of disinfectants and is nowadays available as standard for cold-stored ultrapure water in commercial products (Fig. 1-8).

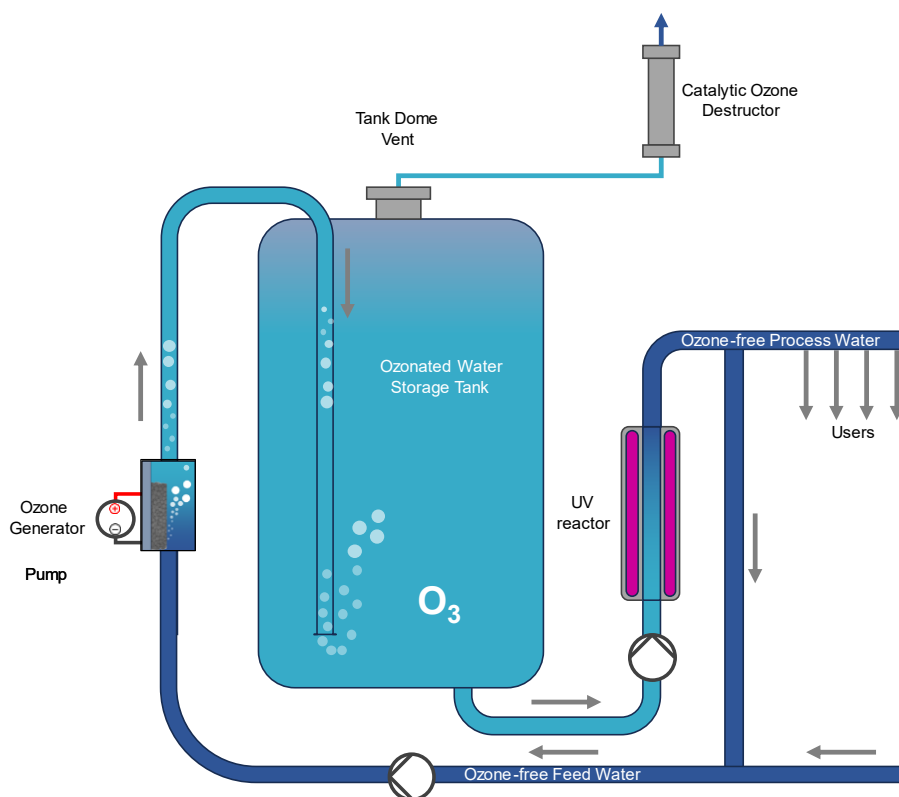


Fig. 1-8. Schematic example of a production plant for ultrapure water production with cold storage of the process water according to the specifications of the International Society for Pharmaceutical Engineering (ISPE) [99].

In the UPW production plant, the feed water for ozone production is obtained from treatment and ‘polishing’ methods such as reverse osmosis, ion exchangers and electro-deionization [16,100,101], before reaching the ozone generator. The freshly ozonized water is subsequently fed into a storage tank and stored with a desirably constant concentration of dissolved ozone. A catalytic ozone destructor [102] is usually mounted on top of the water storage tank to prevent leakage of gaseous ozone arising from the non-sealed system due to rising and falling tank filling levels and thus varying gas volumes above the water surface. When a batch of water is needed for a subsequent process, the stored water is run through a UV reactor and dissolved ozone is removed photolytically (Eq. 39 and 40), eventually participating in the ozone decay circle (Fig. 1-2) [103,104].



Surplus de-ozonized process water, which is not used up by subsequent users in the process, is re-routed to the feed water loop and re-supplied into the ozonation process.

1.5 Ozone detection in the context of process analysis

During cold ultrapure water storage, a permanently low but constant ozone concentration of 20 to 50 $\mu\text{g L}^{-1}$ is aimed for to ensure sterility in the process water shortly before use [10,15]. Therefore, accurate information about the amount of dissolved ozone or other reactive oxygen species in the process water is needed. The ultrapure water loop is ideally located in a closed circuit for safe storage, which provides several options for determining the actual analyte concentrations in the context of process analytical chemistry [105] (Fig. 1-9). In-line measurement allows for the determination of the ozone concentration directly from the main flow of the process. On-line measurements are often applied when e.g. flow velocities influence the analysis method/technology. Is a detection reagent used to determine the ozone concentration, a certain amount of water has to be collected from the tank and analyzed outside the plant to prevent contamination of the process medium. Depending on the scope and duration of the analysis or the stability of the sample, the analysis can then be carried out directly at the plant (at-line) or taken to another analysis site (off-line), i.e. for analyses requiring special equipment. Usually, in-line or on-line analyses are preferred as they allow a real-time integration into the control technology.

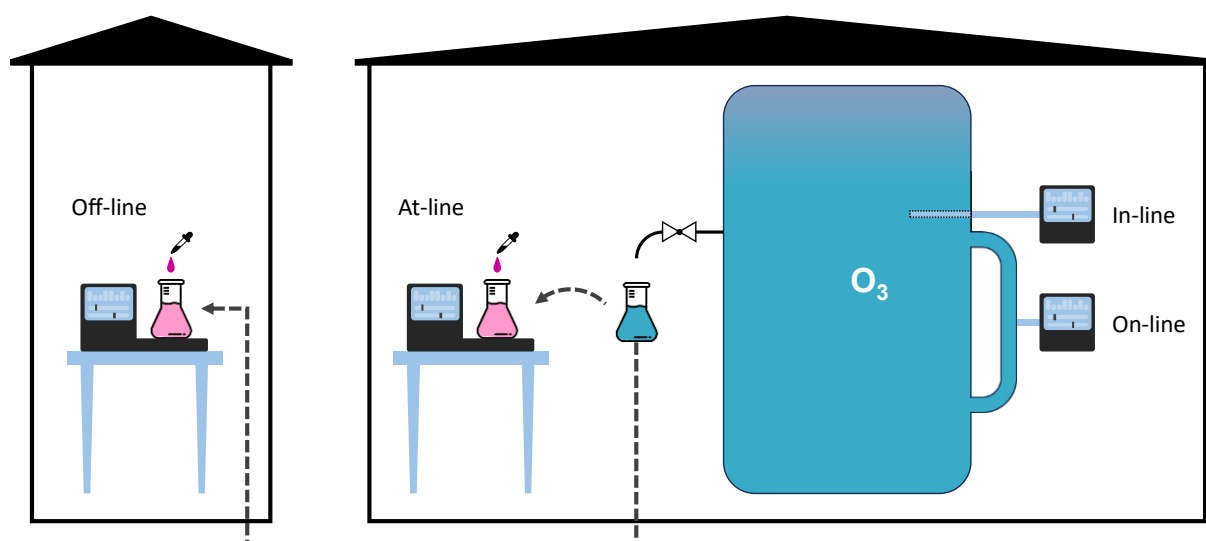
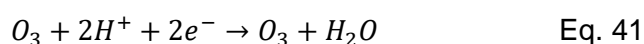


Fig. 1-9: Schematic representation of different forms of process analysis using the example of the determination of ozone for cold ultrapure water storage.

In the field of in- or on-line process analysis for ozone detection, commercial amperometric detectors are available. There, detectors register the electric current during the electrochemical reduction of ozone (Eq. 41) under mass transfer [106–108].



This technique usually works with a 3-electrode setup (Fig. 1-10 (a)), in which the working and counter electrodes are made of gold or platinum as the active surface and are measured against a suitable Ag/AgCl or Hg₂Cl₂ (calomel) electrode as a reference electrode.

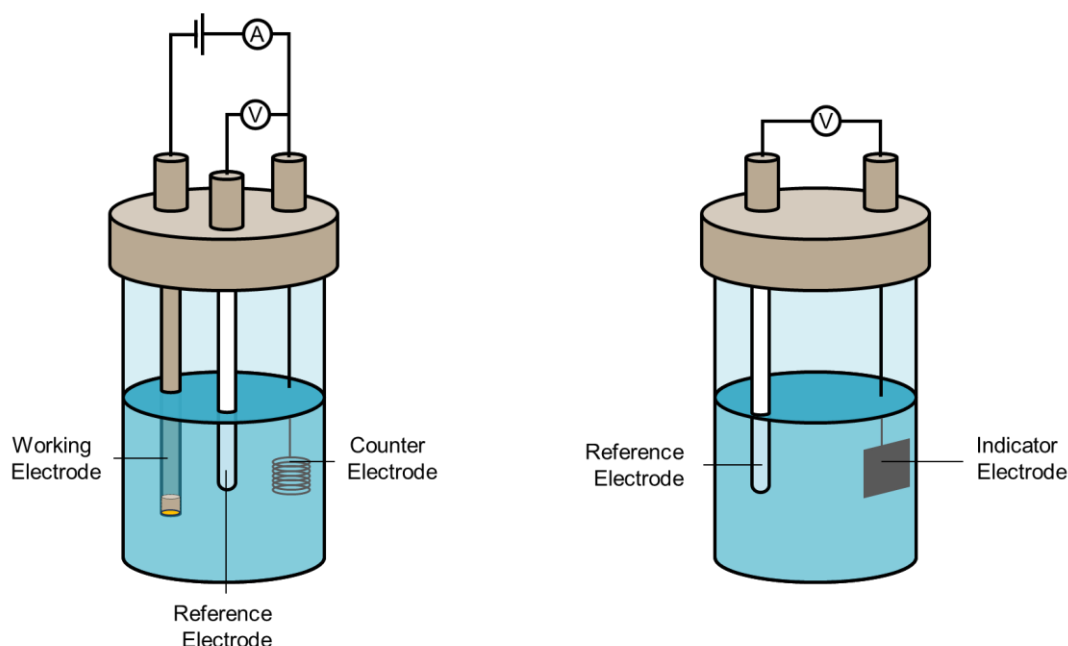


Fig. 1-10. (a) Schematic drawing of an electrochemical three-electrode setup consisting of a working electrode, counter electrode and a reference immersed in an electrolyte. **(b)** Schematic drawing of a simplified setup for potentiometric measurements, consisting of a reference and indicator electrode immersed in the analyte-containing solution.

At a fixed potential between the working and counter electrode, the current is measured and is correlated with the reduction of the ozone concentration in the process water. Masking the gold surface with a thin layer of a polymer electrolyte such as Nafion™ leads to a low detection limit of ozone in the range below 1 µg L⁻¹, which is also relevant for the intended application with expected concentrations of up to 50 µg L⁻¹ [108–110]. A sensitive sensor response for ozone is achieved, while only a low cross-sensitivity with oxygen and other oxidizers such as hypochlorous acid (HClO) or hydrogen peroxide is observed. However, high costs are associated with such systems and are a disadvantage for their widespread use at strategically favorable measuring points in the ultrapure water production cycle. As a result, only a single measuring point is typically provided in complex systems to record and utilize the ozone concentration for the control technology.

Potentiometric sensors are often more affordable alternatives which are based on a different measuring principle (Fig. 1-10 (b)). To determine the content of a dissolved analyte, the cell voltage is measured in equilibrium against a reference electrode whose potential must be sufficiently independent of the sample composition [111,112].

A spatial separation using a solid electrolyte may allow the reference electrode to be separated from the analyte-containing solution and placed in a controlled environment. Most electrode materials have no inherent selectivity towards a particular reactant, which is why ion-selective electrodes feature a masked indicator electrode e.g. with a membrane that is permeable or at least interactable for the ion of interest [113]. With ozone as the only relevant analyte in ultrapure water systems, it is therefore not the reversible interaction of O_3 molecules with the electrode surface that can be expected, but rather a reversible charge transfer by interaction with the electrode. This makes redox sensors in form of ORP (oxidation-reduction potential) electrodes particularly interesting for describing the dissolved ozone concentration present – provided that other reactive oxygen species or impurities (i.e. reductants) can be excluded that unfavorably influence the oxidative state of the water [114].

Occasionally, UV photometric methods of the quantification of dissolved and gaseous ozone within the process water are applied and can be described by the Beer-Lambert law (Eq.42).

$$A = \log\left(\frac{I_0}{I}\right) = \varepsilon \cdot l \cdot c \quad \text{Eq. 42}$$

In this equation, A is the absorbance, ε the molar attenuation coefficient or absorptivity of the attenuating species (e.g. ozone in the aqueous phase), l is the optical path length and c the molar concentration of the attenuating species.

The different absorptivities of ozone ($\varepsilon_{O_3,gaseous} = 3024 \text{ cm}^{-1} \text{ mol}^{-1} \text{ L}$ at 253.7 nm vs. $\varepsilon_{O_3,aqueous} = 2900 \text{ cm}^{-1} \text{ mol}^{-1} \text{ L}$ at 258 nm) allow for a simultaneous, differentiated and comprehensive assessment of the ozone concentration in both gaseous and aqueous state. This analysis can be performed by stripping the ozone out of the water into the gaseous phase [115], separating dissolved and gaseous ozone [61] or the application of high pressure [62] which assumes to quantitatively force gaseous ozone into the aqueous phase. Stripping approaches are not common as in- or on-line analysis methods in UPW production plants due to the potential danger of contamination and changes in pressure. When ozone bubbles are expected due to process control, a mixed signal composed of two different absorption measurements would be obtained and obscures the real ozone content. Systems that no longer measure the water within the main process but use water that is being discarded from the system can be considered integrated at-line analysis methods. These systems usually carry out known photometric detection methods by dosing suitable reagents in a partially or fully automated manner.

In reference analysis, a variety of detection methods have been developed for the determination of dissolved ozone and often incorporate a spectroscopically convenient reaction partner that is colored (Fig. 1-11 (a)) or decolored (Fig. 1-11 (b)) [116–118] over the analytical course.

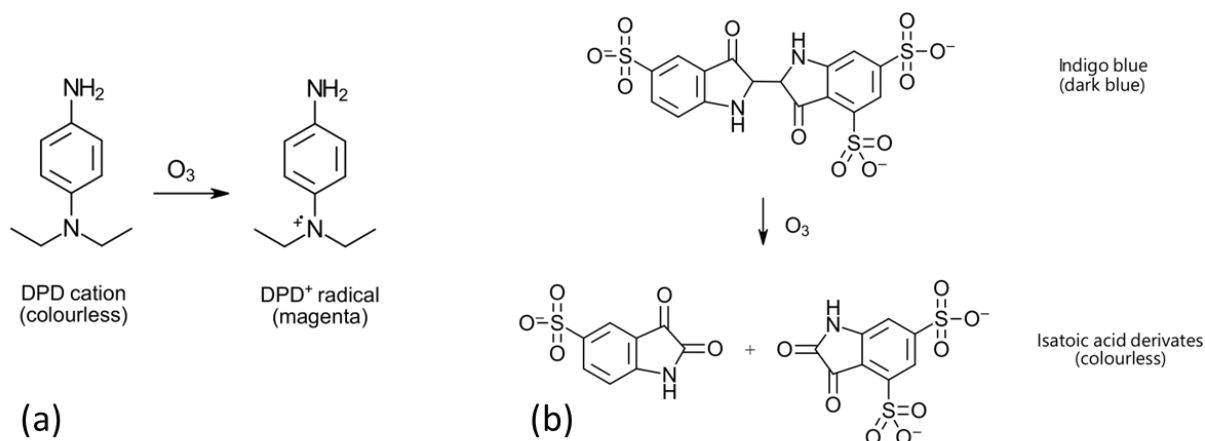


Fig. 1-11. (a) Reaction scheme of N,N-diethyl-p-phenylenediamine (DPD) in the presence of an oxidizing agent such as ozone. Following a one-electron oxidation, a DPD⁺ cation is formed which exhibits a characteristic magenta color. Eventually, this allows for a convenient photometric determination. **(b)** Reaction scheme of Indigo blue with ozone. Caused by the oxidation, a decolorization of the blue dye occurs.

Well-known representatives of these are established staining assays such as the DPD (N,N-diethyl-p-phenylenediamine) assay [118–123]. The methods allow for a sensitive detection of dissolved ozone and therefore have found their way into norms and standards for reference analyses [124]. However, these detection methods are not necessarily free of interference, as other oxidants such as chlorine species and other reactive oxygen species react in the same manner with these reagents and would therefore additionally be detected. Hence, other oxidants should be systematically excluded. Due to their limited time stability of only a few minutes, these detection methods for reactive oxygen species are more suitable in principle for at-line than off-line analysis.

1.6 Objectives

The previous sections led from the question of the treatment of drinking and ultrapure water to the electrochemical production of reactive oxygen species, in particular ozone. Even though the *in situ* production of ozone is widespread in the application of ultrapure water production, a number of questions have arisen from the literature that need to be addressed in more detail.

The focus of this work lies partially in the development of different analysis methods to determine reactive oxygen species (ROS). For this, firstly, the ROS evolving during electrolysis on PbO_2 anodes need to be characterized more thoroughly, as many ROS are involved in the process of electrochemical ozone generation. Consequently, the production rates of hydroxyl radicals, ozone and hydrogen peroxide are acquired as a function of different current densities and even organic content of the process water. Common spectroscopic detection assays for different ROS are known to partially interfere with each other, yet a comprehensive assessment of cross-sensitivities is missing and needs to be resolved for the aforementioned species. Furthermore, the production of hydrogen peroxide as an ozone-decomposing compound in the context of the peroxone-process is evaluated as both oxidants contribute to a sanitization of ultrapure water. An evaluation is necessary as to how an ORP sensors may reliably serve as a monitoring device for the sanitization status of the water.

A further aim of this study is to develop a potentiometric sensor for ozone quantification, in order to move from reliable but laborious at/off-line analyses to a more real-time on/in-line analysis. Low-cost potentiometric sensors for ozone quantification are rarely described in literature. As sensor materials based on NafionTM as a substrate and noble metals as the indicator electrode (Ionic Polymer Metal Composites = IPMC) gained attention in a related context, the preparation of a sensitive yet robust sensor material upon this technique would be desirable. Unfortunately, the correlations between synthesis parameters and subsequent physico-chemical properties show a large vacancy in literature. The conditions that led to the most sensitive or most robust ozone sensing material may then be related to certain physico-chemical properties of the sensor material. An analytical flaw in the sense of metal loading measurements of IPMCs are the either destructive or inaccurate ways of determination that need addressing.

The final goal is the characterization of this PEM electrolyzer as a sanitization device in a non-UPW environment, i.e. tap water. The presence of cations abundant in tap water can be expected to contribute to the electrolysis current and strongly influence the water composition by removing them from their originally analytical compartment. It is therefore necessary to quantify the influence of different water qualities on the transport efficiencies of both protons and tap water cations. Operational conditions need to be identified that may amplify or suppress a potentially harmful crossover of charge carriers except the *in situ* produced protons.

As little is known about both short- or long-term operation of PEM electrolyzers in tap water, the operation of the electrolyzer is observed in a longer time frame to allow for a statement of its stability and perspective application.

1.7 Thesis

Challenges in the determination of reactive oxygen species evolving during membrane water electrolysis for in situ ozone production (Chapter 2)

In chapter 2, common photometric methods are evaluated and sequentially used for a differentiated analysis of reactive oxygen species evolving during the operation of a PEM electrolyzer. In this context, a particular emphasis is put on the consideration of the oxygen reduction potential and residual carbon content upon reactive oxygen species evolution.

Evaluating Platinum-Based Ionic Polymer Metal Composites as Potentiometric Sensors for Dissolved Ozone in Ultrapure Water Systems (Chapter 3, Paper)

Chapter 3 deals with the development of a platinum- and PEM-based sensor material for both a robust and sensitive detection of dissolved ozone in ultrapure water. Using a systematic approach and subsequent statistical evaluation, the synthesis conditions contributing to the desired physicochemical properties are identified. Additionally, a non-destructive computed tomography method is presented and evaluated for its suitability in Pt detection for the determination of noble metal loading.

Operating an ozone-evolving PEM electrolyzer in tap water: A case study of water and ion transport (Chapter 4, Paper)

Chapter 4 showcases the application of the PEM electrolyzer intended for ozone evolution in a tap water environment. The influence of different cation concentration (representing water hardness levels) on ion and water transport through the polymer electrolyte is modeled for different operational parameters. With this input, an optimized electrolyzer design can be presented that can help extend the lifetime of conventional setups.

Discussion and Conclusion (Chapter 5)

The obtained results from the previous chapters are thoroughly discussed with respect to the applicability of the PEM electrolyzer and its intended use in ultrapure and tap water. Furthermore, the results are debated in the light of the original objectives and the progress in literature they provide.

Chapter 2: Challenges in the determination of reactive oxygen species evolving during membrane water electrolysis for *in situ* ozone production

Abstract

The treatment of ultrapure water with electrochemically produced ozone is a common means for disinfection yet leads to the formation of a variety of reactive oxygen species (ROS). The present study draws a comprehensive comparison between three commonly used photometric and fluorometric assays for ROS analysis and quantifies the individual signal responses for dissolved ozone (O_3), hydroxyl radicals ($\cdot OH$) and hydrogen peroxide (H_2O_2), respectively, to account for cross-sensitivities. By calibrating all combinations of assays and analytes in ultrapure water environments, we developed a quantification procedure to reliably determine the actual ROS composition for different operation conditions of a membrane water electrolyzer with PbO_2 anodes down to concentrations of $0.97 \mu g L^{-1}$. While the $\cdot OH$ formation rate can be described linearly over the observed current density range, substantial O_3 evolution is only found for current densities of $0.75 A cm^{-2}$ and above (up to $3.7 \mu mol h^{-1}$ for $J = 1.25 A cm^{-2}$). The formation of H_2O_2 is only observed when an organic carbon source is introduced into the solution. We further elucidate the interference of H_2O_2 with the reading of the oxidation-reduction potential as a common water parameter and elaborate on its validity to describe the actual ROS composition.

2.1 Introduction

Water supply lines are critical infrastructure elements that have to be kept free from pathogens and pollutants in order to provide access to potable or process water in suitable qualities for the intended applications. The necessity for their systematic sanitization becomes most obvious when considering cold-stored ultrapure water, e.g. for pharmaceutical purposes [11,12]. Typically, disinfection is achieved by adding oxidants at defined levels to the water feed to inactivate harmful microorganisms and remove contaminations effectively [125–127]. While potable water is still commonly treated with different chlorine species, the formation of potentially critical disinfection by-products has to be avoided and therefore ozone (O_3) constitutes the preferred powerful oxidant ($E^0(O_3/O_2) = +2.07$ V vs. SHE) for use in ultrapure water environments [10,128].

As the necessary amount of oxidant varies greatly depending on both the feed water quality and the required water conditions, it is desirable to adopt the introduction of ozone into the feed water in a defined manner. Since this unstable compound cannot be conveniently stored in gas cylinders, a frequently suggested approach for disinfection and continuous removal of residual organic compounds is based on the *in situ* formation of reactive oxidants (i.e. hydroxyl radicals ($\cdot OH$) or ozone) by direct oxidation of water. As their evolution occurs at higher thermodynamic potentials than oxygen gas, there is a state of competition between the oxygen evolution reaction (OER) and e.g. the electrochemical ozone production (EOP) [56]. Therefore, the use of special electrocatalysts, such as boron-doped diamond (BDD) or β - PbO_2 with a high overvoltage for oxygen evolution, is indispensable for an efficient anodic oxidation [31,67,68,129]. During this process water is split into both hydrogen gas and a mixture of O_2 and O_3 gasses by electrical energy using a thin, solid polymer electrolyte membrane (PEM) as an ionic conductor between the electrodes [97,130]. This favorable design does not depend on the electrical conductivity of the ultrapure water, which is often a limiting characteristic for electrolysis.

The mechanism of the electrochemical ozone generation strongly depends on the selected catalyst material and involves the formation of $\cdot OH$ as precursor species, which may be either strongly adsorbed for subsequent surface reactions (e.g. on β - PbO_2) or weakly adsorbed and partially released (e.g. on BDD) [73,131]. Depending on the feed quality, not all ozone is immediately consumed during water treatment, with the remainder contributing to a systemic protection of stored ultrapure water due to a depot effect.

The decomposition of ozone is a complex interaction of reactive oxygen species (ROS) with each other. Due to the short half-life of dissolved ozone ($t_{1/2} \approx 80$ min in an ultrapure water setting [132]), it decays rapidly and can generate a large amount of hydroxyl radicals

[37,133,134], which are highly reactive ($E^0(\cdot\text{OH}/\text{H}_2\text{O}) = +2.73 \text{ V vs. SHE}$ [23]) and enable further secondary oxidation reactions, especially with (organic) contaminants [31,135–137]. Although many involved intermediate species have a chemically unstable character, by-products such as H_2O_2 can be quantitatively determined, especially when they emerge during the ozonation of dissolved organic matter (DOM) [138–140]. However, as H_2O_2 is known to rapidly decompose ozone *via* the peroxone reaction [45], its accumulation in ultrapure water systems may impede the overall sanitization process due to its impact on the systemic protection. Because of this multi-step reaction cascade including many short-lived intermediates, there may be a variety of ROS present in solution, which contribute to the overall disinfection effect. An overview of evolving ROS in a PEM electrolyzer setup is given in Fig. 2-1, depicting a selection of the most prominent reactions within the ozone degradation cascade.

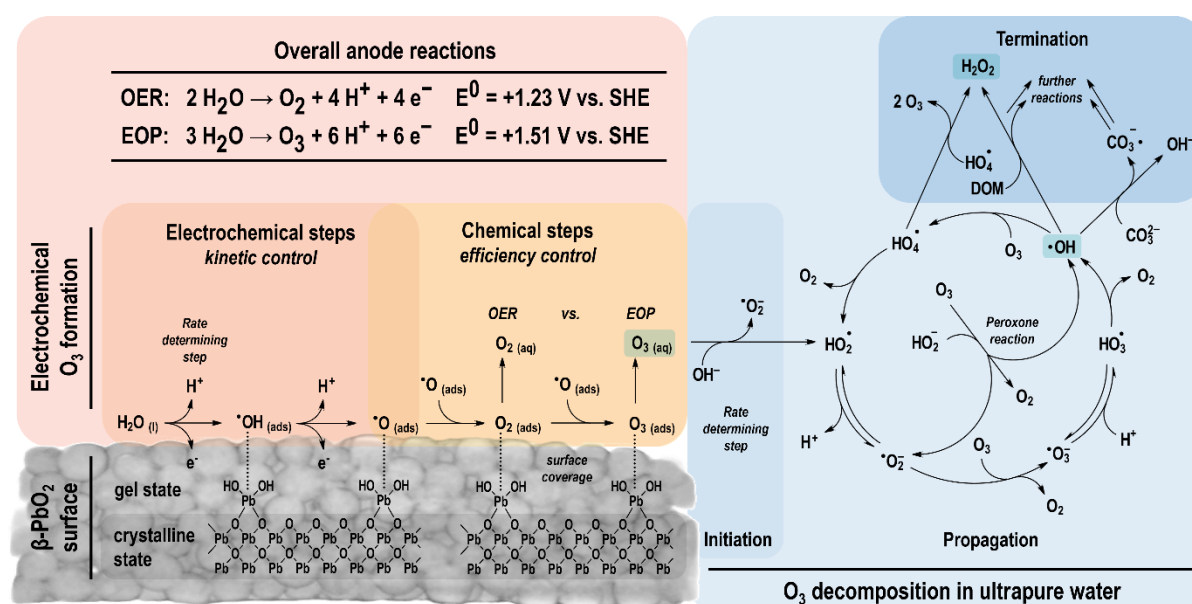


Fig. 2-1. Scheme of the evolution of different ROS during PEM electrolysis on a $\beta\text{-PbO}_2$ anode surface and subsequent decomposition of O_3 in ultrapure water. The ozone evolution process (orange and yellow area) emphasizes the competition between OER and EOP, depending on the surface coverage of oxygen intermediates. The following, non-exhaustive decomposition cycle (blue area) integrates a broad variety of short-lived radicals, which can also lead to H_2O_2 as a stable oxidizing agent. Own drawing, adapted and combined according to [36,43–45,56,64,89,138].

As a common and convenient technique to characterize the oxidative properties of water samples, the oxidation-reduction potential (ORP) allows for an estimation of the present disinfectant concentration [141,142]. However, in systems which inherently allow for the presence of more than one ROS, the ORP signal is a mere sum parameter and may camouflage inconsistent water quality levels due to varying ROS compositions [143]. Hence,

for applications demanding detailed information about the concentration of individual ROS, measuring the ORP signal cannot be the method of choice.

In addition to the presence of electrochemically produced ozone, other ROS can emerge in aqueous solution and therefore pose a particular challenge for independent quantification [144,145]. Concerning dissolved ozone as the target analyte, sensor systems that enable measurements in a range of 0.5 to 200 $\mu\text{g L}^{-1}$ [108,132,146] have been developed and proven reliable in automated process analytics. Simple colorimetric assays (based on dyes such as DPD or Indigo) are still commonly applied as convenient off-line analyses in laboratory and field trials and can detect O_3 as low as 0.4 to 40 $\mu\text{g L}^{-1}$ [117,118,120], but are known to also react with other oxidizing species [124,147,148]. As for $\cdot\text{OH}$, common quantification approaches involve rapid reactions of radical scavengers (e.g. terephthalic acid), followed by a subsequent analysis of the reaction products *via* chromatography [149,150], UV spectrometry [151,152], fluorescence [153–155] or even electron spin resonance [156]. For a selective determination of H_2O_2 , a variety of colorimetric and electrochemical methods [157–159] can be used, including the most prominent titanyl sulfate assay [160].

While these advanced analytical methods ensure a highly selective and sensitive determination of ROS, they can only be applied in well-equipped laboratory settings. In contrast, it is common knowledge that quick routine analyses by colorimetric assays suffer from considerable cross-sensitivities when multiple ROS occur simultaneously, although these distortions have been insufficiently characterized.

In this study we provide insight into the three most common colorimetric assays used for the quantification of the three most prominent reactive oxygen species evolving during the ozonation of water *via* electrolysis, namely ozone, hydroxyl radicals and hydrogen peroxide *via* DPD, TiOSO_4 and terephthalic acid. With this approach, a stepwise procedure is presented to quantify the actual ROS composition with respect to cross-sensitivities between the evaluated assays. Following our findings, we provide a holistic view on the resulting oxidant composition for different operational conditions of a PEM electrolyzer setup with PbO_2 anodes intended for ozone evolution. Furthermore, we elaborate on linking the chemical information about the ROS composition from colorimetric assays with the analytical water parameters ORP and TOC (total organic carbon).

2.2 Materials and methods

2.2.1 Experimental setup

To investigate the evolution of ROS during the operation of a commercial PEM water electrolyzer, the setups depicted in Fig. 2-2 (similar to previously published studies [161,162]) were used for all experiments. Within a water reservoir, an Ozone-Micro-Cell (OMZ CH1) was installed as the ozone evolving unit, consisting of one PbO₂-coated porous titanium anode and one porous stainless-steel cathode (all Innovatec Gerätetechnik GmbH, Rheinbach, Germany), and separated by a Nafion™ 117 membrane (Chemours®, Wilmington, Delaware, USA) as PEM material in a membrane-electrode assembly (MEA) setup. For experiments with “indirect” ozonation, the evolving gases were exhausted through a stainless-steel pipe into a separate ultrapure water reservoir to evaluate ozone evolution selectively without the presence of ROS generated by side-reactions. “Direct” ozonation refers to ultrapure water in the reaction vessel being treated electrochemically without mediation, which was selected for the investigation of ·OH and H₂O₂ evolution.

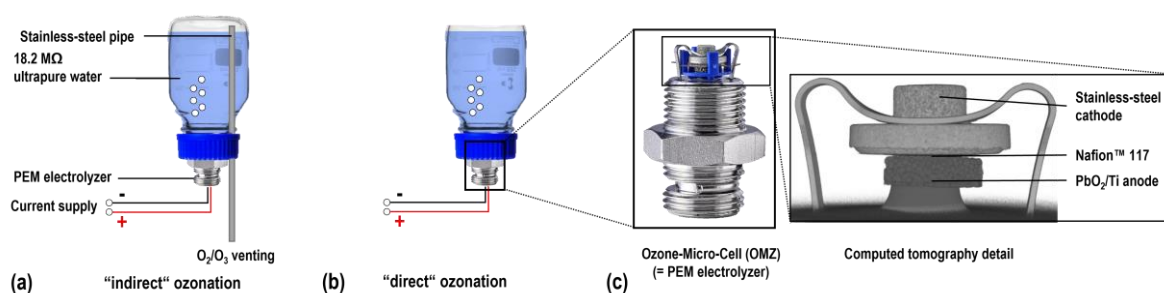


Fig. 2-2. Scheme of the experimental setup for (a) “indirect” ozonation and (b) “direct” ozonation of water reservoirs. While the direct treatment allows for an immediate probing of the ozonated water, the indirect treatment requires the ozone gas to be transferred and introduced into a separate reaction vessel filled with ultrapure water via a stainless-steel pipe. (c) A detailed insight into the MEA arrangement and its porous electrodes is given using computed tomography imaging.

Evolving oxidizing agents were investigated over 90 minutes of operation and current densities in a range from 0.25 to 1.25 A cm⁻², referring to a geometric surface of 0.2 cm² for the anode. In order to simulate a typical stand-by operation, an additional level of 0.01 A cm⁻² (for anodic protection of the catalytically active PbO₂ layer) was evaluated. All reported data for every experimental condition are mean values originating from three independent replicate runs.

For certain experiments, isopropyl alcohol (denoted i-PrOH; Carl Roth, Karlsruhe, Germany) was added to the ultrapure water to achieve defined levels of dissolved organic matter, represented by the TOC value as a common analytical water parameter. In order to mitigate

effects caused by light or CO₂ ingestion, these experiments were conducted under Argon 4.8 gas purging (Westfalen AG, Münster, Germany) and UV protection.

2.2.2 Analytical procedures

For each of the three analytes, an individual assay is used to quantify concentrations and production rates, and additionally tested for cross-sensitivities. For this purpose, the assays were equally treated with defined concentrations of the other ROS under investigation, aiming to describe the signal response with suitable regression functions. The chosen analytical procedures yield observable concentrations for dissolved O₃ and H₂O₂, however, only a cumulative value for scavenged ·OH can be obtained due to its extremely short-lived character ($\tau \approx 10 \mu\text{s}$) [163].

Determination of ozone was carried out using the DPD assay in accordance with DIN 38408-3:2011-04, using DPD ((N,N)-diethyl-*p*-phenylenediamine; Fisher Scientific, Waltham, MA, USA), KIO₃ (Merck, Burlington, MA, USA) as well as KI and Na₂SO₃ (both Carl Roth, Karlsruhe, Germany) [124].

Hydroxyl radical formation was evaluated with a fluorometric method according to [154] using terephthalic acid (TA) (Alfa Aesar, Haverhill, MA, USA) and 2-hydroxyterephthalic acid (HTA) (Apollo Scientific, Bredbury, United Kingdom). HTA calibration solutions in the range from 0.11 to 3.64 mg L⁻¹ as well as analyte solutions were excited and the resulting fluorescence signal was used for characterization. Fluorescence spectra were processed with OriginPro 2022 (OriginLab, Northampton, MA, USA) by integration of the acquired fluorescence signal between $\lambda = 340 \text{ nm}$ and $\lambda = 580 \text{ nm}$ and background correction. For cross-sensitivity evaluation of the DPD assay, the amount of ·OH was adjusted using hydrogen peroxide and FeSO₄ · 7 H₂O (both Carl Roth, Karlsruhe, Germany) via Fenton reaction.

The quantification of hydrogen peroxide was carried out based on DIN 38409-15:1987-06 using a solution of titanil sulfate in sulfuric acid (Merck, Burlington, MA, USA) in a 5 cm cuvette [164]. Calibration solutions were prepared ranging from 0.07 to 1.77 mg L⁻¹.

All chemicals were at least of analytical grade purity. 18.2 MΩ ultrapure water was provided for all experiments by a ELGA Purelab Flex (VWS, High Wycombe, UK) water purification system. Photometric determinations were performed on a DR3900 UV/VIS spectral photometer (Hach Lange, Loveland, CO, USA), with absorption measurements at $\lambda = 510 \text{ nm}$ for the DPD assay and at $\lambda = 407 \text{ nm}$ for the TiOSO₄ assay. For fluorometric determinations, a custom setup was developed using SETi (Columbia, SC, United States) CUD1GF1A light

emitting diodes ($\lambda_{\text{max}} = 315 \text{ nm}$) and an Ocean Insight (Orlando, FL, United States) Ocean HDX spectrometer. A comprehensive overview of all applied assays for ROS determination in this study is given in Fig. 2-3.

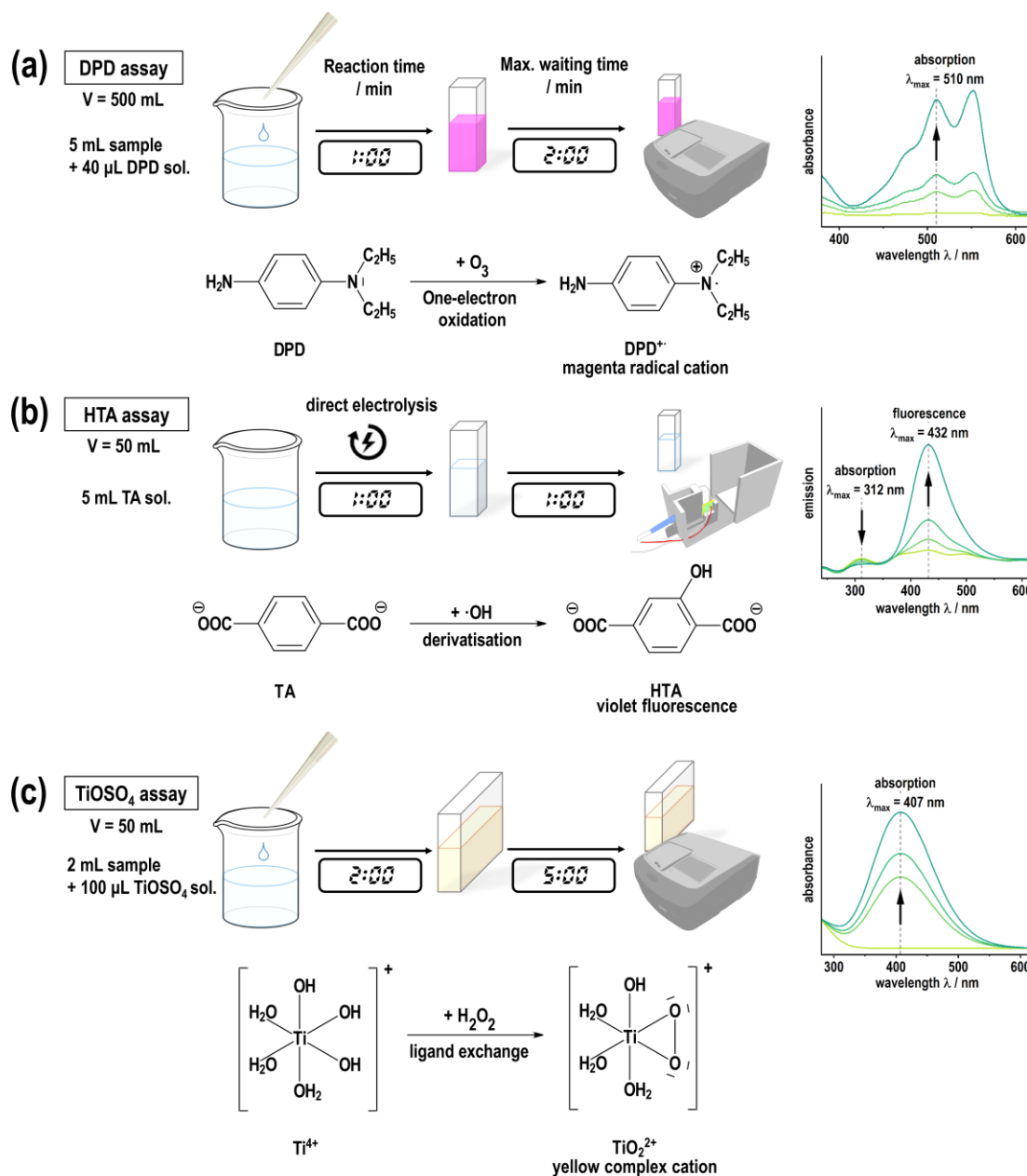


Fig. 2-3. Overview of the assays for ROS determination used in this study: **(a)** O_3 determination via DPD assay. Ozone reacts with DPD in a one-electron transfer reaction, forming a radical DPD cation acting as a detectable dye. After 1 minute the absorption of the magenta radical cation can be measured at $\lambda_{\text{max}} = 510 \text{ nm}$. For different concentration ranges, 1 cm and 5 cm cuvettes were used. **(b)** $\cdot\text{OH}$ determination via HTA assay. Hydroxyl radicals are scavenged by TA forming HTA, which can be measured by excitation at $\lambda_{\text{max}} = 312 \text{ nm}$ and subsequent detection of fluorescence at $\lambda_{\text{max}} \approx 430 \text{ nm}$. **(c)** H_2O_2 determination via TiOSO_4 assay. Ti^{4+} ions form colorless aquo complexes which turn into yellow complex cations by ligand exchange after the addition of hydrogen peroxide. Within 5 minutes, the absorption is measured at $\lambda_{\text{max}} = 407 \text{ nm}$.

2.2.3 ORP measurements

For ORP (oxidation-reduction potential) signal measurements, stock solutions of O_3 (approx. 2 mg L^{-1}) and H_2O_2 (approx. 100 mg L^{-1}) were freshly prepared. Solutions in a range of $\beta_{aq}(O_3) = 0.2 \text{ mg L}^{-1}$ to 1.0 mg L^{-1} and $\beta_{aq}(H_2O_2) = 0.1 \text{ mg L}^{-1}$ to 17 mg L^{-1} were measured with a SenTix® Pt ORP sensor equipped with a Ag/AgCl reference electrode (Xylem Analytics, Washington, D.C., US) and an InLab Micro pH electrode (Mettler Toledo, Columbus, OH, US). Concentrations were verified using the aforementioned colorimetric assays intended for the respective analytes.

In order to evaluate the consumptive effect of hydrogen peroxide on dissolved ozone, a reaction vessel with 5 L of ozonated water at different concentrations ($\beta_{aq}(O_3) = 50$ and $100 \text{ } \mu\text{g L}^{-1}$) was prepared *via* “indirect” ozonation and subsequently doped with different levels of hydrogen peroxide in a molar ratio range of $n_0(H_2O_2)/n_0(O_3) = 0.14$ to 13.5 . ORP values were evaluated with a 1 Hz data acquisition rate over a time of 10 minutes before and after H_2O_2 addition to determine the occurring signal drop.

2.3 Results and Discussion

2.3.1. Evaluation of the analytical performance of colorimetric ROS determination methods and their cross-sensitivities

In order to assess the reliability of the obtained spectroscopic data in a first step, all selected methods were examined with respect to the analytical performance of the conducted calibrations. Therefore, limits of detection (LOD) and quantification (LOQ) as well as the coefficient of variation of the procedure (V_{x0}) were evaluated for all analytes of interest using the calibration approach according to DIN ISO 11843-2:2006-06 and DIN 32645:2008-11 (see Table 2-1). All values are expressed as both a mass and molar concentration to give a tangible value for practitioners and also allow for a direct comparison in relative response per reactive oxygen species.

Table 2-1. Analytical figures of merit for regression functions of all spectroscopic assays used for ROS quantification. For each analytical method, the limits of detection (LOD) and quantification (LOQ) are given for the calibration ranges under investigation and show satisfactory values. Additionally, the method precision is given as the coefficient of variation of the procedure (V_{x0}). For the determination of dissolved O_3 via the DPD assay, V_{x0} values are given for the calibration carried out with the 1 cm cuvette and the 5 cm cuvette, respectively.

Analyte		O_3	$\cdot OH$	H_2O_2
Assay		DPD	HTA	TiOSO ₄
LOD	/ $\mu g L^{-1}$	0.97	3.12	25.5
	/ $\mu mol L^{-1}$	0.02	0.18	0.75
LOQ	/ $\mu g L^{-1}$	3.48	11.3	90.0
	/ $\mu mol L^{-1}$	0.07	0.66	2.65
V_{x0} (1 cm / 5 cm)		2.1 / 1.7	2.0 / -	- / 2.3

All calibrations were fitted to linear functions with coefficients of determination $R^2 \geq 0.9995$ and precision coefficients of less than 2.3%, yielding LOD values as low as $0.97 \mu g L^{-1}$ for ozone. Given that all species under investigation can be quantified to trace concentrations of less than $2.72 \mu mol L^{-1}$, monitoring of all oxygen species during PEM electrolysis is confidently possible. This especially holds true for applications in technical facilities where ozone concentrations between 0.35 and $1.15 \mu mol L^{-1}$ are favorably applied [10]. Due the nature of the HTA assay, the obtained analytical parameters only refer to accumulated amounts of scavenged $\cdot OH$ instead of actual $\cdot OH$ concentrations.

As stated before, many colorimetric assays chosen for the determination of ROS are not necessarily selective to a single species. In order to evaluate cross-sensitivities, the assay

response matrix for all investigated ROS is given in Fig. 2-4, with the relevant calibration features listed in Table 2-2.

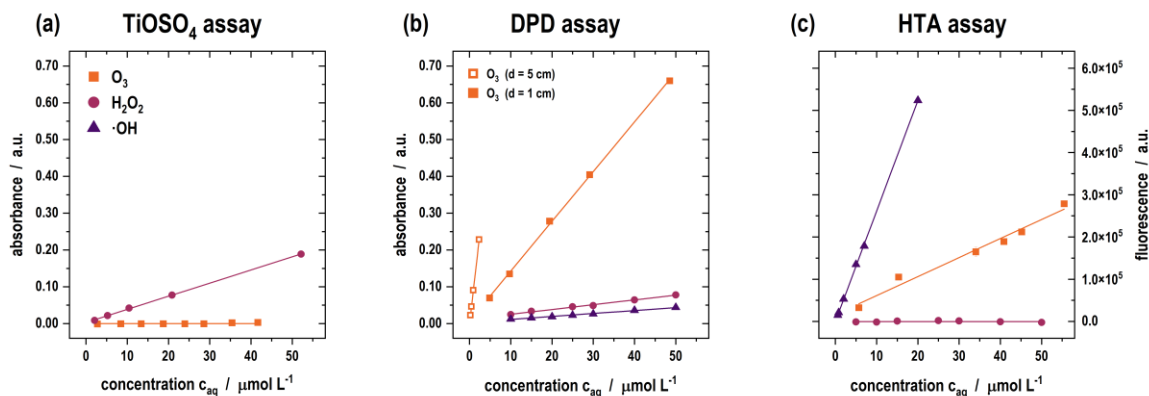


Fig. 2-4. Overview of the responses for the **(a)** TiOSO₄ assay, **(b)** DPD assay and **(c)** HTA assay to identify cross-sensitivities. The absorbance for both the TiOSO₄ and DPD assay is given on the left axis while the fluorescence signal of the HTA assay is referred to on the right axis. Error bars are included, but mostly invisible as they are smaller than the symbol size. For O₃ determination *via* DPD, two separated calibration curves are obtained as two different cuvette sizes are used depending on the concentration range. For calibration ·OH is generated from hydrogen peroxide *via* the Fenton reaction, therefore evaluating the signal of the TiOSO₄ assay would be unselective and misleading.

Not only can valid calibrations be obtained for the assays which are intended for the respective species, it is also possible to adequately describe all observable cross-sensitivities in the observed concentration range by simple regression models: Either the regression yields a linear function when there is a significant reaction or the measured, constant signal is independent of the species concentration, leading to a horizontal line as the assay does not respond to the respective ROS.

Table 2-2. Regression parameters for the linear models describing the assay responses for the respective ROS. Regression functions and R² values are given for each analyte and assay combination, except for calibrations yielding no concentration dependence. I stands for the signal absorbance or fluorescence (both in arbitrary units, denoted a.u.) and c_{aq} refers to the molar ROS concentration.

Analyte	Assay	Regression function	Linearity
O ₃	DPD (1 cm cuvette)	$I = 13.5 \cdot c_{aq} + 0.008$	R ² = 0.9995
	DPD (5 cm cuvette)	$I = 97.1 \cdot c_{aq} + 0.001$	R ² = 0.9999
	HTA	$I = 4.51 \cdot 10^6 \cdot c_{aq} + 0.02 \cdot 10^6$	R ² = 0.9773
	TiOSO ₄	$I = 0.000$	n.a.
·OH	DPD	$I = 1.30 \cdot c_{aq} + 0.012$	R ² = 0.9942
	HTA	$I = 26.2 \cdot 10^6 \cdot c_{aq}$	R ² = 0.9998
	TiOSO ₄	n.a.	n.a.
H ₂ O ₂	DPD	$I = 0.803 \cdot c_{aq} + 0.003$	R ² = 0.9946
	HTA	$I = 0.000$	n.a.
	TiOSO ₄	$I = 3.569 \cdot c_{aq} + 0.003$	R ² = 0.9997

If ROS are to be determined without the presence of interfering species, the intended assays exhibit their suitability. As all calibrations refer to molar concentrations, it is possible to compare the sensitivity for each ROS and method by comparing the slopes of the regression functions. For instance, the quantification of H₂O₂ is most sensibly carried out using the TiOSO₄ assay, which is more than four times more sensitive to H₂O₂ than the alternative DPD assay (3.569 vs. 0.803 L mmol⁻¹).

For ·OH formation the application of the HTA assay is indicated as only the DPD assay leads to measurable results despite being quite insensitive. This observation is similar to a related work, where DPD was used as a radical detection assay involving a Fenton reaction by adding H₂O₂ into a Fe(II)-containing DPD solution, leading to a more pronounced sensitivity [148]. For a selective evaluation of ·OH *via* the TiOSO₄ assay, it would be necessary to reproducibly provide defined amounts of ·OH without using H₂O₂ as a source. Furthermore, the resulting red complex contains a ligand with a peroxide group, which is highly unlikely to form by ·OH self-recombination. Other radical scavenging assays such as ABTS [165] or chromotropic acid [166] were evaluated in pretrials but have proven to not be applicable for species-selective determinations in ozonated water when more than one ROS is present. In case of O₃ determination, both the DPD and HTA assay can be used with sufficient sensitivity, although the reaction from TA to fluorescing HTA is known to be caused by ozone decay and subsequent radical liberation and not by direct ozonation [167,168].

As multiple ROS may be able to coexist within an ultrapure water distribution system due to spatial and temporal separations, the contributions of different species may lead to similar signal responses if only one detection method is applied. Choosing an appropriate and representative sampling point is therefore both tricky and crucial, as varying ROS compositions will not yield unambiguous determinations. This is especially true for highly reactive species that can interact with contaminants or even other ROS.

When it comes to the quantification of more than one occurring ROS, a sensitive determination of O_3 can be achieved by applying the standardized, well-known Indigo assay [118,124], which showed no considerable cross-sensitivity for hydrogen peroxide in pretrials of this study. However, this assay proved to be only applicable in a calibration range from 0.1 up to 0.3 mg L⁻¹ O_3 for the available spectrophotometer equipped with a 5 cm cuvette. Therefore, this assay was not used for subsequent ozone quantifications in this study, which required lower LOD and LOQ values as well as a higher method precision to confidently monitor ozone evolution. Nevertheless, for similar applications dealing with an ozone concentration that is consistent with the calibration range provided by the Indigo assay, this approach could be beneficially applied. If the quantification of H_2O_2 is desired in the presence of other ROS, the $TiOSO_4$ assay is the preferred method, as no interference with O_3 was observed.

Due to the partial selectivity of the presented assays, a breakdown into distinct ROS concentrations is obscured and requires a correction function by using matrix calculation on a linear system of equations [169]. This is used to separate the individual contributions and calculate amended concentrations which reflect the actual ROS composition at a given sampling point more accurately. Consequently, a stepwise ROS quantification needs to be carried out to obtain a comprehensive analysis.

As the determination of H_2O_2 *via* the TiOSO_4 assay is the only method that has proven to be unimpeded by the other ROS under investigation, it inherently provides the real H_2O_2 concentration in a first step (Eq. 2-1). Solving the linear system of equations leads to Eq. 2-2 and Eq. 2-3 which allow for an amended ozone quantification in the presence of hydrogen peroxide. Due to the short lifespan of the hydroxyl radical, only a virtual $\cdot\text{OH}$ concentration (representing the cumulated amount of formed radicals in the given reaction vessel) can be determined with this approach by using the quantified interferences for the other species. For the DPD assay only the calibration range for a 1 cm cuvette was considered.

$$\frac{c_{\text{amended}}(\text{H}_2\text{O}_2)}{\frac{\text{mmol}}{\text{L}}} = 0.280 \cdot I_{\text{TiOSO}_4} - 8.41 \cdot 10^{-4} \quad (\text{Eq. 2-1})$$

$$\frac{c_{\text{amended}}(\text{O}_3)}{\frac{\text{mmol}}{\text{L}}} = -0.0169 \cdot I_{\text{TiOSO}_4} - 3.74 \cdot 10^{-9} \cdot I_{\text{HTA}} + 0.0753 \cdot I_{\text{DPD}} - 0.002 \quad (\text{Eq. 2-2})$$

$$\frac{c_{\text{amended}}(\cdot\text{OH})}{\frac{\text{mmol}}{\text{L}}} = 0.0029 \cdot I_{\text{TiOSO}_4} + 3.88 \cdot 10^{-8} \cdot I_{\text{HTA}} - 0.013 \cdot I_{\text{DPD}} - 4.87 \cdot 10^{-4} \quad (\text{Eq. 2-3})$$

Since the DPD assay shows a reaction with all ROS under investigation, it can be interpreted as an unspecific sum parameter for all occurring oxidizing agents. While this assay may be sufficient to depict ozone concentrations at the time of sampling, the determination of exact formation rates for different ROS requires conducting an HTA assay in parallel. Furthermore, if the presence of H_2O_2 cannot be strictly ruled out, an evaluation *via* the TiOSO_4 assay is also necessary.

In practice, a parallel determination of all three assays is proposed to achieve the most accurate representation of the ROS composition for any given state of operation. For subsequent ROS quantification in the following sections, these corrections were thusly applied.

2.3.2 ROS evolution during PEM electrolysis

Operating the PEM electrolyzer in ultrapure water leads to gaseous ozone evolution on the anodic surface with bubbles eventually rising to the water surface. In this process, ozone partially dissolves into the ultrapure water and can be detected using the aforementioned methods. Fig. 2-5(a) shows that the amount of dissolved ozone increases with the elapsed experimental time and can be described by linear regression functions for all applied current densities.

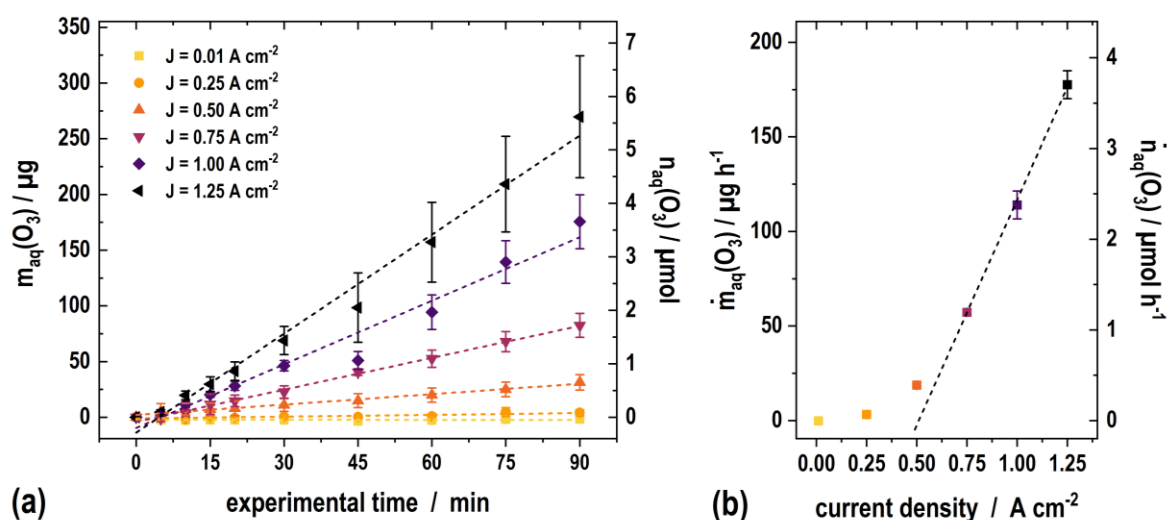


Fig. 2-5. (a) Amount of dissolved ozone $n_{aq}(O_3)$ and $m_{aq}(O_3)$ as a function of the elapsed experimental time for different current densities applied to the electrolytic ozone generator. During operation, the amount of dissolved ozone increases for all current densities and its progression is satisfactorily described with linear regression functions. (b) Ozone formation rates $\dot{m}_{aq}(O_3)$ and $\dot{n}_{aq}(O_3)$ as a function of the applied current density. The formation rate increases significantly more for current densities greater than $0.50 A cm^{-2}$ as indicated by the dashed black line.

After an experimental time of 90 minutes, dissolved ozone concentrations of $0 \mu mol L^{-1}$ and $5.62 \mu mol L^{-1}$ were measured for $J = 0.01 A cm^{-2}$ and $1.25 A cm^{-2}$, respectively. Even when applying a current density of $0.25 A cm^{-2}$ only $0.08 \mu mol L^{-1}$ were found for the same time frame, which is in a comparable order of magnitude as with the applied protection current alone. This barely traceable increase in ozone concentration over time is also demonstrated by low R^2 values. However, for elevated current densities, an accelerated increase in dissolved ozone concentration is observed (see Fig. 2-5(b)). For $J \geq 0.75 A cm^{-2}$, the ozone formation rate follows a linear trend as indicated by the black dashed line. Presumably, this can be attributed to lower anodic potentials at low current densities, which may be insufficient for a significant ozone evolution as OER is thermodynamically preferred over EOP.

The obtained formation rates are a direct result of the experimental setup and only refer to the aqueous phase. A substantial amount of ozone is lost by rising and degassing bubbles, although O_3 exhibits a high solubility in water in direct comparison to O_2 as the main product (480 mg L^{-1} vs. 38 mg L^{-1} at 25°C) [170]. Therefore, a reasonable estimation of a current efficiency is impeded for the given setup. Accounting for a quantitative measurement of both gaseous and aqueous ozone, current efficiencies of 15-20% were previously reported for ultrapure water electrolysis with PbO_2 anodes in a comparable setup [61,62].

Hydroxyl radicals play an important role in both the electrochemical generation and subsequent decay of ozone. Scavenging allows for a time-resolved monitoring of radical evolution depending on the respective electrolyzer setting as displayed in Fig. 2-6(a). As TA is known to be resistant to oxidation by O_3 as well as direct electron transfer reactions [168,171], it is a suitable probe for $\cdot OH$ in this environment and the measured concentration of HTA can therefore be interpreted as an equivalent to the cumulated amount of $\cdot OH$.

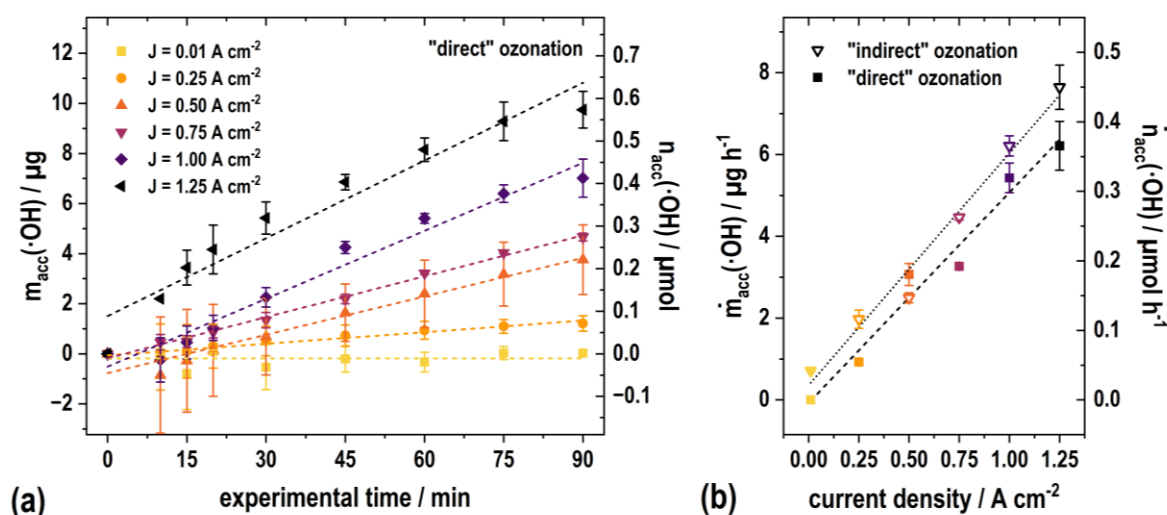


Fig. 2-6. (a) Amount of accumulated $\cdot OH$ radicals $n_{acc}(\cdot OH)$ and $m_{acc}(\cdot OH)$ as a function of the elapsed experimental time for different current densities applied to the PEM electrolyzer. The number of detected radicals increases notably for all current densities $J > 0.01 \text{ A cm}^{-2}$ and its progression is satisfactorily described by linear regression functions. **(b)** The formation rates $\dot{m}_{acc}(\cdot OH)$ and $\dot{n}_{acc}(\cdot OH)$ for detected radicals as a function of the applied current density can be adequately described by linear regression functions (black dotted and dashed lines) for both "indirect" ozonation (∇) and "direct" ozonation (\blacksquare).

While for "direct" ozonation no significant radical accumulation (and therefore formation) is observed in stand-by operation, an increase in current density yields notable amounts of scavenged $\cdot OH$. For all standard operational modes ($J \geq 0.25 \text{ A cm}^{-2}$), the progressively increasing amount of scavenged $\cdot OH$ in solution can be described by linear functions (all

$R^2 = 0.93$ and higher) that allow for a derivation of $\cdot\text{OH}$ formation rates during electrolysis. Plotting the so-obtained values as a function of the applied current density (Fig. 2-6(b)) yields a linear correlation with increasing current densities for both “indirect” and “direct” ozonation ($R^2 = 0.975$ and 0.972 , respectively). As the formation rates for both operational conditions are in similar ranges for each current density level, the occurrence of $\cdot\text{OH}$ can be fully explained by the decomposition of dissolved ozone, indicating no electrochemical generation at PbO_2 anodes. This is in accordance with the mechanistical understanding of the electrochemical surface reactions in ultrapure water [73,172]. Minor differences in the measured formation rates of both operational modes may be attributed to temperature effects (e.g. by heat dissipation from the electrolyzer), leading to a shorter half-life of ozone.

These observations contrast with the generation of ozone which required higher current densities. While formation rates $\dot{n}(\text{O}_3)$ from 0.07 up to $3.70 \mu\text{mol h}^{-1}$ were determined for ozone evolution in the observed current density range, only 0.05 to $0.37 \mu\text{mol h}^{-1}$ were observed for $\cdot\text{OH}$ under the same operation conditions, exhibiting a difference of up to an entire order of magnitude. Considering the ratio $\dot{n}(\cdot\text{OH})/\dot{n}(\text{O}_3)$, values between 0.10 and 0.82 are obtained for all standard operational modes and decrease with increasing current densities.

Controlling the operating conditions of a PEM electrolyzer can help mitigate or predict the evolution of unwanted H_2O_2 because of its impact on ozone depletion. Depending on the structural properties of dissolved carbon sources, various pathways for a reaction with ozone are possible that lead to the emergence of H_2O_2 as a stable side-product (especially *via* the Criegee mechanism for unsaturated compounds) [173]. When considering discontinuously operated ultrapure water distribution systems, a common means of disinfection is isopropyl alcohol (i-PrOH), which often cannot be completely rinsed out and is not removed by commonly applied electro de-ionization either [16]. Therefore it remains in trace amounts as a typical carbon source. As not all structural properties can be adequately represented by a single molecule, the selected i-PrOH only serves as one exemplary model substance and does not allow for a generalized extrapolation for other contaminants contributing to the TOC value. However, due to its high radical scavenging capacity ($k = 2.3 \cdot 10^9 \text{ L mol}^{-1} \text{ s}^{-1}$ [174]) i-PrOH showcases a worst-case estimation for H_2O_2 formation rates in ultrapure water storage and distribution systems.

Specifically for i-PrOH, Reisz *et al.* have reported a mechanistic scheme for both O_3 and $\cdot OH$ mediated pathways that indicate a H_2O_2 yield of about 1.5% considering a non-electrochemical ozonation [138]. The formation rates of H_2O_2 in the presence of i-PrOH are shown in Fig. 2-7 as a function of time, current density and TOC level.

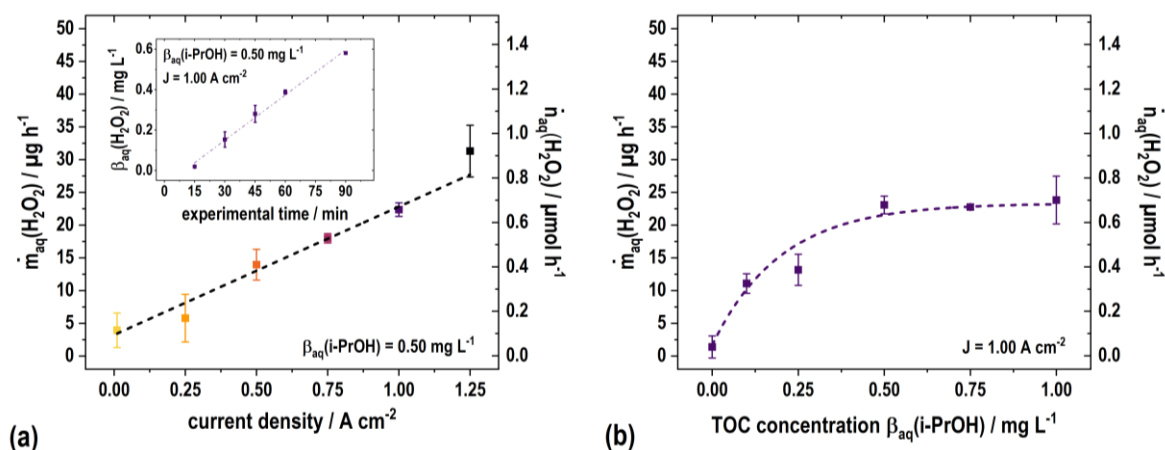


Fig. 2-7. Formation of hydrogen peroxide during electrochemical ozonation of aqueous solutions containing defined levels of i-PrOH. **(a)** Over the course of 90 min, a linear increase in hydrogen peroxide concentration can be measured in the reaction vessel when treating a $0.50 mg L^{-1}$ i-PrOH solution at a current density of $1.00 A cm^{-2}$ (inset graph). Keeping the initial TOC level at a constant value of $0.50 mg L^{-1}$, the resulting formation rates $\dot{m}_{aq}(H_2O_2)$ and $\dot{n}_{aq}(H_2O_2)$ increase linearly with elevated current densities from $3.9 \pm 2.6 \mu g h^{-1}$ in stand-by operation up to $31.2 \pm 3.9 mg h^{-1}$ for $J = 1.25 A cm^{-2}$. **(b)** For a fixed current density of $J = 1.00 A cm^{-2}$, a variation of TOC concentration leads to an increase in H_2O_2 production until plateauing at approx. $23 \mu g h^{-1}$.

As the increase in H_2O_2 concentration also follows a linear trend with time ($R^2 > 0.95$ for all experiments), formation rates were obtained in the same manner as for the other ROS. The progression of measured H_2O_2 concentration over the course of the experimental time is exemplarily depicted in Fig. 2-7(a) (inset graph) for $J = 1.00 A cm^{-2}$ and $\beta_{aq}(i-PrOH) = 0.50 mg L^{-1}$. The obtained slope of $7.46 \mu g L^{-1} min^{-1}$ equals a formation rate of $22.4 \mu g h^{-1}$ for the given reaction vessel, which serves as a common reference point in both Figs. 2-7(a) and (b). By evaluating different current densities, a linear approximation for the H_2O_2 formation rate is obtained ($R^2 = 0.978$) and enables a confident estimation of peroxide concentrations for different operational setpoints. Even in stand-by operation, trace amounts of peroxide evolve due to a small protection current and therefore electrolyzer activity. However, it has been reported that linearity in electrochemical H_2O_2 evolution over longer periods of time is not necessarily given due to possible subsequent reactions such as oxidation to oxygen at certain electrode materials [72,175].

When the PEM electrolyzer is operated without adding i-PrOH to the reaction vessel, minimal amounts of hydrogen peroxide can still be detected in a range of $1.4 \mu g h^{-1}$. This may result from traces of residual organic compounds within the ultrapure water used for preparation.

However, as soon as a carbon source is deliberately introduced into the system, a notable increase in H_2O_2 levels is measured. Varying the TOC level at a constant current density of 1.00 A cm^{-2} leads to an increase of the H_2O_2 formation rate up to only $23 \mu\text{g h}^{-1}$ for i-PrOH concentrations $\geq 0.50 \text{ mg L}^{-1}$ (Fig. 2-7(b)), indicating that the rate of i-PrOH oxidation and therefore H_2O_2 formation depends on the amount of dissolved organic matter. For higher concentrations of i-PrOH no significant increase in peroxide evolution is observed, which is in accordance with previous findings [16].

2.3.3 Correlation of ORP signals with ROS concentrations

Conventionally, the oxidation-reduction potential (ORP) provides a viable sum parameter given by a mixed potential to describe the disinfection efficacy of a given water sample without distinguishing the actual ROS composition. Fig. 2-8 emphasizes this relationship by plotting the measured ORP signal as a function of different concentrations for individual ROS. Herein, an increase in ozone concentration is accompanied by a proportionate increase of the ORP signal and can be described by a linear relationship.

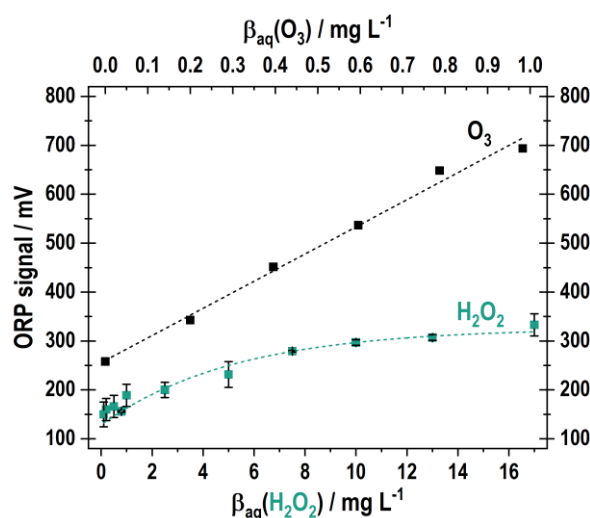


Fig. 2-8. Signal of a Pt ORP electrode as a function of the dissolved ROS concentration. For ozone (black) ORP values between approx. 250 and 700 mV were obtained for a range from 0.0 to 1.0 mg L^{-1} . For hydrogen peroxide (turquoise) a maximum ORP signal of $333 \pm 23 \text{ mV}$ is observed, albeit applying higher oxidant dosages. While a linear correlation between the O_3 concentration and the ORP signal can be approximated up to $1 \mu\text{g L}^{-1}$, H_2O_2 concentrations below 1 mg L^{-1} are not reliably distinguishable.

Ozone dosages as low as 0.2 mg L^{-1} are known to provide sufficient oxidative strength for process water sanitization and yield ORP signals of only approx. 350 mV. However, due to the strong pH dependence of the ORP value, even moderate changes in pH might be sufficient to mask significant differences in the ROS composition. Furthermore, the presence

ORP signal drop ΔU_{ORP} . Furthermore, the addition of higher amounts of H_2O_2 is accompanied by a small decrease in pH. **(b)** Effect of the $n_0(\text{H}_2\text{O}_2)/n_0(\text{O}_3)$ ratio on the ORP signal drop for different ozone levels. Piecewise linear regression functions are used to highlight that the signal drops appear to eventually reach a plateau with an increasing $n_0(\text{H}_2\text{O}_2)/n_0(\text{O}_3)$ ratio. The transition region (purple and grey bars) depends on the total amount of dissolved ozone.

During ozonation of ultrapure water samples, a steady disinfection performance can be monitored by a near constant ORP signal (Fig. 9(a)). Immediately upon H_2O_2 addition, the potential drops for a few minutes and stabilises at a considerably lower level after 5 to 10 min. This change in ORP provides a signal drop ΔU_{ORP} , which can be attributed to O_3 degradation *via* the fast peroxone process that is initiated when H_2O_2 is added to the O_3 solution [45]. While low amounts of added H_2O_2 coincide with low ΔU_{ORP} values, signal drops of up to 620 mV can be measured with H_2O_2 in broad excess ($n_0(\text{H}_2\text{O}_2)/n_0(\text{O}_3) = 13.5$). In these cases a pronounced decrease in pH of up to 0.5 units is observed, while experiments with a lower overall oxidant concentration are accompanied by almost insignificant changes in pH ($\Delta\text{pH} \leq 0.05$). In pretrials, it was possible to rule out that this effect is caused by minor amounts of phosphoric acid as a common stabilizing agent in H_2O_2 solutions. However, both these potentiometric measurements are limited with respect to their accuracy in ultrapure water due to the extremely low conductivity of the surrounding medium.

Since the ORP value changes with pH, comparing the effect of different ROS compositions is only meaningful referring to equal pH environments. As under the given experimental conditions ozone constitutes the main oxidant contributing to the ORP value, the Nernst equation for its redox behavior can be employed to account for the observed change in pH [179] and approximate a correction function for the measured raw ORP values (Eq. 2-4). While this correction is only of minor importance in ideal ultrapure water environments, it may be of high significance in other media.

$$\Delta U_{\text{ORP}} = \Delta U_{\text{ORP,measured}} + 59 \text{ mV} \cdot \Delta\text{pH} \quad (\text{Eq. 2-4})$$

From Fig. 2-9(b) it can be noted that the ORP signal drop increases with an increasing amount of H_2O_2 compared to the dissolved O_3 , until it reaches a plateau as indicated by piecewise linear functions. This transition occurs at $n_0(\text{H}_2\text{O}_2)/n_0(\text{O}_3) \approx 2.2$ for the $100 \mu\text{g L}^{-1}$ ozone solution and at $n_0(\text{H}_2\text{O}_2)/n_0(\text{O}_3) \approx 0.85$ for the $50 \mu\text{g L}^{-1}$ solution.

2.4 Conclusion

This study addresses the formation of ozone, hydroxyl radicals and hydrogen peroxide during the operation of an electrolytic ozone generator for ultrapure water disinfection. For all

reactive oxygen species, the suitability of colorimetric detection assays based on DPD, HTA and TiOSO_4 was evaluated to quantify the respective cross-sensitivities among each other through linear calibration functions. Thus, a stepwise approach was proposed in order to determine the real concentration of all three ROS under investigation and to enable a predictive assessment of ROS evolution.

Specifically, we demonstrated that elevated formation rates for dissolved ozone are only obtained when the applied current density exceeds 0.50 A cm^{-2} . Conversely, the formation of $\cdot\text{OH}$ due to ozone decay shows a direct correlation amongst the entire current density range under investigation. Even minor quantities of dissolved organic carbon result in the observable generation of hydrogen peroxide. By knowing the concentration of dissolved isopropyl alcohol (given as the TOC level), the formation rate of hydrogen peroxide can be directly estimated based on the applied current density. However, when the TOC level surpasses 0.50 mg L^{-1} , no further increase in the formation rate of hydrogen peroxide occurs, remaining steady at $23 \mu\text{g h}^{-1}$ for $J = 1.00 \text{ A cm}^{-2}$.

Considering that even low concentrations of produced H_2O_2 are capable of strongly affecting the O_3 content and eventually the ORP reading, the underlying TOC level and composition constitute a crucial parameter for ultrapure water ozonation. If neglected, unnecessarily high amounts of ozone need to be produced to destroy residual organic matter, thus, distinct attention must be paid to monitoring the feed water quality.

Chapter 3: Evaluating Platinum-Based Ionic Polymer Metal Composites as Potentiometric Sensors for Dissolved Ozone in Ultrapure Water Systems

Roman Grimmig, Philipp Gillemot, Simon Lindner, Philipp Schmidt, Samuel Stucki, Klaus Günther, Helmut Baltruschat, Steffen Witzleben

published in

Advanced Materials Technologies, Volume 8, Issue 12, S. 2202043, **2023**

DOI: [10.1002/admt.202202043](https://doi.org/10.1002/admt.202202043)

Summary of the publication

In ultrapure water storage and distribution systems, the presence of ozone is intended to maintain a sanitized state, whereas the water used in subsequent processes must be ozone-free to avoid undesired interferences, i.e. oxidation or degradation of added ingredients [11,15].

This publication focused on the development of a sensor material for potentiometric measurements, which allows for a sensitive detection of dissolved ozone down to trace concentrations. Nafion™ acts both as a polymer electrolyte and proton exchange membrane and therefore allows for the incorporation of cations. In previous studies, noble metals were deposited on and in PEM substrates *via* electroless deposition and were shown to act as amperometric gas sensors. The most promising results were obtained for ionic polymer metal composite (IPMC) materials using platinum that were synthesized for sensors intended for hydrogen detection [98,180,181]. In this study, an easy to use yet reliable impregnation-reduction method [182,183] was developed that controls relevant synthesis conditions. To obtain different physico-chemical properties of IPMC materials (i.e. metal loading, metal layer thickness and particle size), the synthesis conditions had to be systematically altered (i.e. noble metal concentration of the impregnation solution, selected reducing agent and concentration, a supporting solution beneath the PEM).

A total of 25 IPMC materials were prepared using 2.0, 4.5 and 10.0 mmol L⁻¹ Pt-containing solutions during impregnation and were reduced using either KBH₄, NaBH₄ or hydrazine, each in different concentrations. Furthermore, a cavity beneath the substrate was filled with ultrapure water or electrolyte-containing solutions during synthesis. The so-obtained sensor materials vary in visual appearance from translucent gray to a solid black and to a silver-colored, mirror-like front finish.

A dependable Pt loading quantification of an IPMC sensor material is often related to a digestion procedure in *aqua regia* [184,185] and involves an irreversible sample destruction. Therefore, a radiographic, non-destructive detection approach was developed for metal loading estimation. In applications that range from membranes used in fuel cells to heavily loaded IPMCs for nano-actuator applications, loadings between 0.1 up to 4 mg cm⁻² are expected [98,182,186]. The grayscale of a radiographic image was shown to accurately describe the platinum content obtained with a reference method with up to R² = 0.876, when other absorbing elements that are used during sample preparation are omitted. As a result, Pt loadings of 0.3 mg cm⁻² can be estimated with a sufficient accuracy.

A single-sided Pt deposition was confirmed within the first few micrometers of the usually 178 μm thick Nafion™ membrane. Depending on the synthesis conditions, the obtained Pt layer thicknesses are within a range of 2.2 to 12.6 μm, which is in accordance with the results

achieved by other research groups [187,188]. However, the so-obtained Pt particles are 40 to 90 nm in size which is larger in comparison to other research that yielded particles with a diameter of less than 10 nm and were prepared at higher temperatures [185,189,190].

For the potentiometric ozone-sensing application, a setup was developed that uses an iridium oxide (IrO_x) electrode as a stable reference electrode [191–193]. Doping the water with different amounts of ozone resulted in sensor voltage increases that reliably resumed to the initial voltage baseline after several hours. A plot of the resulting maximum voltage increases (corrected by the natural ozone-decay) as a function of the time-dependent ozone-concentration (confirmed *via* iodometric titration as reference analysis) yields a response curve that can be explained by a pseudo-isotherm. Isotherm in that sense, as the platinum surface interacts with the naturally decomposing ozone in a reactive way, but yielding no real equilibrium (hence pseudo). In order to derive the most apparent and probable underlying adsorption model for ozone with the platinum surface, Langmuir, Freundlich, Redlich-Peterson and Sips pseudo-isotherms were evaluated using the Akaike information criterion [194,195]. With this approach, an objective measure was introduced to spot and prevent overfitting caused by more sophisticated regression models. For the four models under investigation, the Langmuir pseudo-isotherm was therefore found to be the most probable model amongst the selected. The Langmuir parameters K_L and q_{\max} represent the energy of adsorption and the upper limit for an observable change in voltage when all binding sites on the sensor surface are occupied due to ozone interaction [196]. Sensor materials with high K_L values exhibit a steeper calibration curve while sensors with a higher q_{\max} can be used in a broader concentration range. Limited by electronic noise, LOD and LOQ values for ozone can be derived for all sensors that allow for a qualitative and quantitative ozone detection. Averaging over all sensors prepared in this study, a LOD of $2.9 \mu\text{g L}^{-1}$ and LOQ of $9.9 \mu\text{g L}^{-1}$ can be stated which is sufficient for most sensing applications.

To predict physico-chemical and sensing properties from given synthesis conditions, underlying correlations were extracted from the fractional factorial dataset. Although not all factor interactions can be resolved with this approach, high-value resources can be limited and established models still exhibit significant effects [197]. For the metal loading of the final IPMC, a model could be extracted that predicts the value based on the initial Pt solution concentration used during impregnation, the use of either hydrazine or a borohydride salt and the option to renew the reductant during the reduction part of the procedure ($R^2 = 0.952$).

It was shown that the prediction of certain parameters e.g. noble metal loading that would generally require laborious analyses could be either pre-modeled or non-destructively verified by a radiographic method. As a result, sensor materials can be prepared more easily and sustainable and used for secure potentiometric ozone measurements.

Author	Contribution	CRedit authorship contribution statement
Roman Grimmig (First author)	60%	Conceptualization, Methodology, Formal analysis, Investigation, Data Curation, Visualization, Writing - Original Draft.
Philipp Gillemot (Co-author 1)	10%	Conceptualization, Methodology, Data Curation, Visualization, Writing - Original Draft.
Simon Lindner (Co-author 2)	5%	Formal analysis.
Philipp Schmidt (Co-author 3)	5%	Formal analysis.
Samuel Stucki (Co-author 4)	5%	Conceptualization, Writing – Review & Editing.
Klaus Günther (Co-author 5)	5%	Supervision, Writing - Review & Editing.
Helmut Baltruschat (Co-author 6)	5%	Supervision, Writing - Review & Editing.
Steffen Witzleben (Co-author 7)	5%	Funding acquisition, Resources, Supervision, Writing - Review & Editing.

Chapter 4: Operating an ozone-evolving PEM electrolyser in tap water: A case study of water and ion transport

Roman Grimmig, Philipp Gillemot, Samuel Stucki, Klaus Günther, Helmut Baltruschat, Steffen Witzleben

published in

Separation and Purification Technology, Volume 292, 121063, **2022**

DOI: [10.1016/j.seppur.2022.121063](https://doi.org/10.1016/j.seppur.2022.121063)

Summary of the publication

Nowadays, a commonly used technique to sanitize ultrapure water with ozone is the use of PEM water electrolysis. The spatial separation of anolytic and catholytic electrolysis compartments by a polymer electrolyte membrane does not only provide a safety feature in terms of gas evolution, it also enables the selective oxidative treatment of the feed water [129,198]. With the application of an ozone-evolving electrolyzer in a more natural water (i.e. tap water), undesired organic compounds as well as a biological pollution can be effectively countered [199,200]. Its application is mainly limited to the use of ultrapure water to achieve a sufficient long-time stability and is strongly influenced by charge carriers such as Na^+ , K^+ , Mg^{2+} and Ca^{2+} in tap water. Consequently, this study focused on the influence of the transport phenomena of these charge carriers in drinking or tap water on the operation of the PEM electrolyzer. Similar transport effects were already discussed in the literature in the related context of e.g. fuel cells and redox flow batteries [201–204]. The scope of this part of the study was therefore to quantify ion and water permeation in an ozone-evolving PEM-electrolyzer. The focus is on varying conditions of use that occur during operation or in stand-by mode (current density = 0.01 to 1.25 A cm⁻²) with an emphasis on treatment of batchwise operation, representing a stagnant water.

The operation of an electrolyzer in an environment that differs from ultrapure water is often impeded by the formation of cathodic scale [205]. However, as a detailed investigation of feed water ion transport and its fate was still missing, a certain emphasis was put on a constructive approach to mitigate unwanted ion transports. Consequently, the previously developed PEM electrolyzer with its structured MEA arrangement was upgraded with an optional auxiliary cathode [206] within the anolytic compartment and operated with waters of different hardness levels from ion-free ultrapure water to a hard tap water [207].

When operating a PEM electrolyzer, a macroscopic water transport from the anodic to the cathodic compartment can be observed. This water permeation intensifies with an increasing current density and could therefore be shown to only occur during an electrolysis operation. This conforms with a stand-by mode with a nearly negligible electrical current and a correspondingly low water transport below 105 $\mu\text{mol H}_2\text{O h}^{-1} \text{ cm}^{-2}$ (equals 2.6 mg h⁻¹ for this electrolyzer configuration). A variation of the underlying anolytic ion concentrations (representing a changing in water hardness) was performed, ranging from ultrapure water to a hard tap water (total cation equivalents $\Sigma c_{\text{ion, eq}} = 114.35 \text{ mEq L}^{-1}$). However, an influence of the kind of charge carrier on the water transport cannot be stated. Water transport occurs under ambient conditions with an electro-osmotic drag coefficient (EOD) of 2.55, independent of the water composition.

Analytically present cations from dissolved minerals represent additional potential charge carriers apart from the *in situ* generated protons that contribute to the overall current. It was noticed that ion transport from the anodic to the cathodic compartment showed a discrimination as for higher concentrated 'harder' model tap waters a transport of K^+ was favored over the transport of the other ions Na^+ , Ca^{2+} and Mg^{2+} . These variations could be attributed to the ion mobility of the respective ions in water probably resulting from a concentration polarization at the anode/PEM interface. This is supported by a series of analyses that showed that especially at a low current density, a higher percentage of the total current is transported by other ions than protons. The higher the tap water ion concentration in the anolyte (equaling the water hardness), the higher its contribution to the current. As a result, a current density of 0.25 A cm^{-2} and a hard model water led to a H^+ current participation of only $93.5 \pm 0.4\%$, while operating the PEM electrolyzer at a high current density of 1.25 A cm^{-2} and a 'soft' model tap water yielded a H^+ current share of $99.4 \pm 0.1\%$. This is especially important, as the transport of *in situ* generated protons are transported through the PEM and, in a generalized equation, discharged to hydrogen gas. As this reaction can also be formulated as a neutralization reaction of cathodically produced hydroxide anions that result from water decomposition, charge carriers other than protons directly impact on the pH of both compartments.

The operation of a PEM electrolyzer in hard water directly leads to an anolytic acidification due to non-transported and therefore remaining protons, while cathodic hydroxide anions are not neutralized and basify the cathodic compartment. Permeating hardeners Ca^{2+} and Mg^{2+} find predestined alkaline conditions to form precipitates when the catholyte is not buffered in an acidic pH range or exposed to air, enabling a CO_2 ingestion. Dissolved carbon dioxide and therefore carbonate source enables Ca^{2+} and Mg^{2+} to form hydroxides and carbonates of different crystallographic structures such as aragonite and calcite (both $CaCO_3$), brucite ($Mg(OH)_2$) and portlandite ($Ca(OH)_2$) right on top of the cathodes at the electrode / PEM interface, ultimately impairing long-term stability.

However, a constructive approach was chosen to counter the disadvantageous tap water ion crossover with introducing an auxiliary cathode within the anolytic compartment. Although only $3 \pm 1\%$ of the total current flows via this additional anolytic cathode, a reduction in ion crossover of $18 \pm 4\%$ was measured without preference for any cationic species involved. The electric field introduced close to the anode/PEM interface is expected to improve the concentration polarization observed during charge carrier discrimination.

The results show that potential charge carriers present in tap water contribute to undesired ion crossover and can be modeled with a known ion concentration. The water crossover can likewise be modeled as a direct function of the applied current and allows the derivation of a tangible water volume that may require a constructive measure in scaled-up application. The

introduction of an anolytic cathode reduces ion cross over which also means less influence on a pH gradient or cathodic scale formation. Ultimately, the presented results allow for a profound estimation of the optimal operation conditions when using this ozone-evolving PEM water electrolyzer in a tap water of a certain quality.

Author	Contribution	CRedit authorship contribution statement
Roman Grimmig (First author)	65%	Conceptualization, Methodology, Formal analysis, Investigation, Data Curation, Visualization, Writing - Original Draft.
Philipp Gillemot (Co-author 1)	10%	Conceptualization, Methodology, Formal analysis, Data curation, Visualization, Writing – original draft.
Samuel Stucki (Co-author 2)	10%	Conceptualization, Writing – Review & Editing.
Klaus Günther (Co-author 3)	5%	Supervision, Writing - Review & Editing.
Helmut Baltruschat (Co-author 4)	5%	Supervision, Writing - Review & Editing.
Steffen Witzleben (Co-author 5)	5%	Funding acquisition, Resources, Supervision, Writing - Review & Editing.

Chapter 5: Discussion and Conclusion

5.1 Discussion

The preparation and storage of sanitized process water in the pharmaceutical and semiconductor industry is an important building block in the production of vital and everyday products. Using electrolyzers with functionalized electrodes enables an energy-efficient and demand-actuated production of *in situ* produced disinfectants that does not require energy consuming heat treatments to ensure sterility of the stored process water.

The electrolyzer presented in this work (chapter 4) is equipped with a membrane electrolyte assembly that consists of a Nafion™ polymer electrolyte membrane and PbO₂ coated, porous titanium anodes. On the catalytically active anodic surface, ozone expectedly constitutes the main reactive oxygen species by molar concentration during operation. This configuration legitimates its installation in an ultrapure water production plant, as the O₃ molecule effectively counteracts organic and especially biological pollutants. Ozone slowly decays over time, initiating a self-depleting mechanism, as the degradation-induced by-products hydrogen peroxide and hydroxyl radicals both can actively drain ozone from solution themselves. Ozone-depleting H₂O₂ was however most dominantly observed when 2-propanol was present – which may hint at points of entry for 2-propanol into a UPW production plant. Residues of deliberately chosen and poorly washed away cleaning products that contain isopropyl alcohol will drain freshly produced ozone until all residue is used up, and a detectable ozone production recurs.

Although a significant hydroxyl radical formation was detected that could be described by a function of the applied current density, it is worth stressing that this is not due to an anodic production of ‘free radicals’ as it is known from boron-doped diamond electrodes, but exclusively from decay of dissolved ozone. Hydroxyl radicals can then act as an even more potent oxidant and could therefore be more capable of degrading critical compounds than ozone alone. Their range, however, remains severely limited due to the short lifespan. For a transfer of the PbO₂-based PEM electrolyzer technology from the UPW environment into an application that would focus the local degradation of other, persistent organic compounds, this should be considered.

The detection of ozone has always been a tricky endeavor, especially when the presence of other reactive oxygen species cannot be ruled out. As shown, various operating conditions can occur that can severely reduce the concentration of electrochemically produced ozone. A single, isolated message hinting at a too low ozone concentration within the UPW storage tank may overlook or even cover up the actual causes. For a strategic monitoring of an ultrapure water production plant with cold water storage and proper process control, ROS quantification assays are best performed at various measuring points instead of consulting only one point. For obvious reasons, an ozone sensor should be placed downstream right after the ozone-

evolving unit, ensuring that the ozone production is not impeded by electronic signaling of the control system. Furthermore, for a comprehensive production and storage system surveillance, it would be desirable to place even more sensors at critical crossings or junctions. Amperometric state-of-the-art sensors for selective O_3 detection do have their *raison d'être* for being a robust and reliable method - the disadvantage of these commercially available devices however are the high acquisition costs, impeding a lavish distribution at random point within the system. The preparation of IPMCs that can be used for low-cost potentiometric evaluation of oxidant concentration represent a new and interesting alternative: the sensor preparation development shown in this study proposes a simple impregnation-reduction preparation using only common laboratory equipment which easily enables the reproducible production of numerous small sensor materials.

This provides an obvious advantage in terms of strategic positioning of many small sensors and allows for a spatially resolved sensor response of oxidant distribution within the ultra-pure water production and storage system. The relationships between synthesis conditions and physico-chemical properties highlighted in this work in chapter 3, clearly depict a reliable estimation for the potentiometric response in ozone detection. Implementing this kind of decentralized potentiometric detection system allows for the detection of minor changes in the process water quality and can therefore identify potential sinks for the ozone concentration. As a real-time detection of ozone is possible, this poses another advantage over single, centralized detection systems, even when a valve-actuated re-routing of the process water is used for analysis. With the data obtained by numerous sensors, additional hydrodynamic properties can be considered and allow for an insight into different constructive measures for UPW production plants. In an advanced step, the spatially resolved distribution of ozone and its decay might be used to characterize and model individual production plants in advance.

As has been outlined in chapter 2 in this work, the different observed reactive oxygen species do not occur in parallel in a high local or temporal proximity, therefore the presence of different ROS can be qualified and quantified, although the exact species may not be identified. The IPMC then suffers from this flaw and the sensor acts as a tiny ORP probe when ozone is not the only species present. Still, a statement about the oxidative state of the water is possible, referring to known so-called killing rates for biological contaminants. In that case, a sample at this measurement point of the UPW water loop can be withdrawn and analyzed with a photometric assay to identify the dominating reactive oxygen species.

Different restrictions apply when the anolytic part of this PEM electrolyzer is put into a potentially stagnant tap water environment. The presence of dissolved minerals both drastically raise the electric conductivity of the process water and provide a large source of cations that interact with the functional groups of the polymer electrolyte membrane. This key

feature of converting the surface region of membrane from its H^+ -form into a Pt^{2+} -form has been taken advantage of during the IPMC sensor preparation, and is more a restraint for a functional electrolyzer. Due to possibly different analytic and catholytic compositions, tap water ions will get transported through the membrane due to osmotic effects, resulting in the formation of a pH gradient across the membrane. Hence the increase in cell voltage is virtually inevitable. If an acidly buffered catholyte is used in order to effectively suppress the formation of cathodic scale, a large diffusion into the anolyte can be expected – if the buffer is omitted, the scale formation can clog and damage cell components by blocking the Nafion™ membrane.

Therefore, the composition of transport of tap water ions was narrowed down to the ion-mobility controlled cation diffusion to the anode/PEM interface. Hindering cations from reaching the interface by means of the developed auxiliary cathode within the analytic compartment has proved to be an effective measure to decelerate undesired ion migration. Improving and harnessing this effect can be expected to elongate the usable lifetime of this electrolyzer in a tap water environment. Furthermore, the influence of tap water cations in their role as charge carriers has been investigated. Although, there is a large variety of water ingredients present that are known to be affected by anodic ozone evolution. The corresponding and inherently abundant anions in drinking water (e.g. chloride, bromide, nitrate, sulphate, carbonate) are mostly resistant to ozone degradation, but may be oxidized to form compounds such as the oxyhalides chlorate and bromate, with the latter known to harmfully affect the human health. As bromides are predominantly more present in tap waters close to the coastline, an ozonation of (stagnant) tap water should not be favored in these regions at this stage of development.

Another point that needs addressing is the presence and elevated levels of dissolved organic species in tap water. *In situ* produced ozone is consumed in degradation reactions and in a stagnant water disinfection application, the limited amount of available dissolved carbon may therefore be degraded within a short period of time. In contrast to that, the application of this PEM electrolyzer in a constant water flow provides a constant source of carbon to the electrolyzer and may easily drain the ozone concentration before all biological pollution is effectively removed. In order to develop an ozone-evolving PEM electrolyzer for a decentralized disinfection application of tap water, the current (density) dependent ozone production rate should be matched to the expected microbial and carbon load of the respective water.

5.2 Conclusion

With this thesis, the understanding of a PEM electrolyzer equipped with PbO_2 anodes intended for ozone generation was deepened regarding its evolution of reactive oxygen species during operation, the detection of these species and its application in a tap water environment. Although a significant progress was achieved in each facet of this topic, each chapter can only constitute an excerpt of the overall topics that were addressed.

The generation of ozone comes with a variety of other reactive oxygen species than those that were focused in this work. However, this work already provides an approach to model an entire ultrapure water production plant featuring storage and distribution system. An even more differentiated detection might be used for the acquisition of species that were omitted in this study. As a helpful tool for this task, the suitability of different kinds of low-cost potentiometric sensors should be focused.

The development of a simple preparation of platinum-based ionic polymer metal composites yielded sensors that can be useful in PEM electrolyzers that strictly separate the compartments responsible for ozone and hydrogen evolution. However, in order to obtain sensor materials that are also appropriate to monitor the ozone concentration in the presence of hydrogen (i.e. in undivided electrolysis devices), a gold-based IPMC could be a feasible material. With this approach, a similar potentiometric ozone detection material could be synthesized with inherent resistance to the influence of dissolved hydrogen. If the optimum synthesis parameters are to be derived by a structured plan (design of experiments), a particular emphasis on the detection of particle size could lead to both significant and relevant results.

Finally, the application of the electrolyzer in tap water needs to address the potential formation of critical oxyhalides such as chlorate and bromate. As the electrolyzer however features a spatially divided anodic and cathodic department, the electrochemical reduction of *in situ* produced oxyhalides by means of the inherently present catholyte should be evaluated. A significant reduction of anodically formed oxyhalides could be achieved on catalytically modified cathodes. In another iteration, the ozonated water from the analytic compartment that may be contaminated with oxyhalides can be re-routed to the catholytic compartment of the very same electrolyzer and – by subsequent reduction – eventually provide both a sanitized and potable drinking water.

Bibliography

- [1] DIN 2000:2017-02 Zentrale Trinkwasserversorgung - Leitsätze für Anforderungen an Trinkwasser, Planung, Bau, Betrieb und Instandhaltung der Versorgungsanlagen, (2017).
- [2] A.F. Danil De Namor, Water purification: From ancient civilization to the XXI Century, *Water Sci. Technol. Water Supply*. 7 (2007) 33–39. <https://doi.org/10.2166/ws.2007.004>.
- [3] H. Abu Hasan, M.H. Muhammad, N.I. Ismail, A review of biological drinking water treatment technologies for contaminants removal from polluted water resources, *J. Water Process Eng.* 33 (2020) 101035. <https://doi.org/10.1016/j.jwpe.2019.101035>.
- [4] Y. Boivin, B. Massieux, A.M. Breure, F.P. Van Den Ende, G.D. Greve, M. Rutgers, W. Admiraal, Effects of copper and temperature on aquatic bacterial communities, 71 (2005) 345–356. <https://doi.org/10.1016/j.aquatox.2004.12.004>.
- [5] K. Saeki, T. Kunito, H. Oyaizu, S. Matsumoto, Relationships between Bacterial Tolerance Levels and Forms of Copper and Zinc in Soils, *J. Environ. Qual.* 31 (2002) 1570–1575. <https://doi.org/10.2134/jeq2002.1570>.
- [6] P. Rochelle, J. Clancey, The evolution of microbiology in the drinking water industry, *J. / Am. Water Work. Assoc.* 98 (2006) 163–191. <https://doi.org/10.1002/j.1551-8833.2006.tb07614.x>.
- [7] R. Koch, Wasserfiltration und Cholera, *Zeitschrift Für Hyg. Und Infekt.* 14 (1893) 393–426. <https://doi.org/10.1007/BF02284326>.
- [8] TrinkwV:2023-06-20 Zweite Verordnung zur Novellierung der Trinkwasserverordnung (Artikel 1 Verordnung über die Qualität von Wasser für den menschlichen Gebrauch (Trinkwasserverordnung - TrinkwV)), (2023).
- [9] X. Zhang, Y. Yang, H.H. Ngo, W. Guo, H. Wen, X. Wang, J. Zhang, T. Long, A critical review on challenges and trend of ultrapure water production process, *Sci. Total Environ.* 785 (2021) 147254. <https://doi.org/10.1016/j.scitotenv.2021.147254>.
- [10] S. Stucki, D. Schulze, D. Schuster, C. Stark, Ozonization of purified water systems, *Pharm. Eng.* 25 (2005) 40–56. http://apaco.ch.futura.ch-meta.net/xp_wysiwyg_media/jspe2005vol25no1_ozonization-of-purified-water-systems.pdf.
- [11] European Pharmacopeia, 9th ed., 2017.
- [12] United States Pharmacopoeia, Water for Pharmaceutical Purposes <1231>, USP 40 - NF35, 2017.
- [13] ASTM D 1196:2006 Standards for Laboratory Reagent Water, reapproved 2018, (2018).
- [14] ISO 3696:1987 Wasser für analytische Zwecke; Anforderungen und Prüfungen, (1987).
- [15] M. Florjanič, J. Kristl, Microbiological quality assurance of purified water by ozonization of storage and distribution system, *Drug Dev. Ind. Pharm.* 32 (2006) 1113–1121. <https://doi.org/10.1080/03639040600920614>.
- [16] S. Stucki, H. Baumann, Application of Electrochemical Ozone Generators in Ultrapure Water Systems, in: *Process Technol. Water Treat.*, Plenum Press, New York, 1988: pp. 191–201. https://doi.org/https://doi.org/10.1007/978-1-4684-8556-1_19.
- [17] T. Ohmi, T. Isagawa, T. Imaoka, I. Sugiyama, Ozone Decomposition in Ultrapure Water and Continuous Ozone Sterilization for a Semiconductor Ultrapure Water System, *J. Electrochem. Soc.* 139 (1992) 3336–3345. <https://doi.org/10.1149/1.2069075>.
- [18] A.M. Gorito, J.F.J.R. Pesqueira, N.F.F. Moreira, A.R. Ribeiro, M.F.R. Pereira, O.C. Nunes, C.M.R. Almeida, A.M.T. Silva, Ozone-based water treatment (O₃, O₃/UV, O₃/H₂O₂) for removal of organic micropollutants, bacteria inactivation and regrowth prevention, *J. Environ. Chem. Eng.* 9 (2021) 10–14. <https://doi.org/10.1016/j.jece.2021.105315>.
- [19] M. Florjanič, J. Kristl, The control of biofilm formation by hydrodynamics of purified water in industrial distribution system, *Int. J. Pharm.* 405 (2011) 16–22.

<https://doi.org/10.1016/j.ijpharm.2010.11.038>.

- [20] S. Jha, S. Anand, Development and Control of Biofilms: Novel Strategies Using Natural Antimicrobials, *Membranes* (Basel). 13 (2023). <https://doi.org/10.3390/membranes13060579>.
- [21] Marc W. Mittelman, Bacterial Biofilms in Pharmaceutical Water Systems, in: Maik W. Jornitz (Ed.), *Filtr. Purif. Biopharm. Ind.* Third Ed., 3rd Editio, CRC Press, Boca Raton, 2019: p. 21.
- [22] E.M. Cuerda-Correa, M.F. Alexandre-Franco, C. Fernández-González, Advanced oxidation processes for the removal of antibiotics from water. An overview, *Water* (Switzerland). 12 (2020). <https://doi.org/10.3390/w12010102>.
- [23] D.A. Armstrong, R.E. Huie, W.H. Koppenol, S. V. Lyman, G. Merenyi, P. Neta, B. Ruscic, D.M. Stanbury, S. Steenken, P. Wardman, Standard electrode potentials involving radicals in aqueous solution: Inorganic radicals (IUPAC Technical Report), *Pure Appl. Chem.* 87 (2015) 1139–1150. <https://doi.org/10.1515/pac-2014-0502>.
- [24] R. Criegee, Mechanismus der Ozonolyse, *Angew. Chemie.* 87 (1975) 765–771. <https://doi.org/10.1002/ange.19750872104>.
- [25] Z. Hassan, M. Stahlberger, N. Rosenbaum, S. Bräse, Criegee Intermediates Beyond Ozonolysis: Synthetic and Mechanistic Insights, *Angew. Chemie - Int. Ed.* 60 (2021) 15138–15152. <https://doi.org/10.1002/anie.202014974>.
- [26] M.H. Almatarneh, I.A. Elayan, M. Altarawneh, J.W. Hollett, Hydration and Secondary Ozonide of the Criegee Intermediate of Sabinene, *ACS Omega.* 3 (2018) 2417–2427. <https://doi.org/10.1021/acsomega.7b02002>.
- [27] G. V Buxton, P.R.S.L. A, Nanosecond pulse radiolysis of aqueous solutions containing proton and hydroxyl radical scavengers, *Proc. R. Soc. London. A. Math. Phys. Sci.* 328 (1972) 9–21. <https://doi.org/10.1098/rspa.1972.0065>.
- [28] C.C. Winterbourn, Toxicity of iron and hydrogen peroxide: the Fenton reaction, *Toxicol. Lett.* 82–83 (1995) 969–974. [https://doi.org/10.1016/0378-4274\(95\)03532-X](https://doi.org/10.1016/0378-4274(95)03532-X).
- [29] H.J.H. Fenton, LXXIII. - Oxidation of Tartaric Acid in presence of Iron, *J. Chem. Soc. Trans.* 65 (1894) 899–910. <https://doi.org/10.1039/CT8946500899>.
- [30] D. Armstrong, R.E. Huie, W.H. Koppenol, S. V Lyman, “ Standard electrode potentials involving radicals in aqueous solution : inorganic radicals (IUPAC Technical Report)” Steenken and Peter Wardman *Pure and Applied Chemistry Supporting Information Data Sheets* 1-117 Supplementary Data Sheets S1-S12, 12 (n.d.) 1–252.
- [31] A. Kapalka, H. Baltruschat, C. Comninellis, Electrochemical Oxidation of Organic Compounds Induced by Electro-Generated Free Hydroxyl Radicals on BDD Electrodes, in: *Synth. Diam. Film. Prep. Electrochem. Charact. Appl.*, John Wiley & Sons, Ltd, Hoboken, 2011: pp. 237–260. <https://doi.org/10.1002/9781118062364.ch10>.
- [32] A. Kapalka, G. Fóti, C. Comninellis, The importance of electrode material in environmental electrochemistry. Formation and reactivity of free hydroxyl radicals on boron-doped diamond electrodes, *Electrochim. Acta.* 54 (2009) 2018–2023. <https://doi.org/10.1016/j.electacta.2008.06.045>.
- [33] D. Gardoni, A. Vailati, R. Canziani, Decay of Ozone in Water: A Review, *Ozone Sci. Eng.* 34 (2012) 233–242. <https://doi.org/10.1080/01919512.2012.686354>.
- [34] M.D. Gurol, P.C. Singer, Kinetics of Ozone Decomposition: A Dynamic Approach, *Environ. Sci. Technol.* 16 (1982) 377–383. <https://doi.org/10.1021/es00101a003>.
- [35] S. Morooka, K. Kusakabe, J. ichiro Hayashi, K. Isomura, K. Ikemizu, Decomposition and Utilization of Ozone in Water Treatment Reactor with Ultraviolet Radiation, *Ind. Eng. Chem. Res.* 27 (1988) 2372–2377. <https://doi.org/10.1021/ie00084a022>.
- [36] A.N. Ignatiev, A.N. Pryakhin, V. V. Lunin, Numerical simulation of the kinetics of ozone decomposition in an aqueous solution, *Russ. Chem. Bull.* 57 (2008) 1172–1178. <https://doi.org/10.1007/s11172-008-0146-0>.

- [37] G. Merényi, J. Lind, S. Naumov, C. Von Sonntag, Reaction of ozone with hydrogen peroxide (peroxone process): A revision of current mechanistic concepts based on thermokinetic and quantum-chemical considerations, *Environ. Sci. Technol.* 44 (2010) 3505–3507. <https://doi.org/10.1021/es100277d>.
- [38] H. Tomiyasu, H. Fukutomi, G. Gordon, Kinetics and Mechanism of Ozone Decomposition in Basic Aqueous Solution, *Inorg. Chem.* 24 (1985) 2962–2966. <https://doi.org/10.1021/ic00213a018>.
- [39] C. Von Sonntag, Advanced oxidation processes: Mechanistic aspects, *Water Sci. Technol.* 58 (2008) 1015–1021. <https://doi.org/10.2166/wst.2008.467>.
- [40] A. Fischbacher, J. Von Sonntag, C. Von Sonntag, T.C. Schmidt, The $\bullet\text{OH}$ radical yield in the $\text{H}_2\text{O}_2 + \text{O}_3$ (peroxone) reaction, *Environ. Sci. Technol.* (2013). <https://doi.org/10.1021/es402305r>.
- [41] G. Merényi, J. Lind, S. Naumov, C. Von Sonntag, The reaction of ozone with the hydroxide ion: Mechanistic considerations based on thermokinetic and quantum chemical calculations and the role of HO_4^- in superoxide dismutation, *Chem. - A Eur. J.* 16 (2010) 1372–1377. <https://doi.org/10.1002/chem.200802539>.
- [42] L.M. Da Silva, L.A. De Faria, J.F.C. Boodts, Electrochemical ozone production: Influence of the supporting electrolyte on kinetics and current efficiency, *Electrochim. Acta.* (2003). [https://doi.org/10.1016/S0013-4686\(02\)00739-9](https://doi.org/10.1016/S0013-4686(02)00739-9).
- [43] B. Langlais, D.A. Reckhow, D.R. Brink, *Ozone in Water Treatment: Application and Engineering*, Lewis Publishers, Routledge, 1991. <https://doi.org/10.2134/jeq1991.00472425002000040040x>.
- [44] I. Fábián, Reactive intermediates in aqueous ozone decomposition: A mechanistic approach, *Pure Appl. Chem.* 78 (2006) 1559–1570. <https://doi.org/10.1351/pac200678081559>.
- [45] J. Staehelin, J. Hoigné, Decomposition of Ozone in Water: Rate of Initiation by Hydroxide Ions and Hydrogen Peroxide, *Environ. Sci. Technol.* 16 (1982) 676–681. <https://doi.org/10.1021/es00104a009>.
- [46] U. Kogelschatz, Dielectric-barrier Discharges: Their History, Discharge Physics, and Industrial Applications, *Plasma Chem. Plasma Process.* 23 (2003) 1–46. <https://doi.org/10.1023/A:1022470901385>.
- [47] S.W. Benson, Kinetic Considerations of Efficiency of Ozone Production in Gas Discharges, (1959) 405–409. <https://doi.org/10.1021/ba-1959-0021.ch054>.
- [48] U. Kogelschatz, B. Eliasson, W. Egli, From ozone generators to flat television screens: History and future potential of dielectric-barrier discharges, *Pure Appl. Chem.* 71 (1999) 1819–1828. <https://doi.org/10.1351/pac199971101819>.
- [49] B. Eliasson, M. Hirth, U. Kogelschatz, Ozone synthesis from oxygen in dielectric barrier discharges, *J. Phys. D. Appl. Phys.* 20 (1987) 1421–1437. <https://doi.org/10.1088/0022-3727/20/11/010>.
- [50] U. Kogelschatz, B. Eliasson, M. Hirth, Ozone Generation from Oxygen and Air: Discharge Physics and Reaction Mechanisms, *Ozone Sci. Eng.* 10 (1988) 367–377. <https://doi.org/10.1080/01919518808552391>.
- [51] S. Jodzis, M. Zięba, Energy efficiency of an ozone generation process in oxygen. Analysis of a pulsed DBD system, *Vacuum.* 155 (2018) 29–37. <https://doi.org/10.1016/j.vacuum.2018.05.035>.
- [52] Ulrich Kogelschatz, Advanced Ozone Generation, in: S. Stucki (Ed.), *Process Technol. Water Treat.*, Springer, Boston, 1988: pp. 87–118. https://doi.org/10.1007/978-1-4684-8556-1_9.
- [53] D. Bessarabov, H. Wang, H. Li, N. Zhao, *PEM Electrolysis for Hydrogen Production*, Taylor & Francis, Boca Roca, 2015.
- [54] P.A. Christensen, T. Yonar, K. Zakaria, The Electrochemical Generation of Ozone: A Review, *Ozone Sci. Eng.* 35 (2013) 149–167. <https://doi.org/10.1080/01919512.2013.761564>.
- [55] J.C. Santos, P. Cruz, T. Regala, F.D. Magalhães, A. Mendes, High-purity oxygen production by

- pressure swing adsorption, *Ind. Eng. Chem. Res.* 46 (2007) 591–599. <https://doi.org/10.1021/ie060400g>.
- [56] L.M. Da Silva, M.H.P. Santana, J.F.C. Boodts, Electrochemistry and green chemical processes: Electrochemical ozone production, *Quim. Nova.* 26 (2003) 880–888. <https://doi.org/10.1590/s0100-40422003000600017>.
- [57] L.M. Da Silva, W.F. Jardim, Trends and strategies of ozone application in environmental problems, *Quim. Nova.* 29 (2006) 310–317. <https://doi.org/10.1590/s0100-40422006000200023>.
- [58] P.C. Foller, Charles W. Tobias, The Anodic Evolution of Oxygen, *J. Electrochem. Soc.* 129 (1982) 506–515. <https://doi.org/10.1149/1.2123890>.
- [59] G.L. Putnam, R.W. Moulton, ELECTROLYTIC OZONE, 93 (1948) 211–221. <https://doi.org/10.1149/1.2773807>.
- [60] N. Kishimoto, T. Nakagawa, H. Okada, H. Mizutani, Treatment of Paper and Pulp Mill Wastewater by Ozonation Combined with Electrolysis, *J. Water Environ. Technol.* 8 (2010) 99–109. <https://doi.org/10.2965/jwet.2010.99>.
- [61] S. Stucki, G. Theis, R. Kötz, H. Devantay, H.J. Christen, In Situ Production of Ozone in Water Using a Membrel Electrolyzer, *J. Electrochem. Soc.* 132 (1985) 367–371. <https://doi.org/10.1149/1.2113840>.
- [62] S. Stucki, H. Baumann, H.J. Christen, R. Kötz, Performance of a pressurized electrochemical ozone generator, *J. Appl. Electrochem.* (1987). <https://doi.org/10.1007/BF01007814>.
- [63] L.M. Da Silva, L.A. De Faria, J.F.C. Boodts, Green processes for environmental application. Electrochemical ozone production, *Pure Appl. Chem.* 73 (2001) 1871–1884. <https://doi.org/10.1351/pac200173121871>.
- [64] F.J. Beltran, Ozone Reaction Kinetics for Water and Wastewater Systems, Lewis Publishers, Boca Raton, 2003. <https://doi.org/10.1201/9780203509173>.
- [65] J.C.G. Thanos, H.P. Fritz, D. Wabner, The influences of the electrolyte and the physical conditions on ozone production by the electrolysis of water, *J. Appl. Electrochem.* (1984). <https://doi.org/10.1007/BF01269940>.
- [66] D. Wabner, C. Grambow, Reactive intermediates during oxidation of water lead dioxide and platinum electrodes, *J. Electroanal. Chem. Interfacial Electrochem.* 195 (1985) 95–108.
- [67] C.A. Martínez-Huitle, M.A. Quiroz, C. Comninellis, S. Ferro, A. De Battisti, Electrochemical incineration of chloranilic acid using Ti/IrO₂, Pb/PbO₂ and Si/BDD electrodes, *Electrochim. Acta.* 50 (2004) 949–956. <https://doi.org/10.1016/j.electacta.2004.07.035>.
- [68] R. Amadelli, A.B. Velichenko, Lead dioxide electrodes for high potential anodic processes, *J. Serbian Chem. Soc.* 66 (2001) 836–845. <https://doi.org/10.2298/JSC0112835A>.
- [69] K. Arihara, C. Terashima, A. Fujishima, Electrochemical Production of High-Concentration Ozone-Water Using Freestanding Perforated Diamond Electrodes, *J. Electrochem. Soc.* 154 (2007) E71–E75. <https://doi.org/10.1149/1.2509385>.
- [70] S. Garcia-Segura, E. Mostafa, H. Baltruschat, Could NO_x be released during mineralization of pollutants containing nitrogen by hydroxyl radical? Ascertaining the release of N-volatile species, *Appl. Catal. B Environ.* 207 (2017) 376–384. <https://doi.org/10.1016/j.apcatb.2017.02.046>.
- [71] E. Mostafa, P. Reinsberg, S. Garcia-Segura, H. Baltruschat, Chlorine species evolution during electrochlorination on boron-doped diamond anodes: In-situ electrogeneration of Cl₂, Cl₂O and ClO₂, *Electrochim. Acta.* 281 (2018) 831–840. <https://doi.org/10.1016/j.electacta.2018.05.099>.
- [72] B. Marselli, J. Garcia-Gomez, P.-A. Michaud, M.A. Rodrigo, C. Comninellis, Electrogeneration of Hydroxyl Radicals on Boron-Doped Diamond Electrodes, *J. Electrochem. Soc.* 150 (2003) D79. <https://doi.org/10.1149/1.1553790>.
- [73] C. Comninellis, Electrocatalysis in the Electrochemical Conversion/Combustion of Organic Pollutants for Waste Water Treatment, *Electrochim. Acta.* 39 (1994) 1857–1862. [https://doi.org/10.1016/0013-4686\(94\)85175-1](https://doi.org/10.1016/0013-4686(94)85175-1).

- [74] P.A. Michaud, M. Panizza, L. Ouattara, T. Diaco, G. Foti, C. Comninellis, Electrochemical oxidation of water on synthetic boron-doped diamond thin film anodes, *J. Appl. Electrochem.* 33 (2003) 151–154. <https://doi.org/10.1023/A:1024084924058>.
- [75] P.A. Christensen, K. Zakaria, T.P. Curtis, Structure and Activity of Ni- and Sb-doped SnO₂/Ozone Anodes, *Ozone Sci. Eng.* 34 (2012) 49–56. <https://doi.org/10.1080/01919512.2012.639687>.
- [76] S.A. Cheng, K.Y. Chan, Electrolytic Generation of Ozone on an Antimony-Doped Tin Dioxide Coated Electrode, *Electrochem. Solid-State Lett.* 7 (2004) 34–36. <https://doi.org/10.1149/1.1645753>.
- [77] Y. Honda, T.A. Ivandini, T. Watanabe, K. Murata, Y. Einaga, An electrolyte-free system for ozone generation using heavily boron-doped diamond electrodes, *Diam. Relat. Mater.* 40 (2013) 7–11. <https://doi.org/10.1016/j.diamond.2013.09.001>.
- [78] Y. Park, D. Kim, J. Kim, H.J. Cho, H. Cho, J. Kim, T. Kim, Electrochemical Properties of Boron-Doped Diamond Thin Film Synthesized by MPCVD on Titanium Substrate to Use as an Ozone Generator, *ECS Trans.* 61 (2014) 87–97. <https://doi.org/10.1149/06107.0087ecst>.
- [79] M. Panizza, G. Cerisola, Application of diamond electrodes to electrochemical processes, *Electrochim. Acta.* 51 (2005) 191–199. <https://doi.org/10.1016/j.electacta.2005.04.023>.
- [80] Y. Tzeng, C.C. Tin, R. Phillips, T. Srivinyunon, Y. Chen, High electrical resistivity diamond films deposited from an oxyacetylene flame, *Appl. Phys. Lett.* 57 (1990) 789–791. <https://doi.org/10.1063/1.103421>.
- [81] Y.-H. Wang, S. Cheng, K.-Y. Chan, X.Y. Li, Electrolytic Generation of Ozone on Antimony- and Nickel-Doped Tin Oxide Electrode, *J. Electrochem. Soc.* 152 (2005) D197. <https://doi.org/10.1149/1.2041007>.
- [82] A.A. Babak, R. Amadelli, A. De Battisti, V.N. Fateev, Influence of Anions on Oxygen/Ozone Evolution on PbO₂/spe and PbO₂/Ti Electrodes in Neutral pH Media, *Electrochim. Acta.* 39 (1994) 1597–1602. [https://doi.org/10.1016/0013-4686\(94\)85141-7](https://doi.org/10.1016/0013-4686(94)85141-7).
- [83] A.B. Velichenko, D. V Girenko, F.I. Danilov, Mechanism of lead dioxide electrodeposition, *J. Electroanal. Chem.* 495 (1996) 127–132.
- [84] A.B. Velichenko, E.A. Baranova, D. V. Girenko, R. Amadelli, S. V. Kovalev, F.I. Danilov, Mechanism of Electrodeposition of Lead Dioxide from Nitrate Solutions, *Russ. J. Electrochem.* 39 (2003) 615–621. <https://doi.org/10.1023/A:1024101210790>.
- [85] X. Li, D. Pletcher, F.C. Walsh, Electrodeposited lead dioxide coatings, *Chem. Soc. Rev. Chem. Soc. Rev.* 40 (2011) 3879–3894. <https://doi.org/10.1039/c0cs00213e>.
- [86] K. Momma, F. Izumi, VESTA 3 for three-dimensional visualization of crystal, volumetric and morphology data, *J. Appl. Crystallogr.* 44 (2011) 1272–1276. <https://doi.org/10.1107/S0021889811038970>.
- [87] R.W.G. Wyckoff, *Crystal Structures*, Second edi, Interscience Publishers, New York, 1963.
- [88] A.A. Bolzan, C. Fong, B.J. Kennedy, C.J. Howard, Structural Studies of Rutile-Type Metal Dioxides, *Acta Crystallogr. Sect. B Struct. Sci.* 53 (1997) 373–380. <https://doi.org/10.1107/S0108768197001468>.
- [89] D. Rosestolato, R. Amadelli, A.B. Velichenko, Electrode characteristics for ozone production: a case study using undoped and doped PbO₂ on porous platinised titanium substrates, *J. Solid State Electrochem.* 20 (2016) 1181–1190. <https://doi.org/10.1007/s10008-015-2945-1>.
- [90] J.W. Yu, G. bin Jung, Y.J. Su, C.C. Yeh, M.Y. Kan, C.Y. Lee, C.J. Lai, Proton exchange membrane water electrolysis system-membrane electrode assembly with additive, *Int. J. Hydrogen Energy.* 44 (2019) 15721–15726. <https://doi.org/10.1016/j.ijhydene.2018.11.192>.
- [91] T.L. Doan, H.E. Lee, S.S.H. Shah, M.J. Kim, C.H. Kim, H.S. Cho, T. Kim, A review of the porous transport layer in polymer electrolyte membrane water electrolysis, *Int. J. Energy Res.* 45 (2021) 14207–14220. <https://doi.org/10.1002/er.6739>.
- [92] U. Babic, M. Suermann, F.N. Büchi, L. Gubler, T.J. Schmidt, Critical Review—Identifying Critical

- Gaps for Polymer Electrolyte Water Electrolysis Development, *J. Electrochem. Soc.* 164 (2017) F387–F399. <https://doi.org/10.1149/2.1441704jes>.
- [93] A. Kusoglu, A.Z. Weber, New Insights into Perfluorinated Sulfonic-Acid Ionomers, *Chem. Rev.* 117 (2017) 987–1104. <https://doi.org/10.1021/acs.chemrev.6b00159>.
- [94] K.A. Mauritz, R.B. Moore, State of understanding of Nafion, *Chem. Rev.* 104 (2004) 4535–4585. <https://doi.org/10.1021/cr0207123>.
- [95] H.G. Haubold, T. Vad, H. Jungbluth, P. Hiller, Nano structure of Nafion: A SAXS study, *Electrochim. Acta.* 46 (2001) 1559–1563. [https://doi.org/10.1016/S0013-4686\(00\)00753-2](https://doi.org/10.1016/S0013-4686(00)00753-2).
- [96] W.Y. Hsu, T.D. Gierke, Ion transport and clustering in nafion perfluorinated membranes, *J. Memb. Sci.* 13 (1983) 307–326. [https://doi.org/10.1016/S0376-7388\(00\)81563-X](https://doi.org/10.1016/S0376-7388(00)81563-X).
- [97] H. Ito, T. Maeda, A. Nakano, H. Takenaka, Properties of Nafion membranes under PEM water electrolysis conditions, *Int. J. Hydrogen Energy.* 36 (2011) 10527–10540. <https://doi.org/10.1016/j.ijhydene.2011.05.127>.
- [98] H. Takenaka, E. Torikai, Y. Kawami, N. Wakabayashi, Solid polymer electrolyte water electrolysis, *Int. J. Hydrogen Energy.* 7 (1982) 397–403. [https://doi.org/10.1016/0360-3199\(82\)90050-7](https://doi.org/10.1016/0360-3199(82)90050-7).
- [99] ISPE, Good Practice Guide: Ozone Sanitization of Pharma Water Systems, 2012.
- [100] V. Libman, D. Wilcox, B. Zerfas, Ultrapure Water for Advanced Semiconductor Manufacturing: Challenges and Opportunities V. Libman, *ECS Trans.* 69 (2015) 17–28. <https://doi.org/10.1149/06908.0017ecst>.
- [101] H. Lee, Y. Jin, S. Hong, Recent transitions in ultrapure water (UPW) technology: Rising role of reverse osmosis (RO), *Desalination.* 399 (2016) 185–197. <https://doi.org/10.1016/j.desal.2016.09.003>.
- [102] A.E.R. Budd, Ozone Control in High-Flying Jet Aircraft: Platinum Catalyst Ensures Decomposition, *Platin. Met. Rev.* 24 (1980) 90–94.
- [103] W.B. Demore, O.F. Raper, Primary processes in ozone photolysis, *J. Chem. Phys.* 44 (1966) 1780–1783. <https://doi.org/10.1063/1.1726939>.
- [104] Y. Matsumi, M. Kawasaki, Photolysis of Atmospheric Ozone in the Ultraviolet Region, *Chem. Rev.* 103 (2003) 4767–4781. <https://doi.org/10.1021/cr0205255>.
- [105] J. Workman, B. Lavine, R. Chrisman, M. Koch, Process analytical chemistry, *Anal. Chem.* 83 (2011) 4557–4578. <https://doi.org/10.1021/ac200974w>.
- [106] G. Schiavon, G. Zotti, G. Bontempelli, Amperometric Monitoring of Ozone in Gaseous Media by Gold Electrodes Supported on Ion Exchange Membranes (Solid Polymer Electrolytes), *Anal. Chem.* 62 (1990) 293–298.
- [107] J.H. Stanley, J.D. Johnson, Amperometric Membrane Electrode for Measurement of Ozone in Water, *Anal. Chem.* 51 (1979) 2144–2147. <https://doi.org/10.1021/ac50049a020>.
- [108] R. Knake, P.C. Hauser, Sensitive electrochemical detection of ozone, *Anal. Chim. Acta.* 459 (2002) 199–207. [https://doi.org/10.1016/S0003-2670\(02\)00121-6](https://doi.org/10.1016/S0003-2670(02)00121-6).
- [109] Y. Einaga, I. Tribidasarianggraningrum, Y. Ishii, S. Sekiguchi, K. Murata, Ozone water concentration measurement apparatus and ozone water concentration measurement method, US9,625,405 B2, 2017.
- [110] K. Vandersmissen, F. De Smedt, C. Vinckier, The impact of traces of hydrogen peroxide and phosphate on the ozone decomposition rate in “pure water,” *Ozone Sci. Eng.* 30 (2008) 300–309. <https://doi.org/10.1080/01919510802144085>.
- [111] H. Yoon, Current trends in sensors based on conducting polymer nanomaterials, *Nanomaterials.* 3 (2013) 524–549. <https://doi.org/10.3390/nano3030524>.
- [112] N.J. Ronkainen, H.B. Halsall, W.R. Heineman, Electrochemical biosensors, *Chem. Soc. Rev.* 39 (2010) 1747–1763. <https://doi.org/10.1039/b714449k>.

- [113] M.A. Arnold, M.E. Meyerhoff, Ion-Selective Electrodes, *Anal. Chem.* 56 (1984) 20–48.
- [114] S.M. de Smit, J.J.H. Langedijk, L.C.A. van Haalen, S.H. Lin, J.H. Bitter, D.P.B.T.B. Strik, Methodology for In Situ Microsensor Profiling of Hydrogen, pH, Oxidation-Reduction Potential, and Electric Potential throughout Three-Dimensional Porous Cathodes of (Bio)Electrochemical Systems, *Anal. Chem.* 95 (2023) 2680–2689. <https://doi.org/10.1021/acs.analchem.2c03121>.
- [115] G. Gordon, Gilbert E. Pacey, William J. Cooper, Rip G. Rice, Current State-Of-The-Art Measurements of Ozone In The Gas Phase And In Solution, *Ozone Sci. Eng.* 10 (1988) 353–365. <https://doi.org/10.1080/01919518808552390>.
- [116] J. Grunwell, J. Benga, H. Cohen, G. Gordon, A detailed comparison of analytical methods for residual ozone measurement, *Ozone Sci. Eng.* 5 (1983) 203–223. <https://doi.org/10.1080/01919518308550989>.
- [117] J. Nobbs, C. Tizaoui, A Modified Indigo Method for the Determination of Ozone in Nonaqueous Solvents, *Ozone Sci. Eng.* 36 (2014) 110–120. <https://doi.org/10.1080/01919512.2013.836956>.
- [118] H. Bader, J. Hoigné, Determination of ozone in water by the indigo method, *Water Res.* 15 (1981) 449–456. [https://doi.org/10.1016/0043-1354\(81\)90054-3](https://doi.org/10.1016/0043-1354(81)90054-3).
- [119] A.T. Palin, The Determination of Free and Combined Chlorine in Water by the Use of Diethyl- p -phenylene Diamine , *J. AWWA.* 49 (1957) 873–880. <https://doi.org/10.1002/j.1551-8833.1957.tb16870.x>.
- [120] A.T. Palin, Current DPD methods for residual halogen compounds and ozone in water, *J. / Am. Water Work. Assoc.* 67 (1975) 32–33. <https://doi.org/10.1002/j.1551-8833.1975.tb02149.x>.
- [121] J. Grunwell, J. Benga, H. Cohen, G. Gordon, A detailed comparison of analytical methods for residual ozone measurement, *Ozone Sci. Eng.* 5 (1983) 203–223. <https://doi.org/10.1080/01919518308550989>.
- [122] J.Q. Adams, B.J. Mariñas, Modified Indigo Method For Gaseous and Aqueous Ozone Analyses, *Ozone Sci. Eng.* 17 (1995) 329–344. <https://doi.org/10.1080/01919519508547539>.
- [123] T. Wang, D.A. Reckhow, Spectrophotometric Method for Determination of Ozone Residual in Water Using ABTS: 2,2'-Azino-Bis (3-Ethylbenzothiazoline-6-Sulfonate), *Ozone Sci. Eng.* 38 (2016) 373–381. <https://doi.org/10.1080/01919512.2016.1188681>.
- [124] DIN 38408-3:2011-04 Deutsche Einheitsverfahren zur Wasser-, Abwasser- und Schlammuntersuchung - Gasförmige Bestandteile (Gruppe G) - Teil 3: Bestimmung von Ozon (G 3), (2011).
- [125] M. Bourgin, E. Borowska, J. Helbing, J. Hollender, H.P. Kaiser, C. Kienle, C.S. Mc Ardell, E. Simon, U. von Gunten, Effect of operational and water quality parameters on conventional ozonation and the advanced oxidation process O₃/H₂O₂: Kinetics of micropollutant abatement, transformation product and bromate formation in a surface water, *Water Res.* 122 (2017) 234–245. <https://doi.org/10.1016/j.watres.2017.05.018>.
- [126] D.B. Miklos, C. Remy, M. Jekel, K.G. Linden, J.E. Drewes, U. Hübner, Evaluation of advanced oxidation processes for water and wastewater treatment – A critical review, *Water Res.* 139 (2018) 118–131. <https://doi.org/10.1016/j.watres.2018.03.042>.
- [127] Á. Moratalla, S.E. Correia, E. Lacasa, P. Murillo, P. Cañizares, M.A. Rodrigo, C. Sáez, Facing the treatment of polymedicated effluents using gaseous ozone electrochemically generated, *J. Water Process Eng.* 55 (2023). <https://doi.org/10.1016/j.jwpe.2023.104153>.
- [128] W. Ding, S. Cao, W. Jin, X. Zhou, C. Wang, Q. Jiang, H. Huang, R. Tu, S.-F. Han, Q. Wang, Ozone disinfection of chlorine-resistant bacteria in drinking water, *Water Res.* 160 (2019) 339–349. <https://doi.org/10.1016/j.watres.2019.05.014>.
- [129] Z. Zhang, G. Yi, P. Li, X. Wang, X. Wang, C. Zhang, Y. Zhang, Recent progress in engineering approach towards the design of PbO₂-based electrodes for the anodic oxidation of organic pollutants, *J. Water Process Eng.* 42 (2021) 102173. <https://doi.org/10.1016/j.jwpe.2021.102173>.
- [130] M. Paidar, V. Fateev, K. Bouzek, Membrane electrolysis—History, current status and perspective, *Electrochim. Acta.* 209 (2016) 737–756.

<https://doi.org/10.1016/j.electacta.2016.05.209>.

- [131] F. Okada, K. Naya, Electrolysis for Ozone Water Production, in: *Electrolysis*, InechOpen, Rijeka, 2012. <https://doi.org/10.5772/51945>.
- [132] R. Grimmig, P. Gillemot, S. Lindner, P. Schmidt, S. Stucki, K. Günther, H. Baltruschat, S. Witzleben, Evaluating Platinum-Based Ionic Polymer Metal Composites as Potentiometric Sensors for Dissolved Ozone in Ultrapure Water Systems, *Adv. Mater. Technol.* 2202043 (2023) 1–13. <https://doi.org/10.1002/admt.202202043>.
- [133] K. Sehested, H. Corfitzen, J. Holcman, E.J. Hart, On the mechanism of the decomposition of acidic O₃ solutions, thermally or H₂O₂-initiated, *J. Phys. Chem. A.* 102 (1998) 2667–2672. <https://doi.org/10.1021/jp9721053>.
- [134] J. Staehelin, J. Hoigne, Decomposition of ozone in water in the presence of organic solutes acting as promoters and inhibitors of radical chain reactions, *Environ. Sci. Technol.* 19 (1985) 1206–1213. <https://doi.org/10.1021/es00142a012>.
- [135] A. Stefanova, S. Ayata, A. Erem, S. Ernst, H. Baltruschat, Mechanistic studies on boron-doped diamond: Oxidation of small organic molecules, *Electrochim. Acta.* 110 (2013) 560–569. <https://doi.org/10.1016/j.electacta.2013.05.104>.
- [136] C.J. Bondue, P. Königshoven, H. Baltruschat, A New 2-Compartment Flow Through Cell for the Simultaneous Detection of Electrochemical Reaction Products by a Detection Electrode and Mass Spectroscopy, *Electrochim. Acta.* 214 (2016) 241–252. <https://doi.org/10.1016/j.electacta.2016.08.008>.
- [137] S. Garcia-Segura, E. Mostafa, H. Baltruschat, Electrogenation of inorganic chloramines on boron-doped diamond anodes during electrochemical oxidation of ammonium chloride, urea and synthetic urine matrix, *Water Res.* 160 (2019) 107–117. <https://doi.org/10.1016/j.watres.2019.05.046>.
- [138] E. Reisz, C. von Sonntag, A. Tekle-Röttering, S. Naumov, W. Schmidt, T.C. Schmidt, Reaction of 2-propanol with ozone in aqueous media, *Water Res.* 128 (2018) 171–182. <https://doi.org/10.1016/j.watres.2017.10.035>.
- [139] J.J. Wu, J.S. Yang, M. Muruganandham, C.C. Wu, The oxidation study of 2-propanol using ozone-based advanced oxidation processes, *Sep. Purif. Technol.* 62 (2008) 39–46. <https://doi.org/10.1016/j.seppur.2007.12.018>.
- [140] S.H. Schäfer, K. van Dyk, J. Warmer, T.C. Schmidt, P. Kaul, A New Setup for the Measurement of Total Organic Carbon in Ultrapure Water Systems, *Sensors.* 22 (2022). <https://doi.org/10.3390/s22052004>.
- [141] A. Giwa, A. Yusuf, H. Abiodun, N. Soraya, M. Roil, I. Adeyemi, S. Chakraborty, S. Curcio, Recent advances in advanced oxidation processes for removal of contaminants from water: A comprehensive review, *Process Saf. Environ. Prot.* 146 (2021) 220–256. <https://doi.org/10.1016/j.psep.2020.08.015>.
- [142] U. Feistel, P. Otter, S. Kunz, T. Grischek, J. Feller, Field tests of a small pilot plant for the removal of arsenic in groundwater using coagulation and filtering, *J. Water Process Eng.* 14 (2016) 77–85. <https://doi.org/10.1016/j.jwpe.2016.10.006>.
- [143] P. Kruse, Review on water quality sensors, *J. Phys. D. Appl. Phys.* 51 (2018) 203002. <https://doi.org/10.1088/1361-6463/aabb93>.
- [144] E.S. Massima Mouele, O.O. Fatoba, O. Babajide, K.O. Badmus, L.F. Petrik, Review of the methods for determination of reactive oxygen species and suggestion for their application in advanced oxidation induced by dielectric barrier discharges, *Environ. Sci. Pollut. Res.* 25 (2018) 9265–9282. <https://doi.org/10.1007/s11356-018-1392-9>.
- [145] P. Fernández-Castro, M. Vallejo, M.F. San Román, I. Ortiz, Insight on the fundamentals of advanced oxidation processes: Role and review of the determination methods of reactive oxygen species, *J. Chem. Technol. Biotechnol.* 90 (2015) 796–820. <https://doi.org/10.1002/jctb.4634>.
- [146] W.R. Penrose, L. Pan, J.R. Stetter, W.M. Ollison, Sensitive measurement of ozone using

- amperometric gas sensors, *Anal. Chim. Acta.* 313 (1995) 209–219. [https://doi.org/10.1016/0003-2670\(95\)00251-T](https://doi.org/10.1016/0003-2670(95)00251-T).
- [147] P. Zhu, R. Wu, X. Liu, Z. Yang, P. Xu, B. Hou, Rapid measurement of trace periodate concentration with bromide ion–catalyzed periodate for oxidation colorization of DPD, *J. Water Process Eng.* 58 (2024) 104825. <https://doi.org/10.1016/j.jwpe.2024.104825>.
- [148] J. Zou, H. Cai, D. Wang, J. Xiao, Z. Zhou, B. Yuan, Spectrophotometric determination of trace hydrogen peroxide via the oxidative coloration of DPD using a Fenton system, *Chemosphere.* 224 (2019) 646–652. <https://doi.org/10.1016/j.chemosphere.2019.03.005>.
- [149] G. Louit, S. Foley, J. Cabillic, H. Coffigny, F. Taran, A. Valleix, J.P. Renault, S. Pin, The reaction of coumarin with the OH radical revisited: Hydroxylation product analysis determined by fluorescence and chromatography, *Radiat. Phys. Chem.* 72 (2005) 119–124. <https://doi.org/10.1016/j.radphyschem.2004.09.007>.
- [150] M.D.G. de Luna, J.I. Colades, C.C. Su, M.C. Lu, Comparison of dimethyl sulfoxide degradation by different Fenton processes, *Chem. Eng. J.* 232 (2013) 418–424. <https://doi.org/10.1016/j.cej.2013.07.107>.
- [151] R.S. Lankone, A.R. Deline, M. Barclay, D.H. Fairbrother, UV–Vis quantification of hydroxyl radical concentration and dose using principal component analysis, *Talanta.* 218 (2020) 121148. <https://doi.org/10.1016/j.talanta.2020.121148>.
- [152] T. Deng, S. Hu, X. an Huang, J. Song, Q. Xu, Y. Wang, F. Liu, A novel strategy for colorimetric detection of hydroxyl radicals based on a modified Griess test, *Talanta.* 195 (2019) 152–157. <https://doi.org/10.1016/j.talanta.2018.11.044>.
- [153] Z. Li, S. Yuan, C. Qiu, Y. Wang, X. Pan, J. Wang, C. Wang, J. Zuo, Electrochimica Acta Effective degradation of refractory organic pollutants in landfill leachate by electro-peroxone treatment, *Electrochim. Acta.* 102 (2013) 174–182. <https://doi.org/10.1016/j.electacta.2013.04.034>.
- [154] X. Sui, X. Duan, F. Xu, L. Chang, Journal of the Taiwan Institute of Chemical Engineers Fabrication of three-dimensional networked PbO₂ anode for electrochemical oxidation of organic pollutants in aqueous solution, *J. Taiwan Inst. Chem. Eng.* 100 (2019) 74–84. <https://doi.org/10.1016/j.jtice.2019.04.007>.
- [155] Y. Arbid, M. Usman, N.T. Luong, B. Mathon, B. Cedat, J.-F. Boily, K. Hanna, Use of iron-bearing waste materials in laundry wastewater treatment, *J. Water Process Eng.* 57 (2024) 104717. <https://doi.org/10.1016/j.jwpe.2023.104717>.
- [156] S. Pei, S. You, J. Ma, X. Chen, N. Ren, Electron Spin Resonance Evidence for Electro-generated Hydroxyl Radicals, *Environ. Sci. Technol.* 54 (2020) 13333–13343. <https://doi.org/10.1021/acs.est.0c05287>.
- [157] E. Kurowska, A. Brzózka, M. Jarosz, G.D. Sulka, M. Jaskuła, Silver nanowire array sensor for sensitive and rapid detection of H₂O₂, *Electrochim. Acta.* 104 (2013) 439–447. <https://doi.org/10.1016/j.electacta.2013.01.077>.
- [158] L. Domínguez-Henao, A. Turolla, D. Monticelli, M. Antonelli, Assessment of a colorimetric method for the measurement of low concentrations of peracetic acid and hydrogen peroxide in water, *Talanta.* 183 (2018) 209–215. <https://doi.org/10.1016/j.talanta.2018.02.078>.
- [159] J.L. Aquino de Queiroz, C.A. Martínez-Huitle, P.S. Castro, Real time monitoring of in situ generated hydrogen peroxide in electrochemical advanced oxidation reactors using an integrated Pt microelectrode, *Talanta.* 218 (2020) 121133. <https://doi.org/10.1016/j.talanta.2020.121133>.
- [160] G.M. Eisenberg, Colorimetric Determination of Hydrogen Peroxide, *Ind. Eng. Chem. - Anal. Ed.* 15 (1943) 327–328. <https://doi.org/10.1021/i560117a011>.
- [161] G.A. Zoumpouli, M. Scheurer, H.J. Brauch, B. Kasprzyk-Hordern, J. Wenk, O. Happel, COMBI, continuous ozonation merged with biofiltration to study oxidative and microbial transformation of trace organic contaminants, *Environ. Sci. Water Res. Technol.* 5 (2019) 552–563. <https://doi.org/10.1039/c8ew00855h>.

- [162] N. Hermes, G. Knupp, Transformation of atrazine, bisphenol A and chlrendic acid by electrochemically produced oxidants using a lead dioxide electrode, *Environ. Sci. Water Res. Technol.* 1 (2015) 905–912. <https://doi.org/10.1039/c5ew00149h>.
- [163] J. Hoigné, Inter-calibration of OH radical sources and water quality parameters, *Water Sci. Technol.* 35 (1997) 1–8. [https://doi.org/10.1016/S0273-1223\(97\)00002-4](https://doi.org/10.1016/S0273-1223(97)00002-4).
- [164] DIN 38409-15:1987-06 Deutsche Einheitsverfahren zur Wasser-, Abwasser- und Schlammuntersuchung; Summarische Wirkungs- und Stoffkenngrößen (Gruppe H); Bestimmung von Wasserstoffperoxid (Hydrogenperoxid) und seinen Addukten (H 15), (1987).
- [165] J.P. Crow, C. Spruell, J. Chen, C. Gunn, H. Ischiropoulos, M. Tsai, C.D. Smith, R. Radi, W.H. Koppenol, J.S. Beckman, On the pH-dependent yield of hydroxyl radical products from peroxynitrite, *Free Radic. Biol. Med.* 16 (1994) 331–338. [https://doi.org/10.1016/0891-5849\(94\)90034-5](https://doi.org/10.1016/0891-5849(94)90034-5).
- [166] H. Shiraishi, M. Kataoka, Y. Morita, J. Umemoto, Interactions of Hydroxyl Radicals with Tris (Hydroxymethyl) Aminomethane and Good's Buffers Containing Hydroxymethyl or Hydroxyethyl Residues Produce Formaldehyde, *Free Radic. Res. Commun.* 19 (1993) 315–321. <https://doi.org/10.3109/10715769309056520>.
- [167] V.M. Mishin, P.E. Thomas, Characterization of hydroxyl radical formation by microsomal enzymes using a water-soluble trap, terephthalate, *Biochem. Pharmacol.* 68 (2004) 747–752. <https://doi.org/10.1016/j.bcp.2004.05.004>.
- [168] M.A. Rosenfeld, S.D. Razumovskii, A.N. Shchegolikhin, M.L. Konstantinova, N.B. Sultimova, A.I. Kozachenko, L.G. Nagler, A. V. Bychkova, V.B. Leonova, Nature of active intermediate particles formed during ozone-induced oxidation, *Dokl. Biochem. Biophys.* 461 (2015) 139–141. <https://doi.org/10.1134/S1607672915020180>.
- [169] J. Steidtner, F. Hernandez, H. Baltruschat, Electrocatalytic reactivity of Pd monolayers and monatomic chains on Au, *J. Phys. Chem. C.* 111 (2007) 12320–12327. <https://doi.org/10.1021/jp071712f>.
- [170] C. von Sonntag, U. von Gunten, Chemistry of Ozone in Water and Wastewater Treatment: From Basic Principles to Applications, IWA Publishing, London, 2012. <https://doi.org/10.2166/9781780400839>.
- [171] Y. Jing, B.P. Chaplin, Mechanistic Study of the Validity of Using Hydroxyl Radical Probes to Characterize Electrochemical Advanced Oxidation Processes, *Environ. Sci. Technol.* 51 (2017) 2355–2365. <https://doi.org/10.1021/acs.est.6b05513>.
- [172] M. Panizza, G. Cerisola, Electrocatalytic materials for the electrochemical oxidation of synthetic dyes, *Appl. Catal. B Environ.* 75 (2007) 95–101. <https://doi.org/10.1016/j.apcatb.2007.04.001>.
- [173] S. Lim, J.L. Shi, U. von Gunten, D.L. McCurry, Ozonation of organic compounds in water and wastewater: A critical review, *Water Res.* 213 (2022) 118053. <https://doi.org/10.1016/j.watres.2022.118053>.
- [174] G. V. Buxton, C.L. Greenstock, W.P. Helman, A.B. Ross, Critical Review of rate constants for reactions of hydrated electrons, hydrogen atoms and hydroxyl radicals ($\cdot\text{OH}/\text{O}^-$ in Aqueous Solution, *J. Phys. Chem. Ref. Data.* 17 (1988) 513–886. <https://doi.org/10.1063/1.555805>.
- [175] I. Kisacik, A. Stefanova, S. Ernst, H. Baltruschat, Oxidation of carbon monoxide, hydrogen peroxide and water at a boron doped diamond electrode: The competition for hydroxyl radicals, *Phys. Chem. Chem. Phys.* 15 (2013) 4616–4624. <https://doi.org/10.1039/c3cp44643c>.
- [176] C.M. Pham, N.Q. Pham, A.K. Le, Oxidation-Reduction Potential and Peroxone Process in Antibiotic Residues Removal from Hospital Wastewater, *Chem. Eng. Trans.* 97 (2022) 187–192. <https://doi.org/10.3303/CET2297032>.
- [177] T.W. LeBaron, R. Sharpe, ORP should not be used to estimate or compare concentrations of aqueous H_2 : An in silico analysis and narrative synopsis, *Front. Food Sci. Technol.* 2 (2022) 1–17. <https://doi.org/10.3389/frfst.2022.1007001>.
- [178] C. Kim, Y.C. Hung, R.E. Brackett, Roles of oxidation-reduction potential in electrolyzed oxidizing

- and chemically modified water for the inactivation of food-related pathogens, *J. Food Prot.* 63 (2000) 19–24. <https://doi.org/10.4315/0362-028X-63.1.19>.
- [179] S. Okouchi, M. Suzuki, K. Sugano, S. Kagamimori, S. Ikeda, Water desirable for the human body in terms of oxidation-reduction potential (ORP) to pH relationship, *J. Food Sci.* 67 (2002) 1594–1598. <https://doi.org/10.1111/j.1365-2621.2002.tb08689.x>.
- [180] M. Sakthivel, W. Weppner, Response behaviour of a hydrogen sensor based on ionic conducting polymer-metal interfaces prepared by the chemical reduction method, *Sensors.* 6 (2006) 284–297. <https://doi.org/10.3390/s6040284>.
- [181] L. Xie, J. Lu, H. Yan, A Solid-State Ozone Sensor Based on Solid Polymer Electrolyte, *Electroanalysis.* 10 (1998) 842–845. [https://doi.org/10.1002/\(SICI\)1521-4109\(199809\)10:12<842::AID-ELAN842>3.0.CO;2-S](https://doi.org/10.1002/(SICI)1521-4109(199809)10:12<842::AID-ELAN842>3.0.CO;2-S).
- [182] R. Liu, In Situ Electrode Formation on a Nafion Membrane by Chemical Platinization, *J. Electrochem. Soc.* 139 (1992) 15. <https://doi.org/10.1149/1.2069162>.
- [183] P.S. Fedkiw, An Impregnation-Reduction Method to Prepare Electrodes on Nafion SPE, *J. Electrochem. Soc.* 136 (1989) 899. <https://doi.org/10.1149/1.2096772>.
- [184] J. Zhao, C. Huang, S. Zhang, F. Qu, R. Wang, H. Jiang, M. Yang, Excellent stability fuel cell type methanol sensor based on platinum-decorated mesoporous CrN, *Sensors Actuators, B Chem.* 341 (2021) 129993. <https://doi.org/10.1016/j.snb.2021.129993>.
- [185] A. Sode, N.J.C. Ingle, M. McCormick, D. Bizzotto, E. Gyenge, S. Ye, S. Knights, D.P. Wilkinson, Controlling the deposition of Pt nanoparticles within the surface region of Nafion, *J. Memb. Sci.* 376 (2011) 162–169. <https://doi.org/10.1016/j.memsci.2011.04.016>.
- [186] L. Daniel, A. Bonakdarpour, D.P. Wilkinson, Relationship between Electroless Pt Nanoparticle Growth and Interconnectivity at the Membrane Interface: Implications for Fuel Cell Applications, *ACS Appl. Nano Mater.* 2 (2019) 3127–3137. <https://doi.org/10.1021/acsanm.9b00461>.
- [187] N.J.C. Ingle, A. Sode, I. Martens, E. Gyenge, D.P. Wilkinson, D. Bizzotto, Synthesis and characterization of diverse Pt nanostructures in nafion, *Langmuir.* 30 (2014) 1871–1879. <https://doi.org/10.1021/la403399y>.
- [188] P. Millet, M. Pineri, R. Durand, New solid polymer electrolyte composites for water electrolysis, *J. Appl. Electrochem.* 19 (1989) 162–166. <https://doi.org/10.1007/BF01062295>.
- [189] L. Daniel, A. Bonakdarpour, D.P. Wilkinson, Benefits of platinum deposited in the polymer membrane subsurface on the operational flexibility of hydrogen fuel cells, *J. Power Sources.* 471 (2020) 228418. <https://doi.org/10.1016/j.jpowsour.2020.228418>.
- [190] P.C. Lee, J.E. Hyun, S.K. Jeoung, J. Do Nam, T. Hwang, K.J. Kim, K.C. Solasa, Ionic polymer metal composites for use as an organic electrolyte supercapacitor, *Smart Mater. Struct.* 28 (2019). <https://doi.org/10.1088/1361-665X/ab1182>.
- [191] Z. Zhu, X. Liu, Z. Ye, J. Zhang, F. Cao, J. Zhang, A fabrication of iridium oxide film pH micro-sensor on Pt ultramicroelectrode and its application on in-situ pH distribution of 316L stainless steel corrosion at open circuit potential, *Sensors Actuators, B Chem.* 255 (2018) 1974–1982. <https://doi.org/10.1016/j.snb.2017.08.219>.
- [192] M. Wang, S. Yao, M. Madou, A long-term stable iridium oxide pH electrode, *Sensors Actuators, B Chem.* 81 (2002) 313–315. [https://doi.org/10.1016/S0925-4005\(01\)00972-8](https://doi.org/10.1016/S0925-4005(01)00972-8).
- [193] O.C. Keller, J. Buffle, Voltammetric and reference microelectrodes with integrated microchannels for flow through microvoltammetry. 1. The microcell, *Anal. Chem.* 72 (2000) 936–942. <https://doi.org/10.1021/ac9905064>.
- [194] K.P. Burnham, D.R. Anderson, Kullback-Leibler information as a basis for strong inference in ecological studies, *Wildl. Res.* 28 (2001) 111–119. <https://doi.org/10.1071/WR99107>.
- [195] E.J. Wagenmakers, S. Farrell, AIC model selection using Akaike weights, *Psychon. Bull. Rev.* 11 (2004) 192–196. <https://doi.org/10.3758/BF03206482>.
- [196] I. Langmuir, The constitution and fundamental properties of solids and liquids. Part II.-Liquids, *J.*

- Franklin Inst. 184 (1917) 721. [https://doi.org/10.1016/s0016-0032\(17\)90088-2](https://doi.org/10.1016/s0016-0032(17)90088-2).
- [197] G.E.P. Box, R.D. Meyer, An Analysis for Unreplicated Fractional Factorials, *Technometrics*. 28 (1986) 11–18.
- [198] M. Rodríguez-Peña, J.A. Barrios Pérez, J. Lobato, C. Saez, C.E. Barrera-Díaz, M.A. Rodrigo, Scale-up in PEM electro-ozonizers for the degradation of organics, *Sep. Purif. Technol.* 284 (2021) 120261. <https://doi.org/10.1016/j.seppur.2021.120261>.
- [199] D. Haaken, T. Dittmar, V. Schmalz, E. Worch, Disinfection of biologically treated wastewater and prevention of biofouling by UV/electrolysis hybrid technology: Influence factors and limits for domestic wastewater reuse, *Water Res.* 52 (2014) 20–28. <https://doi.org/10.1016/j.watres.2013.12.029>.
- [200] N. Hermes, G. Knupp, Transformation of atrazine, bisphenol A and chlorendic acid by electrochemically produced oxidants using a lead dioxide electrode, *Environ. Sci. Water Res. Technol.* 1 (2015) 905–912. <https://doi.org/10.1039/c5ew00149h>.
- [201] J. Hu, H. Zhang, W. Xu, Z. Yuan, X. Li, Mechanism and transfer behavior of ions in Nafion membranes under alkaline media, *J. Memb. Sci.* 566 (2018) 8–14. <https://doi.org/10.1016/j.memsci.2018.08.057>.
- [202] R.A. Rozendal, H.V.M. Hamelers, C.J.N. Buisman, Effects of membrane cation transport on pH and microbial fuel cell performance, *Environ. Sci. Technol.* 40 (2006) 5206–5211. <https://doi.org/10.1021/es060387r>.
- [203] J.S. Lawton, A. Jones, T. Zawodzinski, Concentration dependence of VO₂⁺ crossover of nafion for vanadium redox flow batteries, *J. Electrochem. Soc.* 160 (2013) 697–702. <https://doi.org/10.1149/2.004306jes>.
- [204] C. Lutz, S. Hampel, X. Ke, S. Beuermann, T. Turek, U. Kunz, A. Guilherme Buzanich, M. Radtke, U.E.A. Fittschen, Evidence for redox reactions during vanadium crossover inside the nanoscopic water-body of Nafion 117 using X-ray absorption near edge structure spectroscopy, *J. Power Sources*. 483 (2021). <https://doi.org/10.1016/j.jpowsour.2020.229176>.
- [205] T. Chen, A. Neville, M. Yuan, Influence of Mg²⁺ on CaCO₃ formation-bulk precipitation and surface deposition, *Chem. Eng. Sci.* 61 (2006) 5318–5327. <https://doi.org/10.1016/j.ces.2006.04.007>.
- [206] D. Schulze, S. Stucki, R. Grimmig, [DE] Elektrolysezelle, Verfahren zum Betreiben einer Elektrolysezelle und Verwendung einer Elektrolysezelle, 2021.
- [207] Gesetz über die Umweltverträglichkeit von Wasch- und Reinigungsmitteln (WRMG), 2017.

Annex

Paper: Evaluating Platinum-Based Ionic Polymer Metal Composites as Potentiometric Sensors for Dissolved Ozone in Ultrapure Water Systems

Roman Grimmig, Philipp Gillemot, Axel Kretschmer, Klaus Günther,
Helmut Baltruschat, Steffen Witzleben

published in

Advanced Materials Technologies, Volume 8, Issue 12, 2202043, 2023

DOI: 10.1002/admt.202202043

Evaluating Platinum-Based Ionic Polymer Metal Composites as Potentiometric Sensors for Dissolved Ozone in Ultrapure Water Systems

Roman Grimmig,* Philipp Gillemot, Simon Lindner, Philipp Schmidt, Samuel Stucki, Klaus Günther, Helmut Baltruschat, and Steffen Witzleben

Monitoring the content of dissolved ozone in purified water is often mandatory to ensure the appropriate levels of disinfection and sanitization. However, quantification bears challenges as colorimetric assays require laborious off-line analysis, while commercially available instruments for electrochemical process analysis are expensive and often lack the possibility for miniaturization and discretionary installation. In this study, potentiometric ionic polymer metal composite (IPMC) sensors for the determination of dissolved ozone in ultrapure water (UPW) systems are presented. Commercially available polymer electrolyte membranes are treated via an impregnation-reduction method to obtain nanostructured platinum layers. By applying 25 different synthesis conditions, layer thicknesses of 2.2 to 12.6 μm are obtained. Supporting radiographic analyses indicate that the platinum concentration of the impregnation solution has the highest influence on the obtained metal loading. The sensor response behavior is explained by a Langmuir pseudo-isotherm model and allows the quantification of dissolved ozone to trace levels of less than 10 $\mu\text{g L}^{-1}$. Additional statistical evaluations show that the expected Pt loading and radiographic blackening levels can be predicted with high accuracy and significance ($R^2_{\text{adj.}} > 0.90$, $p < 10^{-10}$) solely from given synthesis conditions.

1. Introduction

In the pharmaceutical and semiconductor industry, the use of sanitized ultrapure water is mandatory for the production and


preparation of medical products and microprocessors.^[1–3] In order to obtain and store water of different quality standards (e.g. *aqua purificata*, water for injection), various disinfection strategies are in use.^[4–6] Concerning the production and energy-efficient cold storage of sanitized, pressurized water, electrochemically produced ozone (O_3) is the disinfectant of choice.^[7,8]

Although the stored water is allowed to contain minimal amounts of dissolved ozone ensuring sterility,^[9] the process water should be clear of any oxidizing agents.^[2] Consequently, a reliable method to monitor the concentration of dissolved ozone in water is required. However, common reference methods have shown to be rather inconvenient as they are based on sampling and off-line analysis, typically including a wet chemical processing step followed by a spectroscopic^[10–12] or titrimetric^[13,14] determination. Thus, an on-line method with an

electrochemical sensor suitable for aqueous application is desired in order to obtain quick and continuous readings.

Within the past 40 years, different amperometric^[15,16] and voltammetric^[17–19] sensor systems have become the industry

R. Grimmig, P. Gillemot, P. Schmidt, S. Witzleben
Bonn-Rhein-Sieg University of Applied Sciences Department of Natural Sciences
von-Liebig-Str. 20, 53359 Rheinbach, Germany
E-mail: roman.grimmig@h-brs.de

 The ORCID identification number(s) for the author(s) of this article can be found under <https://doi.org/10.1002/admt.202202043>

© 2023 The Authors. Advanced Materials Technologies published by Wiley-VCH GmbH. This is an open access article under the terms of the Creative Commons Attribution License, which permits use, distribution and reproduction in any medium, provided the original work is properly cited.

DOI: 10.1002/admt.202202043

S. Lindner
Research Centre for Experimental Marine Biology and Biotechnology
Plentzia Marine Station
PiE-UPV/EHU
University of the Basque Country
Plentzia 48620, Spain
S. Stucki
Innovatec Gerätetechnik GmbH
von-Liebig-Str. 6, 53359 Rheinbach, Germany
K. Günther
Institute for Bio- and Geosciences (IBG-2)
Research Centre Jülich
Wilhelm-Johnen-Straße, 52428 Jülich, Germany
H. Baltruschat
Clausius Institute of Physical and Theoretical Chemistry
University of Bonn
Römerstr. 164, 53117 Bonn, Germany

standard, leading to commonly used commercial ozone sensors, for example, from the Orbisphere product family as used in previous studies.^[9,20] However, miniaturization and the suitability for adaption into an embedded system are limited and add to the setup cost, which is why these devices are often only installed at one spot within water storage systems.

When it comes to compact setups, a widely used type of sensor material is based on polymer electrolyte membranes (PEM) containing catalytic layers of defined metal loading. The required noble metal surface can be obtained using different approaches,^[21,22] including the impregnation-reduction technique.^[23–25] Therein, Nafion acts as a solid ion exchanger and allows the exchange with metal cations, which are subsequently reduced to their metallic state. Depending on the noble metals and reductants used, the resulting ionic polymer metal composite (IPMC) can be tailored to its specific application.^[26,27] Most commonly, these materials find their field of application in the detection of hydrogen peroxide,^[28] dissolved and gaseous hydrogen^[29–32] as well as gaseous ozone.^[15,33–35] However, for the detection of dissolved oxygen species in aqueous media, only a few sensor systems are reported.^[36–38]

The influence of preparation parameters of such IPMCs has previously been discussed by Sakthivel et al.,^[31] however, this has only been investigated in the context of hydrogen sensors. Furthermore, by determining the surface characteristics of Pt electrodes, correlations between the particle size and the amperometric sensor response were identified. Furthermore, it has been reported that incorporating nanoparticles in the IPMC structure influences the properties of a material in the application as a potentiometric sensor.^[39] As the use of a supporting solution during the impregnation-reduction process has been reported, Pt layer formation might be altered by influencing the establishing equilibria within the ion exchange membrane from both sides.^[40] Thus, a deeper knowledge of the structural composition is equally desired for the development of highly sensitive potentiometric ozone sensors.

The determination of the metal loading is described in varying quality within the literature, as often enough a thorough, comprehensible analytical procedure is not provided. For IPMC specimens with large dimensions, the loading is commonly determined gravimetrically,^[24,41] while for low absolute metal content a digestion in aqua regia followed by ICP OES analysis is favored.^[42–44] In addition, the application of image processing after TEM analysis has been successfully evaluated.^[40]

This study covers the preparation of platinum-based IPMC sensor materials for the application as potentiometric sensors, suitable for the quantification of aqueous ozone in ultrapure water (UPW). By systematic variation of critical synthesis parameters during the impregnation-reduction process, different sensor materials with varying appearances are obtained. The prepared surfaces are thoroughly characterized regarding their physicochemical properties and evaluated in terms of their ozone-sensing characteristics. From the collected data, structure-property relationships are identified and provide guidelines for the preparation of compact, tailor-made sensors using suitable synthesis conditions.

Table 1. Analytical parameters for regression functions of both Pt content as well as dissolved ozone. For each analytical method, the upper limit of quantification (ULOQ), limits of detection (LOD), and quantification (LOQ) as well as the coefficient of determination (R^2) are given and show satisfactory values. Additionally, the method precision is given as the coefficient of variation of the procedure (V_{x0}).

Method	Pt	O ₃	
	ICP OES radial configuration	DPD method via VIS spectroscopy with 5 cm cuvette	DPD method via VIS spectroscopy with 1 cm cuvette
λ / nm	370.6	510.0	510.0
ULOQ [mg L ⁻¹]	20.0	0.12	2.4
LOD [μ g L ⁻¹]	51.3	0.9	43.1
LOQ [μ g L ⁻¹]	213.0	3.2	130.5
R^2	0.9997	0.9998	0.9994
V_{x0} [%]	2.1	1.5	2.1

2. Results and Discussion

2.1. Analytical Performance of Spectroscopic Determination Methods

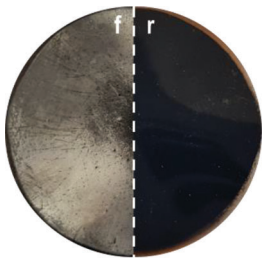
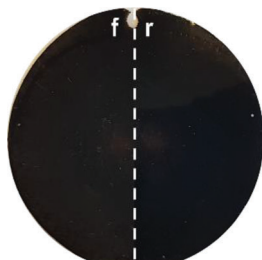
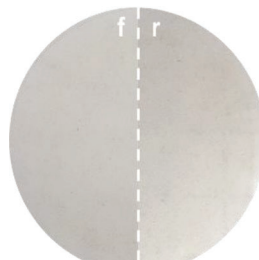
For a thorough characterization of the sensor material, the ability to accurately determine the quantity of Pt deposited per membrane surface area and the concentration of O₃ in UPW is central to this study. This is especially true for the quantification of the metal loading as gravimetric determination approaches suffer from poor sensitivity due to the low absolute weight of the noble metal incorporated within the IPMC.

Hence, a more selective and precise spectroscopic determination was chosen for this study. To ensure an exhaustive removal of the metal layer from the IPMC electrode after digestion with aqua regia, the absence of Pt signals from the residual Nafion substrate was confirmed via X-ray fluorescence.

The performed calibrations were described regarding their analytical capabilities, which are given in Table 1. LOD and LOQ values were calculated using a calibration approach according to DIN ISO 11843-2:2006-06 and DIN 32645:2008-11.

A wide calibration range from 20.0 mg L⁻¹ down to just 213 μ g L⁻¹ Pt content allows for the analysis of digested samples that originate from both heavily loaded electrode surfaces as well as barely coated IPMC materials. For ozone concentrations, a range from 2.4 mg L⁻¹ down to 0.9 μ g L⁻¹ is suitable to reliably detect traces of dissolved ozone emerging after short periods of electrolysis operation or operational conditions involving low current densities. It must be noted that these analytical limitations can only be reached when the highest grade UPW (18.2 M Ω cm resistivity, total organic carbon \leq 1 μ g L⁻¹) is used, as the presence of natural organic matter or other reactive oxygen species may bear additional challenges. The calibration curves for all analytical procedures were fitted to linear functions with coefficients of determination $R^2 > 0.999$ and coefficients of variation less than 2.1 %, stressing the precision and suitability of the chosen methods.

Table 2. Visual appearance of a representative selection of IPMC sensor materials and their specific synthesis conditions (top view, photomontage). The electrode surface exposed to the impregnation-reduction process (front side, marked “f”, pointing upwards during the synthesis) is shown on the left half of the picture, whereas the right half of the picture refers to the rear of the electrode surface which was exposed to the supporting solution (marked “r”, pointing downwards).

Specimen	#10	#7	#25
IPMC appearance			
Reducing agent	KBH_4	KBH_4	N_2H_4
Reductant concentration	40 mmol L^{-1}	200 mmol L^{-1}	$25\,000 \text{ mmol L}^{-1}$ ($\omega = 80\%$)
Reduction strategy	$3 \times 20 \text{ min}$	$1 \times 60 \text{ min}$	$1 \times 60 \text{ min}$
Pt concentration	4.5 mmol L^{-1}	4.5 mmol L^{-1}	2.0 mmol L^{-1}
Supporting solution		K_2SO_4 , 13 mmol L^{-1}	

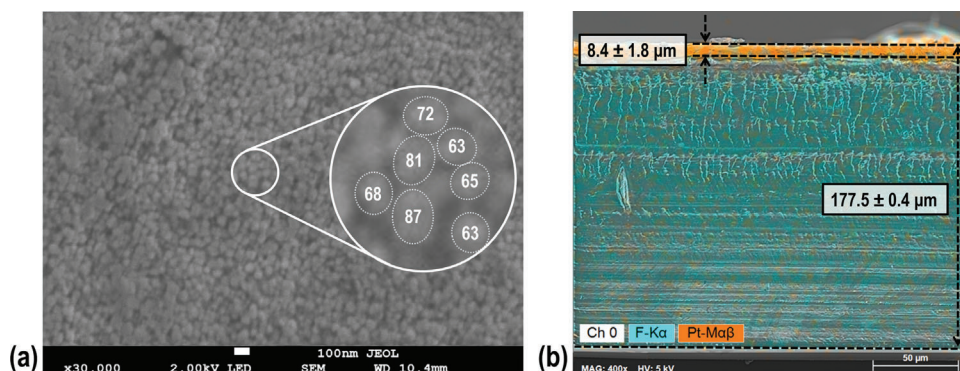


Figure 1. a) SEM image of the IPMC surface which has undergone a $200 \text{ mmol L}^{-1} \text{KBH}_4$ reduction step, revealing spherical and elliptical nanoparticles which were measured using digital image processing software (additional 400% digital zoom in the circular segment). Values represent the (longest) diameter of individual nanoparticles. b) For facilitated visual interpretation of the SEM/EDX image of the cross-section of the electrode, characteristic fluorescence energies of fluorine and platinum were colored, representing the bulk Nafion material (turquoise, $178 \mu\text{m}$ total thickness) and the incorporated surficial Pt layer (orange) with a thickness of $\approx 8 \mu\text{m}$.

2.2. Influence of Synthesis Parameters on the Physicochemical Properties of Sensor Material

The synthesis leads to flexible IPMC sensor materials which vary in visual appearance, depending on the synthesis conditions. All sensor materials show substantial staining of the underlying Nafion substrate which ranges from a translucent gray darkening to a solid matte black appearance on both sides and even to a silver-colored, mirror-like front finish (see Table 2). The reduced translucence of the sensor materials is accompanied by an increase in the perceived resistance to elastic deformation.

When simply comparing the visual appearance, it becomes apparent that the choice of reducing agent bears a considerable impact. The use of hydrazine (N_2H_4) only leads to an extensively stained sensor material which hints at a low Pt loading. Under the

given conditions, tetraborohydride acts as a powerful reducing agent^[45] and leads to substantially reduced visual transparency, which can be completely blocked at lower reductant concentrations due to the formation of a solid metal deposit on the IPMC surface.

In order to obtain the morphological properties of the synthesized IPMC electrodes, SEM studies were conducted. For an exemplary sensor material, both the surface and cross-section are displayed in Figure 1.

By observing the sensor materials at a magnification level of 30 000 in Figure 1a, surficial layers of structured metal deposits become clearly visible. Agglomerates are identified as spherical-shaped Pt nanoparticles via EDX with mean particle sizes ranging between 40 and 90 nm. This is larger than reported for layers obtained under comparable conditions at elevated temperatures^[43,46] or from recast Nafion solutions.^[47,48]

However, this observation is only valid for sensor materials that have undergone a reduction using tetraborohydrides, as hydrazine solutions did not result in electrodes which allowed for the identification of individual Pt particles. Furthermore, for the given dataset, statistically significant smaller particle sizes are measured when using KCl or K_2SO_4 electrolytes in contrast to UPW. For all sensor materials, additional cross-sections were prepared and evaluated. EDX analyses revealed that the applied synthesis procedure leads to controlled one-sided precipitation of Pt particles, which can be a valuable feature for an IPMC sensor design. Obtained layer thicknesses are within a range of 2.2 to 12.6 μm , which is in accordance with the results achieved by other researchers^[40,49] although even thinner layers have been reported previously, partially using elevated temperatures.^[41,50] Electrodes that were prepared with hydrazine as the reducing agent yielded no defined Pt layer that could be identified via SEM/EDX. This is because, in contrast to the anionic borohydride, hydrazine is not subject to Donnan exclusion^[51] and can thusly undergo diffuse reduction reactions over the entire cross-section of the IPMC material.

For accurate measurements, the sensor material has to be digested and is consequently destroyed during the quantification process. For that reason, the applicability of radiography as an alternative non-destructive method was evaluated to reliably approximate the Pt loading by determining the radiographic blackening caused by X-ray absorption. This technique makes use of differing material contrasts between the polymer substrate and the incorporated heavy metal atoms.

After the digital reconstruction of the radiographic image, a gray value image is obtained. As within the 8-bit grayscale 256 different shades of gray or black can be differentiated, this leads to a discrimination limit of $\approx 0.4\%$. In Figure 2 the obtained radiographic blackening values are displayed with respect to the elemental content found after digestion and atomic spectroscopy.

The obtained Pt loadings in this study range from 0.01 to 1.52 $mg\ cm^{-2}$ and comply with the range of sensor materials reported in the literature, which usually exhibit a noble metal loading of 0.1 to 4 $mg\ cm^{-2}$.^[21,41,49,52] Elevated levels of Pt loading in the final product are shown to be obtained primarily by increasing the initial Pt concentration of the impregnation solution. For the given electrodes, a corresponding radiographic blackening from 22.0% to 34.3% was observed. However, it must be noted that any contribution to an increased gray value may also be caused in part by incorporated elements other than Pt due to incomplete restoration of the initial, fully H^+ -loaded state during the work-up. For Pt loadings in the range of 0 to 0.3 $mg\ cm^{-2}$, the calculated gray values exhibit considerable deviations, implying comparable analytical limitations as gravimetric approaches.

When all sensor materials are considered, a coefficient of determination $R^2 = 0.725$ for a linear regression model is obtained, which is insufficient for analytical purposes. In contrast, when omitting electrodes with KCl or K_2SO_4 electrolytes, an improved $R^2 = 0.876$ can be achieved. This allows for a reasonable, non-destructive estimation of the absolute Pt loading, especially for higher loading values. While previous work on the radiographic determination of heavy metal contents yielded even higher R^2 values, these studies have predominantly focused on aqueous matrices, enabling more advanced measuring and quantification

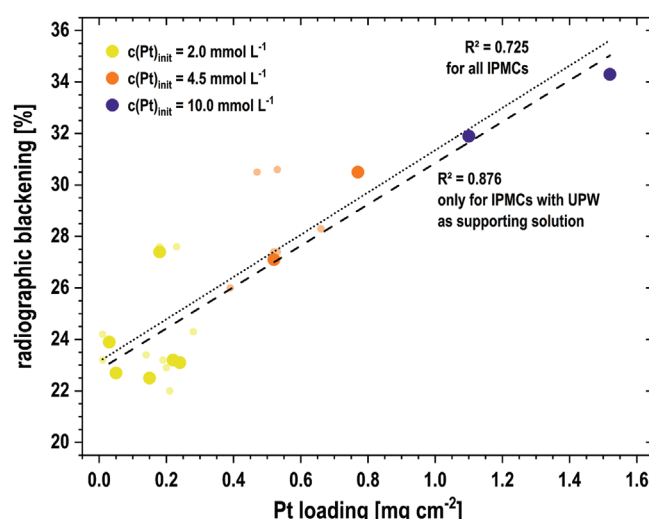


Figure 2. Scatter plot of averaged radiographic blackening versus mean Pt loading for individual specimens, determined via digestion and spectroscopic determination. The color scale of the data points correlates with the initial Pt concentration. Smaller data points represent sensor materials prepared with KCl or K_2SO_4 electrolytes whereas larger data points show specimens prepared with ultrapure water as supporting solution. Discrete group formation hints at higher Pt concentrations during synthesis also leading to higher elemental content in the final IPMC electrode. Linear trend functions were estimated for all sensor materials (dotted line) as well as only those IPMCs obtained using ultrapure water as a supporting solution (dashed line).

methods.^[53,54] Nonetheless, the proposed method may already be sufficient for technical applications (e.g. process and quality control).

A comprehensive overview of the physicochemical parameters obtained for all synthesis conditions is given in Table 3. For several specimens, a distinguishable nanostructured Pt layer could not be characterized during SEM analysis and therefore no value is given for layer thickness and/or particle size (denoted n.d.). To ensure highest accuracy for all synthesis conditions, the reported Pt loading values are all obtained from ICP OES measurements.

2.3. Evaluation of the Performance of Synthesized IPMC Materials as Potentiometric Electrodes for Ozone Sensing

Prior to a measuring sequence, all synthesized specimens were equilibrated for 24 h with ultrapure water, resulting in a stable voltage baseline (U_b) between the IPMC and the IrO_x reference electrodes. A substantial change in voltage is observed within 2 min after exchanging the ultrapure water with ozonated UPW, as dissolved ozone molecules interact with the electrode surface. Once the maximum voltage (U_{max}) is reached, it is followed by a slow signal decrease back to the initial voltage U_b over a time period of up to 10 h due to successive ozone decomposition. Exposing the sensor material to solutions with higher content of dissolved ozone leads to a correspondingly increased sensor signal. A stable voltage baseline signal was always re-obtained over the measurement period of about two weeks per specimen, indicating no significant irreversible changes in sensing properties

Table 3. Comprehensive overview of the physicochemical properties obtained for the 25 sensor materials depending on their respective synthesis conditions. Sensor materials are sorted by their initial Pt impregnation solution concentration, reducing agents, reductant concentration, reduction strategy, and supporting solution. Mean values are given for the Pt loading leached from the electrode, radiographic blackening as well as Pt layer thickness and particle sizes (rounded to the nearest 5 nm).

#	Synthesis parameters					Measured physicochemical IPMC properties			
	Initial <i>c</i> (Pt) [mmol L ⁻¹]	Reducing agent	Initial <i>c</i> (red.) [mmol L ⁻¹]	Reduction strategy	Supporting solution	Pt loading [mg cm ⁻²]	Blackening [%]	Layer thickness [μm]	Particle size [nm]
1	10.0	NaBH ₄	200	1 × 60 min	UPW	1.52	34.3	5.0	n.d.
2	10.0	NaBH ₄	40	3 × 20 min	UPW	1.10	31.9	4.5	90
3	4.5	NaBH ₄	200	1 × 60 min	KCl	0.66	28.3	6.7	75
4	4.5	NaBH ₄	40	3 × 20 min	KCl	0.39	26.0	10.2	55
5	4.5	KBH ₄	200	1 × 60 min	UPW	0.77	30.5	8.4	65
6	4.5	KBH ₄	200	1 × 60 min	KCl	0.47	30.5	7.9	45
7	4.5	KBH ₄	200	1 × 60 min	K ₂ SO ₄	0.53	30.6	5.7	65
8	4.5	KBH ₄	40	3 × 20 min	UPW	0.52	27.1	4.3	70
9	4.5	KBH ₄	40	3 × 20 min	KCl	0.53	27.4	12.6	50
10	4.5	KBH ₄	40	3 × 20 min	K ₂ SO ₄	0.52	27.4	2.2	75
11	2.0	NaBH ₄	200	1 × 60 min	UPW	0.24	23.1	7.5	n.d.
12	2.0	NaBH ₄	200	1 × 60 min	K ₂ SO ₄	0.19	23.2	5.5	n.d.
13	2.0	NaBH ₄	200	3 × 20 min	UPW	0.22	23.2	8.7	n.d.
14	2.0	NaBH ₄	200	3 × 20 min	KCl	0.20	22.9	5.5	65
15	2.0	NaBH ₄	200	3 × 20 min	K ₂ SO ₄	0.14	23.4	6.8	40
16	2.0	NaBH ₄	40	1 × 60 min	K ₂ SO ₄	0.28	24.3	4.3	55
17	2.0	NaBH ₄	40	3 × 20 min	UPW	0.15	22.5	5.7	85
18	2.0	NaBH ₄	40	3 × 20 min	K ₂ SO ₄	0.21	22.0	3.8	50
19	2.0	KBH ₄	200	3 × 20 min	UPW	0.18	27.4	7.9	n.d.
20	2.0	KBH ₄	200	3 × 20 min	KCl	0.23	27.6	7.4	70
21	2.0	KBH ₄	200	3 × 20 min	K ₂ SO ₄	0.18	27.6	10.3	n.d.
22	2.0	N ₂ H ₄	2000	1 × 60 min	UPW	0.03	23.9	n.d.	55
23	2.0	N ₂ H ₄	2000	1 × 60 min	KCl	0.01	23.2	n.d.	n.d.
24	2.0	N ₂ H ₄	25 000	1 × 60 min	UPW	0.05	22.7	n.d.	n.d.
25	2.0	N ₂ H ₄	25 000	1 × 60 min	K ₂ SO ₄	0.01	24.2	n.d.	n.d.

due to, for example, degradation effects and therefore not limiting the reusability of the presented sensor materials. As an example displayed in **Figure 3a**, varying ozone concentrations in a range of 0.07 to 0.83 mg L⁻¹ resulted in signal responses from 75 to 200 mV.

In an aqueous solution, dissolved ozone undergoes a complex decomposition mechanism, which is strongly affected by the given reaction conditions. However, there is no univocal model for ozone decay, hence reaction orders ranging from 1 to 2 are discussed in the literature.^[55–57] Since the experiments in the present study were performed under atmospheric conditions, all solutions were slightly acidic (pH ≈ 5.5) and ensured that the pH-sensitive IrO_x electrode produced a well-defined reference potential. As first-order kinetics are preferably applied for acidic environments, this approximation was chosen and yielded a fit with $R^2_{adj.} > 0.96$. This enabled us to quantify the mean half-life of the unstable ozone solutions colorimetrically as 80 min, which is in congruence with the findings of previously reviewed studies.^[55] Therefore, the concentration at the measured peak maximum

$\beta(O_3)_{t(U_{max})}$ was calculated according to Equation (1) based on the measured initial ozone concentration $\beta(O_3)_{t=0}$.

$$\beta(O_3) = \beta(O_3)_{t=0} \cdot e^{-k \cdot t} = \beta(O_3)_{t=0} \cdot 2^{-\frac{t}{t_{1/2}}}$$

$$\text{with } t_{1/2} = \frac{\ln(2)}{k} \quad (1)$$

The measured voltage differences ($\Delta U_{max} = U_{max} - U_b$) for these potentiometric sensors form response curves that are a function of the ozone concentration at peak maximum (**Figure 3b**). As the experimental setup only allows the observation of transient voltage signals, a true adsorption equilibrium cannot be established due to successive ozone decay. Furthermore, ozone shows reactive adsorption, as only atomic oxygen forms a chemisorption layer on the Pt surface.^[58] Since ozone molecules are not re-formed during the subsequent desorption, an equilibrium state cannot be achieved either. Instead, a slow, kinetically inhibited desorption of surface-bound oxygen atoms occurs,

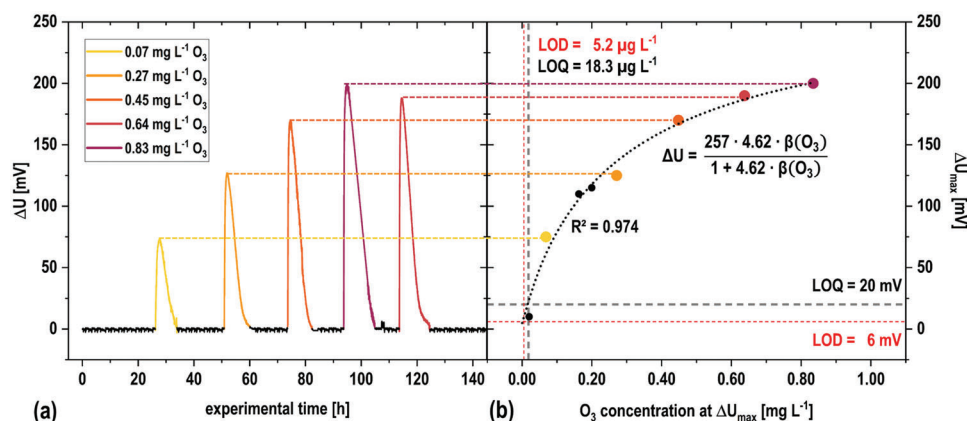


Figure 3. a) Baseline-corrected potential curve for an exemplary representative sensor (#18). Colors indicate the sensor response to ozonated water of different concentrations. Higher ozone concentrations are linked to higher sensor voltages. Over the course of several hours, the signal drops back to the same, stable baseline level due to successive ozone decomposition even when a lower ozone concentration follows the measurement of a higher concentrated solution, indicating the absence of a ‘carryover effect’. b) Sensor response as a function of the calculated ozone concentration at peak maximum for sensor #18. Colored dots are directly derived from (a) whereas black dots represent additional data points obtained for this sensor. The sensor response curve is satisfactorily described by a Langmuir pseudo-isotherm. Additionally, the analytical limits for detection (light red dashed lines) and quantification (light gray dashed lines) are shown in terms of the electrical signal as well as ozone concentration.

possibly as O_2 due to recombination.^[59] Therefore, the obtained response curves are only described by pseudo-isotherms.

In order to characterize the occurring adsorption behavior, the Freundlich^[60] and Langmuir^[61] models were fitted to the experimental data and compared by Akaike’s information criterion (AIC_c) for small sample sizes (Equation (2)).^[62,63] Herein, N is the number of data points per sensor, K is the number of parameters within the regression model, and RSS is the residual sum of squares.

$$AIC_c = N \cdot \ln \left(\frac{RSS}{N} \right) + 2K + \frac{2K^2 + 2K}{N - K - 1} \quad (2)$$

As for the vast majority of sensors lower AIC_c values are obtained for the Langmuir pseudo-isotherm, this model seems more suitable to explain the sensor response curves and suggests that only a monolayer of adsorbates is formed on the Pt surface. To further account for possible deviations from a strict pseudo-Langmuir behavior, both the Redlich–Petersen^[64] and Sips^[65,66] isotherms are also considered suitable regression models.^[67] However, the gain in the goodness of fit does not lead to an overall decrease in AIC_c values (see Table 4) and therefore does not justify the introduction of a third regression parameter, also preventing overfitting. Hence, the Langmuir pseudo-isotherm model (Equation (3)) is selected for subsequent sensor characterization.

$$\Delta U_{\max} \left(\beta(O_3)_{t(U_{\max})} \right) = f \cdot q_e = \frac{q_{\max} \cdot K_L \cdot \beta(O_3)_{t(U_{\max})}}{1 + K_L \cdot \beta(O_3)_{t(U_{\max})}} \quad (3)$$

Herein, q_e is the relative occupancy of adsorption sites at pseudo-equilibrium, $q_{\max} = f \cdot q_L$ is the adjusted maximum adsorption capacity of the adsorbent (Pt surface of IPMC electrode), K_L is the Langmuir constant related to the affinity of adsorption, and $\beta(O_3)_{t(U_{\max})}$ is the pseudo-equilibrium concentration of the adsorbate (dissolved ozone). In the context of this study, the

pseudo-Langmuir model assumes an approximate direct proportionality between the measured sensor voltage and the pseudo-equilibrium occupancy, which is given by the proportionality factor f in the equation above. This formal scale factor accounts for different physical dimensions incorporated into the equation. Under the assumption that q_e approaches the limit of 1, the numerical value of f becomes equal to q_{\max} for every individual sensor.

This assumption is supported by the typical cyclic voltammetry of Pt on Nafion as a working electrode in purified water.^[68] In the potential range where chemisorption of oxygen adsorbates occurs on the Pt surface (oxygen underpotential deposition), the observed $I(U)$ profile can be approximated by a rectangular graph and thus be interpreted as a capacitor, where the amount of electric charge (given by the anodic current integral in this region) linearly depends on the electrode potential. As the surface coverage of adsorbed oxygen is proportional to the electric charge,^[59] the assumption of linear proportionality is justified.

For LOD and LOQ estimation, the noise of the signal baseline was determined to be the limiting characteristic and its standard deviation was quantified to $\sigma_b = 2$ mV, also taking the resolution of the measuring equipment into account. Hence, LOD ($3 \sigma_b$) and LOQ ($10 \sigma_b$) correspond to voltages of $\Delta U_{\max} = 6$ and 20 mV, respectively. By solving Equation (3) for $\beta(O_3)_{t(U_{\max})}$, Equation (4) is obtained and yields individual concentration values for the different synthesized sensors.

$$\beta(O_3)_{t(U_{\max})} = \frac{\Delta U_{\max}}{K_L \cdot (q_{\max} - \Delta U_{\max})} \quad (4)$$

Choosing the most suitable sensor strongly depends on the specific application: If ozone concentrations typically occur in the low $\mu g L^{-1}$ range (i.e. low LOD values are desired), a steep calibration curve with higher values for K_L is preferred. On the other hand, if a larger dynamic range is required, then sensors with a lower K_L value but higher q_{\max} values should be selected.

Table 4. Comprehensive overview of the ozone-sensing properties obtained for the sensors listed in Table 3. AIC_c values were calculated for the Freundlich (FR), Langmuir (LA), Redlich–Petersen (RP), and Sips (SI) pseudo-isotherm models. Langmuir pseudo-isotherm regression parameters are given for each sensor as well as the adjusted coefficient of determination (R^2_{adj}) and the limits of detection (LOD) and quantification (LOQ).

#	AIC_c values				Pseudo–Langmuir fit parameters			Analytical parameters	
	FR	LA	RP	SI	q_{max} [mV]	K_L [L mg ^{−1}]	R^2_{adj}	LOD [μg L ^{−1}]	LOQ [μg L ^{−1}]
1	48.8	46.8	66.7	65.8	426	10.90	0.861	1.3	4.5
2	35.8	31.9	49.3	49.3	281	2.48	0.971	8.8	30.9
3	40.7	35.3	55.2	53.9	290	5.53	0.974	3.8	13.4
4	46.9	48.1	56.8	56.8	280	5.06	0.834	4.3	15.2
5	61.6	57.2	66.3	64.0	583	7.42	0.880	1.4	4.8
6	52.6	52.8	58.9	58.9	357	10.03	0.890	1.7	5.9
7	73.4	68.4	73.9	73.8	597	12.75	0.930	0.8	2.7
8	56.2	53.2	60.3	58.6	418	2.14	0.898	6.8	23.5
9	43.9	43.4	34.3	30.4	1023	0.79	0.793	7.4	25.1
10	40.2	37.2	44.7	38.2	381	1.08	0.941	14.8	51.3
11	66.2	68.0	70.1	70.1	454	13.58	0.881	1.0	3.4
12	30.8	32.8	50.6	50.8	324	20.45	0.848	0.9	3.2
13	50.3	44.4	64.3	64.4	567	19.41	0.959	0.6	1.9
14	53.5	44.2	50.3	49.0	722	2.34	0.967	3.6	12.2
15	63.5	64.9	69.4	68.9	647	11.61	0.881	0.8	2.7
16	58.7	55.9	62.8	59.8	542	7.24	0.783	1.5	5.3
17	48.5	48.2	56.9	56.4	351	21.82	0.891	0.8	2.8
18	46.3	41.4	45.5	46.2	257	4.62	0.974	5.2	18.3
19	62.0	53.6	59.7	59.6	435	12.42	0.941	1.1	3.9
20	49.4	48.7	67.8	67.9	561	36.05	0.872	0.3	1.0
21	57.7	51.2	55.0	53.6	621	25.97	0.974	0.4	1.3
22	50.8	52.2	59.8	60.2	364	13.27	0.874	1.3	4.4
23	63.8	60.6	66.9	66.2	572	6.71	0.899	1.6	5.4
24	62.8	45.2	52.0	51.8	495	23.65	0.989	0.5	1.8
25	49.8	45.0	64.5	65.0	686	10.94	0.958	0.8	2.7

An overview of the pseudo–Langmuir regression parameter derived from the sensor response curves as well as resulting LOD and LOQ values are given in Table 4.

For most regressions, an adjusted coefficient of determination $R^2_{adj} > 0.85$ is achieved, indicating a sufficient description of the data points by the pseudo–Langmuir regression model. The calculated q_{max} values range from 257 to 1023 mV and suggest a notable span in the obtained surface properties as q_{max} represents the upper limit for an observable change in voltage when all binding sites on the sensor surface are occupied by analyte molecules. For the parameter K_L , which is linked to the energy of adsorption, values range from 0.79 to 36.05 L mg^{−1} and thus exceed an order of magnitude. This further implies differences concerning the surfaces of the individual sensors as larger K_L values are related to stronger interactions between the adsorbate and adsorbent.^[61] However, the obtained values for q_{max} and K_L exhibit a much broader range than expected as the adsorption behavior is primarily a material property of Pt in the presence of ozone. In consequence, while the Langmuir pseudo-isotherm yields the most suitable fit according to the AIC_c criterion, it is

indicated that other models may consider the occurring phenomena more accurately.

Considering all sensors, mean LOD and LOQ values of 2.9 and 9.9 μg L^{−1} are determined, respectively. These limits enable confident monitoring of UPW for the application during pharmaceutical-grade water sanitization.

2.4. Evaluation of General Trends between Synthesis Parameters, Physicochemical Properties, and Ozone-Sensing Behavior

The aforementioned findings show that both the physicochemical and ozone-sensing properties are strongly influenced by the selected synthesis conditions. It would therefore be desirable to identify underlying correlations in order to enable tailoring IPMC sensors to their specific application in disinfection monitoring. The accurate calculation of numerical relations from the presented dataset bears challenges as a fractional factorial study design was deliberately chosen to limit high-value resources (e.g. platinum, Nafion). While this approach cannot resolve all

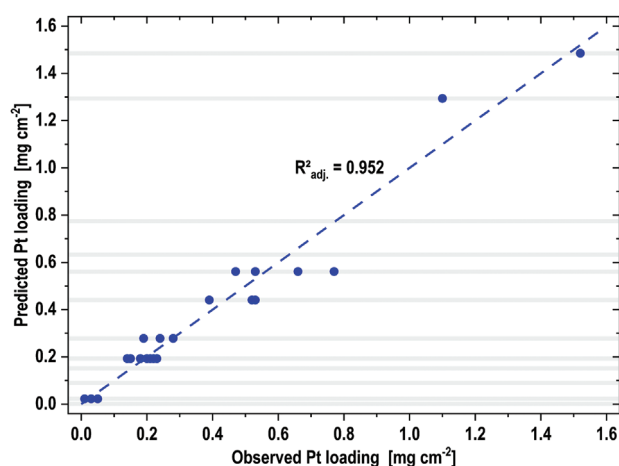


Figure 4. Plotting the predicted (according to Equation (6)) versus observed values for the regression model of the Pt loading indicates a good model accuracy ($R^2_{adj.} > 0.95$). A step-like profile of the calculated data points arises from the fact that the regression model is based on a limited amount of input parameters and can only assume a defined number of levels for the given dataset (gray horizontal lines).

higher-order interactions due to confounding factors, this can be considered a minor issue, as only a small proportion of all variables exhibit statistically significant effects (effect sparsity principle^[69]) and main effects are more likely to be important than two-factor or higher-order interactions (hierarchical ordering principle^[70]). Therefore, the study design is justified by allowing the beneficial extraction of general trends from a cost-effective screening of synthesis conditions affecting the physicochemical and sensing properties.

Both the direct correlations between synthesis parameters and sensing properties as well as correlations between physicochemical properties and sensing properties were considered. However, valid models were only established for certain properties, with the best results found for Pt loading, demonstrated in **Figure 4**.

To verify whether all prerequisites for the multiple linear regression analysis are given, both the normal distribution and homoscedasticity of the residuals are evaluated. For the Pt loading a Box-Cox transformation (Equation (5)) of the dataset had to be performed.^[71] As a result, only a few data points exhibit large residuals, that is, for a majority of data points there are only minor deviations between the measured values and the modeled data. This can also be seen in Figure 4 as the overall model shows a good agreement between observed and predicted data ($R^2_{adj.} > 0.95$). This is especially remarkable as the refined model merely requires information about the initial Pt concentration, the selected reducing agent, and the applied reduction strategy (Equation (6)). In turn, a reliable prediction of Pt loadings may be used to prepare IPMCs with defined physicochemical properties even beyond sensing applications by employing the presented model.

$$\text{Pt loading}_{\text{trans}} = \frac{(\text{Pt loading})^\lambda - 1}{\lambda} \quad \text{with } \lambda = 0.545 \quad (5)$$

$$\text{Pt loading}_{\text{trans}} = 0.174 + 0.598 \cdot c(\text{Pt})_{\text{init}} - 2.391$$

$$\begin{array}{|c|c|c|} \hline \text{Red. agent} & -0.580 \cdot & \text{Red. strategy} \\ \hline 1 \text{ for } \text{N}_2\text{H}_4 & & 1 \text{ for } 3 \times 20 \text{ min} \\ 0 \text{ for } \text{NaBH}_4, \text{KBH}_4 & & 0 \text{ for } 1 \times 60 \text{ min} \\ \hline \end{array} \quad (6)$$

Furthermore, it can be observed that the calculated data points form horizontal lines, resulting in a step-like profile. This is a direct consequence of the underlying regression model consisting of just three input parameters which were varied on only 2 or 3 defined levels for the given dataset. As a result, no more than 12 different levels of Pt loading can be extracted from the regression model. Yet, this degree of differentiation is already sufficient for a reasonable estimation of the metal loading, merely on the basis of given synthesis conditions and without the necessity of performing any measurements on the manufactured products. Other synthesis variables, such as, for example, the concentration of the reducing agent, have shown to be less important as they were not limiting the reduction process and were subsequently not implemented into the refined regression model for Pt loading.

An overview of all successfully established regression models is given in **Figure 5**. Only those models are included that achieved a $p < 0.05$ and $R^2_{adj.} > 0.50$ to ensure sufficient model adequacy and significance for a general estimation of physicochemical or sensing properties. In this context, the p -value indicates the probability that the identified correlation was randomly obtained. Just four of all evaluated and refined models fulfill these criteria, the remainder led to insufficient fits or poor significance. In consequence, no significant models were established to describe the expected sensing properties merely based on given synthesis conditions. All obtained regression models are purely based on main effects; two-factor interactions were considered but none were identified as being statistically significant. In general, factors with $p < 0.05$ were typically not included in the model refinement unless explicitly stated. Equations for the remaining regression models are given in Supporting Information.

For the radiographic blackening, a statistically significant and adequate model was obtained. In contrast to the Pt loading regression model, the choice of either NaBH_4 or KBH_4 shows a statistically significant distinction with respect to the blackening, which is a direct result of different mass attenuation coefficients of remaining cations in the Nafion structure. A rather decent model was also obtained for the Pt layer thickness. With a p -value of 0.11, the use of a supporting solution shows a formally insignificant effect, however, omitting this minor factor from the regression has been shown to degrade the quality of the model substantially.

The presented dataset yielded no valid regression models between the synthesis parameters and the sensing properties and therefore does not allow for a direct correlation. Apparent patterns in some Q-Q plots, irrespective of the choice of variables, indicate that there may be further, complex influencing factors that have not been considered so far. In a related context, Sakthivel et al. have previously indicated a relationship between surface morphology and the choice of borohydride salt.^[31] However, with K_L (expressing the pseudo-Langmuir curvature), a single structure-property relationship is successfully described by a statistically significant model. Although blackening and Pt

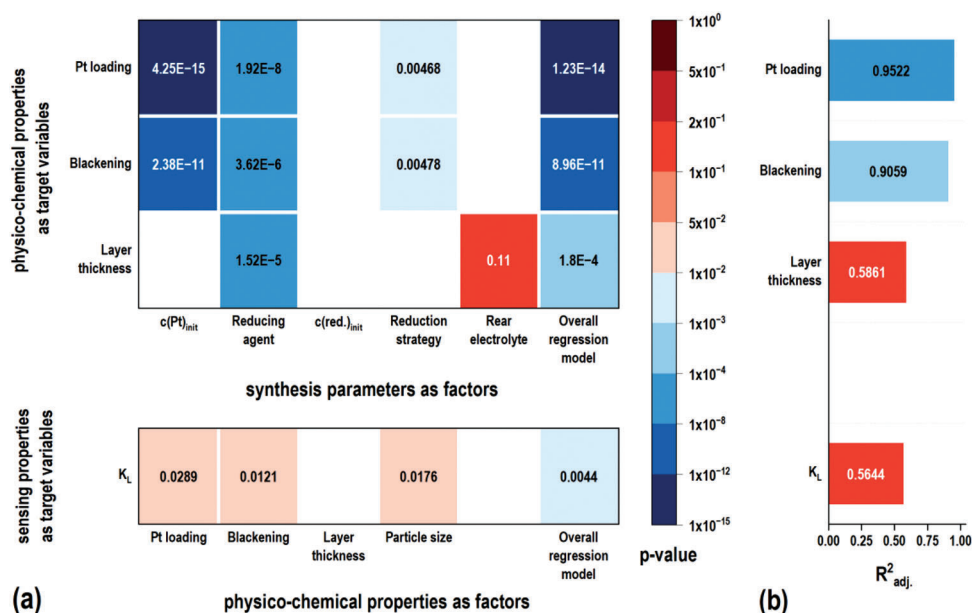


Figure 5. a) Heatmap of p -values for all multiple linear regression models that yielded sufficient model adequacy and significance. The color gradient corresponds to the p -values, with blue tiles of varying intensity referring to factors of higher significance ($p < 0.01$). b) Adjusted coefficients of determination for the obtained valid regression models. For Pt loading and blackening $R^2_{\text{adj.}} > 0.90$ were achieved.

loading were expected to describe somewhat redundant information, both factors contribute significantly to the model, while layer thickness was excluded during model refinement due to insignificance. Furthermore, particle size is another contributing factor to this model; however, since missing values had to be considered, this resulted in a loss in statistical power due to fewer data points for model refinement. Yet, removing the particle size from the regression model would also lead to lower $R^2_{\text{adj.}}$ values.

3. Conclusion

In this study, platinum-based IPMCs were synthesized using a simple laboratory-scale setup and characterized with respect to the intended use as potentiometric sensors for the quantification of dissolved ozone in UPW monitoring. Depending on the selected synthesis parameters the obtained sensor materials vary greatly in appearance and feature nanostructured Pt surfaces with particle diameters in the range of 40 to 90 nm. The formation of contiguous Pt layers only occurred when using tetraborohydrides as reducing agents, however, IPMCs prepared with hydrazine also led to sensitive ozone sensors despite possessing low Pt loadings.

As common non-destructive determination methods for the individual metal loading are limited due to gravimetric resolution, a radiographic approach was evaluated and allows for a sufficient estimation of the Pt content. However, for low Pt loadings, other incorporated elements may contribute considerably to the overall X-ray absorption, impairing the accuracy of the method.

Sensor response properties in ozonated water can be conclusively described by Langmuir pseudo-isotherms in the potentiometric measuring setup. Mean LODs of $\approx 3 \mu\text{g L}^{-1}$ were enabled, qualifying the materials as suitable sensors in pharmaceutical systems for cold water storage.

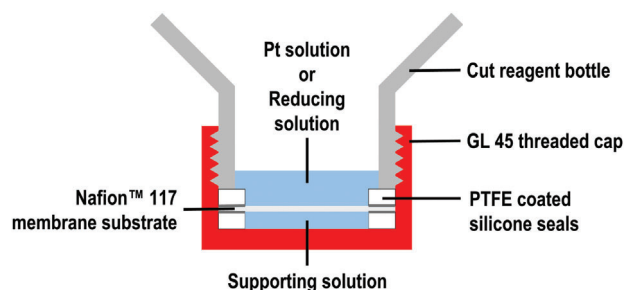


Figure 6. Schematic model of the experimental setup: The reagent bottle, its threaded cap, and two sealing discs allow the Nafion membrane to be contacted simultaneously by both the Pt solution or the reducing solution from above and the supporting solution from beneath.

Even from a limited dataset, it is possible to accurately correlate selected physicochemical properties with given synthesis conditions, however, sensing properties did not yield satisfying regression models. An assumed influence by the supporting solution was only identified for the Pt layer thickness. By improving the microscopic analysis of particle sizes, especially for smaller nanoparticles expected when using hydrazine as a reductant, modeling of sensing properties might be achievable at a higher accuracy and significance.

The obtained results contribute to prospective targeted syntheses of cost-effective IPMC sensor materials with defined physicochemical properties and enable miniaturized sensor setups that can be retrofitted at various key spots within UPW storage systems. Future studies can improve by a larger range of different sensors, which would be more feasible with an optimized sensor design to require even fewer resources. Furthermore, the observed sensor response and reset times limit monitoring

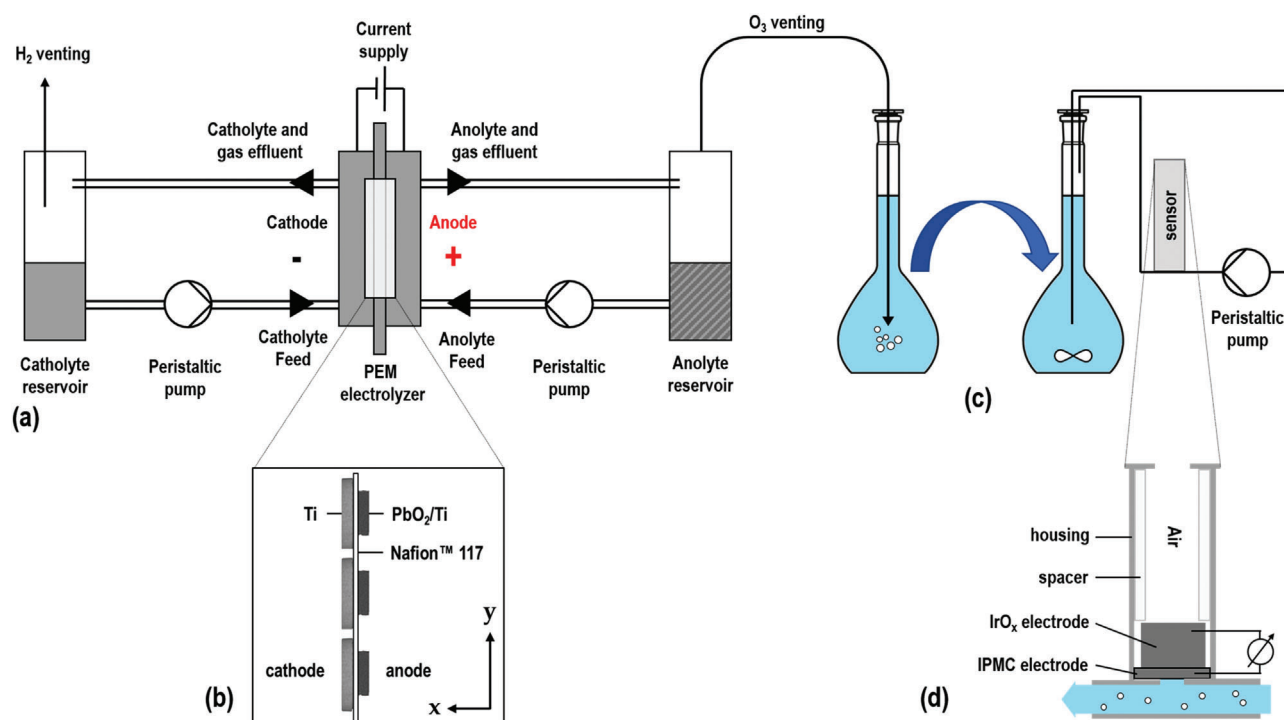


Figure 7. Scheme of the experimental setup for a) ozonated water production and b) arrangement of the SMEA. 18.2 MΩ ultrapure water from the reservoir is pumped through both the anodic and cathodic half-cells of the PEM electrolyzer, with oxidants being dissolved into the anolyte. Gaseous ozone from the analytic cycle is bubbled into a separate ultrapure water reservoir to provide solutions with ozone as the only oxidant present. c) The ozonated water is then pumped along d) a simple sensor setup which allows for quick material exchange.

applications that demand quick response qualities and should gain further attention. A promising approach for this purpose may involve the presence of stabilizing agents during synthesis to better control Pt nanoparticle growth which might also be of interest for further applications of IPMCs.

4. Experimental Section

Preparation of Platinized Nafion Membrane Electrodes via Impregnation-Reduction Method: Nafion 117 membranes (Chemours, Wilmington, Delaware, USA) were conditioned according to Sakthivel et al.^[31] and placed in the apparatus depicted in **Figure 6**. The setup consisted of a GL 45 screw cap, the PEM (circular, $d = 41$ mm) placed between two silicone-PTFE seals (with circular center cut-out, $d = 35$ mm), and a horizontally cut PP reagent bottle. The lower cavity beneath the membrane provided a supporting solution while the funnel-shaped reagent bottle acted as the reservoir for the metal and reducing solutions to which the membranes were exposed during the impregnation-reduction process.

The synthesis followed and expanded the impregnation-reduction methods from the literature.^[23,31] All chemicals were in analytical grade quality and all solutions thereof were prepared from 18.2 MΩ UPW. Both UPW, as well as KCl and K₂SO₄ (Merck KGaA, Darmstadt, Germany) electrolytes (13 mmol L⁻¹), were evaluated as supporting solutions.^[40,52]

3 mL of the supporting solution was filled into the cavity before placing the prepared membrane substrate into the setup. Subsequently, a Pt(NH₃)₄Cl₂ (Aldrich, St. Louis, MO, USA) solution (10 mL) with defined concentration levels was allowed to impregnate the membrane with Pt for 1 h at room temperature, supported by a 3D platform rotator (Grant Instruments, Shepreth, United Kingdom). Thereafter, the impregnation solution was exchanged for a reducing solution (15 mL), prepared in an aqueous

NH₃/NH₄⁺ buffer system (100 mmol L⁻¹, $pH = 9.25$). Reducing agents and concentrations were varied in a fractional factorial design and include NaBH₄, KBH₄, and N₂H₄ (all VWR Chemicals, Radnor, PA, USA). The reduction treatment was carried out for 1 h under magnetic stirring. All 25 IPMC variations were synthesized as duplicates.

Structural and Elemental Characterization of the Synthesized Pt Layers: All characterization steps were performed after prior reloading and drying of the synthesized Pt/Nafion IPMCs. Pt loading values were determined by atomic emission spectroscopy on an ARCOS ICP OES system (Spectro, Kleve, Germany) after digesting circular cut-outs ($d = 6$ mm) in boiling aqua regia (12 mL) for 30 min and subsequent dilution with UPW. ICP OES measurements were carried out as triplicates at 1400 W incident power and an integration time of 12 s after a rinse time of 60 s.

The determination of both thickness, position, and uniformity of the Pt layers was performed using a 7200F field-emission scanning electron microscope (JEOL, Akishima, Japan) at 2 kV acceleration voltage. All samples were degassed and dried in a desiccator for at least 24 h before SEM analysis. The layer thickness was acquired via SEM imaging in a 10-fold determination at the cross-section of the composite material. The particle size was determined at five representative spots on the SEM image of the respective electrode surface using the ImageJ distribution Fiji.^[72] In order to enable Pt identification via Pt-Mα and Pt-Mβ emission lines, elemental analyses were carried out using a Bruker XFlash 6|60 EDX detector at 15 kV acceleration voltage.

Radiographic assessment of the Pt loading was performed using a Skyscan 1275 computed tomography scanner (Bruker, Billerica, MA, USA) at 15 kV acceleration voltage and 150 μA current with 16-bit image acquisition. Three representative circular sections ($d = 6$ mm) were taken from each radiograph and collected as a 2D color value dataset. Mean values were calculated from the individual pixels using OriginPro 2022 (OriginLab, Northampton, MA, USA) and the gray value of the individual electrodes was determined using the 256 gray levels available in the 8-bit grayscale depth.

Table 5. Overview of synthesis parameters, physicochemical properties, and sensing parameters evaluated in the present study. LOQ was not included in the multiple linear regression analysis due to linear dependency with LOD.

Synthesis parameters	Physicochemical properties	Sensing parameters
Initial Pt concentration	Pt loading	Langmuir fit parameter q_{max}
Reducing agent	Radiographic blackening	Langmuir fit parameter K_L
Initial reductant concentration	Layer thickness	Coefficient of determination R^2_{adj}
Reduction strategy	Particle size	Limit of detection LOD
Supporting solution		Limit of quantification LOQ

Characterization of Ozone Sensing Properties: To prepare aqueous solutions with defined ozone content, the setup depicted in **Figure 7** is used for all experiments. A structured membrane-electrode assembly (SMEA), consisting of a Nafion 117 membrane and seven pairs of PbO_2 -coated porous titanium anodes and porous titanium cathodes (all Innovatec Gerätetechnik GmbH, Rheinbach, Germany), was mounted within a PVC housing (as previously described in ref. [73]). The ozone-rich gas phase of the anodic half-cell was exhausted into a separate flask to prevent the introduction and subsequent measurement of other electrochemically formed oxygen species.

Subsequently, the ozonated water was stirred gently and pumped along the sensor setup shown in Figure 7d, containing one IPMC specimen per experiment (representing each synthesis condition), a PTFE spacer, and an IrO_x electrode (De Nora, Milan, Italy) assembled within a sealed housing. No additional reference electrode had to be incorporated as there is no current flow during the potentiometric measurement which would lead to a polarization of the IrO_x electrode. Furthermore, IrO_x has proven to provide a stable electrode potential ($E \approx 880$ mV vs SHE) while the surrounding media exhibit constant pH values.^[74–76] As Nafion fulfills this requirement under ultrapure water conditions, a stable reference electrode is thus guaranteed.^[77,78]

For sensor characterization experiments, the UPW used for sensor conditioning was replaced by ozonated ultrapure water with a target concentration range of $\approx 10 \mu g L^{-1}$ to $1.0 mg L^{-1}$. Sensor signals were acquired by measuring the potential between the Nafion-supported Pt surface (exposed to the ozonated water) and the IrO_x surface (exposed to ambient air). In order to allow for a justified extraction of regression parameters from the signal response properties, signals were collected for at least 5 different ozone concentrations.

At the same as the sensor was initially supplied with a new concentration level of ozonated water, the ozone content of the solution was quantified colorimetrically for an off-line sample via the DPD method in accordance with DIN 38408-3:2011-04, using KI, KIO_3 , Na_2HPO_4 , KH_2PO_4 , $Na_2S_2O_3$, H_2SO_4 , starch (all p.a. grade, Carl Roth, Karlsruhe, Germany), and DPD (N,N-diethyl-p-phenylenediamine sulfate; Merck, Burlington, MA, USA) on a DR6000 spectral photometer (Hach Lange, Düsseldorf, Germany). On a daily basis, the required I_2 solutions ($2.5 mmol L^{-1}$) were freshly prepared and checked for their titers with a $Na_2S_2O_3$ solution ($10 mmol L^{-1}$) using KIO_3 and KI as primary standards. The same procedure is used for the characterization of ozone decay within the setup displayed in Figure 7c.

Model Development and Statistical Analysis: Additional statistical evaluations were performed using the free software environment R for statistical computing,^[79] supported by the MASS package,^[80] in order to identify general trends between all groups of parameters measured and evaluated in the present study (see **Table 5**). A multiple linear regression analysis was chosen to estimate the magnitude and direction of selected factor effects by regressing the physicochemical properties and the sensing parameters with the synthesis conditions of the sensor materials. To integrate categorical variables in the regression models, dummy variables were used.

Due to the fractional factorial study design, not all factor interactions were considered; instead, higher-order interactions of three or more parameters were excluded as they can be considered less probable (hierarchical ordering principle).^[81] Furthermore, only selected two-factor interactions were evaluated, for which a cause-effect relationship was considered plausible.

Initial regression models that included all factors and assumed interactions were set up and refined. The developed reduced models only included statistically significant contributing factors, which were identified by analysis of variance. The model adequacy was verified with normal probability and residual plots, and a Box–Cox transformation was performed where applicable.^[71]

Supporting Information

Supporting Information is available from the Wiley Online Library or from the author.

Acknowledgements

This work was supported and financed by the Federal Ministry of Education and Research program “FHprofUnt” project “ReDeX” (grant number: 13FH107PX8). The authors gratefully acknowledge the support by Innovatec Gerätetechnik GmbH, in particular by Katharina van Dyk and Johannes Warmer, in providing materials and resources for the synthesis of the IPMC electrodes as well as for data collection setups. Furthermore, the authors acknowledge the support of Xuan Tung Do (Bonn-Rhein-Sieg University of Applied Sciences) in acquiring CT radiography files and of Amelia Heiner (Department of Material Science and Engineering, University of Utah, Salt Lake City, UT, USA) for proofreading.

Open access funding enabled and organized by Projekt DEAL.

Conflict of Interest

One of the authors, Samuel Stucki, works as scientific consultant for Innovatec Gerätetechnik GmbH which provided resources for the present study. All other authors declare no conflict of interest.

Data Availability Statement

The data that support the findings of this study are available from the corresponding author upon reasonable request.

Keywords

dissolved ozone, impregnation-reduction, ionic polymer metal composites, potentiometric sensors, ultrapure water

Received: December 2, 2022
Revised: March 21, 2023
Published online: April 23, 2023

- [1] United States Pharmacopoeia, Water for Pharmaceutical Purposes <1231>, USP 40 – NF35, **2017**.
- [2] European Pharmacopeia, 9th Edition, **2017**, p. 5790–5791.
- [3] X. Zhang, Y. Yang, H. H. Ngo, W. Guo, H. Wen, X. Wang, J. Zhang, T. Long, *Sci. Total Environ.* **2021**, 785, 147254.
- [4] Y. Choi, Y. June Choi, *Water Res.* **2010**, 44, 115.
- [5] M. Bourgin, E. Borowska, J. Helbing, J. Hollender, H. P. Kaiser, C. Kienle, C. S. McArdell, E. Simon, U. von Gunten, *Water Res.* **2017**, 122, 234.
- [6] M. Fabbicino, L. D'Antonio, *Environ. Technol.* **2012**, 33, 539.
- [7] W. Ding, S. Cao, W. Jin, X. Zhou, C. Wang, Q. Jiang, H. Huang, R. Tu, S.-F. Han, Q. Wang, *Water Res.* **2019**, 160, 339.
- [8] S. Stucki, D. Schulze, D. Schuster, C. Stark, *Pharm. Eng.* **2005**, 25, 40.
- [9] M. Florjanič, J. Kristl, *Drug Dev. Ind. Pharm.* **2006**, 32, 1113.
- [10] T. Wang, D. A. Reckhow, *Ozone: Sci. Eng.* **2016**, 38, 373.
- [11] H. Taube, *Trans. Faraday Soc.* **1957**, 53, 656.
- [12] J. Hoigné, H. Bader, W. R. Haag, J. Staehelin, *Water Res.* **1985**, 19, 993.
- [13] W. Gottardi, *Fresenius' J. Anal. Chem.* **1998**, 362, 263.
- [14] M. L. Kilpatrick, C. C. Herrick, M. Kilpatrick, *J. Am. Chem. Soc.* **1956**, 78, 1784.
- [15] S. Uchiyama, T. Ikarugi, M. Mori, K. Kasama, Y. Ishikawa, M. Kaneko, A. Umezawa, *Electroanalysis* **1993**, 5, 121.
- [16] J. H. Stanley, J. D. Johnson, *Anal. Chem.* **1979**, 51, 2144.
- [17] R. B. Smart, R. Dormond-Herrera, K. H. Mancy, *Anal. Chem.* **1979**, 51, 2315.
- [18] Y. Einaga, I. Tribidasarianggraningrum, Y. Ishii, S. Sekiguchi, K. Murata, US9625405B2, **2017**.
- [19] Y. Ishii, T. A. Ivandini, K. Murata, Y. Einaga, *Anal. Chem.* **2013**, 85, 4284.
- [20] K. Vandersmissen, F. De Smedt, C. Vinckier, *Ozone: Sci. Eng.* **2008**, 30, 300.
- [21] H. Takenaka, E. Torikai, Y. Kawami, N. Wakabayashi, *Int. J. Hydrogen Energy* **1982**, 7, 397.
- [22] S. D. Thompson, L. R. Jordan, M. Forsyth, *Electrochim. Acta* **2001**, 46, 1657.
- [23] P. S. Fedkiw, *J. Electrochem. Soc.* **1989**, 136, 899.
- [24] M. Rashid, T.-S. Jun, Y. S. Kim, *J. Nanosci. Nanotechnol.* **2013**, 13, 3627.
- [25] M. Sakthivel, W. Weppner, *J. Solid State Electrochem.* **2007**, 11, 561.
- [26] Y. Ming, Y. Yang, R. P. Fu, C. Lu, L. Zhao, Y. M. Hu, C. Li, Y. X. Wu, H. Liu, W. Chen, *Adv. Mater. Technol.* **2018**, 3, 1800257.
- [27] S. Biswas, Y. Visell, *Adv. Mater. Technol.* **2019**, 4, 1900042.
- [28] M. Parrilla, R. Cánovas, F. J. Andrade, *Electroanalysis* **2017**, 29, 223.
- [29] C. Ramesh, N. Murugesan, M. V. Krishnaiah, V. Ganesan, G. Periaswami, *J. Solid State Electrochem.* **2008**, 12, 1109.
- [30] Y. Tanaka, S. Uchinashi, Y. Saihara, K. Kikuchi, T. Okaya, Z. Ogumi, *Electrochim. Acta* **2003**, 48, 4013.
- [31] M. Sakthivel, W. Weppner, *Sensors* **2006**, 6, 284.
- [32] Y. C. Weng, K. C. Hung, *Sens. Actuators, B* **2009**, 141, 161.
- [33] L. Xie, J. Lu, H. Yan, *Electroanalysis* **1998**, 10, 842.
- [34] R. Knake, P. C. Hauser, *Anal. Chim. Acta* **2002**, 459, 199.
- [35] G. Schiavon, G. Zotti, G. Bontempelli, *Anal. Chem.* **1990**, 62, 293.
- [36] T. Chou, K. Ng, S. Wang, *Sens. Actuators, B* **2000**, 66, 184.
- [37] X. Z. Yuan, S. Zhang, J. C. Sun, H. Wang, *J. Power Sources* **2011**, 196, 9097.
- [38] Y. M. Obeidat, A. J. Evans, W. Tedjo, A. J. Chicco, E. Carnevale, T. W. Chen, *Sens. Actuators, B* **2018**, 276, 72.
- [39] T. Yin, W. Qin, *TrAC, Trends Anal. Chem.* **2013**, 51, 79.
- [40] N. J. C. Ingle, A. Sode, I. Martens, E. Gyenge, D. P. Wilkinson, D. Bizzotto, *Langmuir* **2014**, 30, 1871.
- [41] R. Liu, *J. Electrochem. Soc.* **1992**, 139, 15.
- [42] P. Hosseinabadi, M. Javanbakht, L. Naji, H. Ghafarian-Zahmatkesh, *Ind. Eng. Chem. Res.* **2018**, 57, 434.
- [43] A. Sode, N. J. C. Ingle, M. McCormick, D. Bizzotto, E. Gyenge, S. Ye, S. Knights, D. P. Wilkinson, *J. Membr. Sci.* **2011**, 376, 162.
- [44] J. Zhao, C. Huang, S. Zhang, F. Qu, R. Wang, H. Jiang, M. Yang, *Sens. Actuators, B* **2021**, 341, 129993.
- [45] B. L. Cushing, V. L. Kolesnichenko, C. J. O'Connor, *Chem. Rev.* **2004**, 104, 3893.
- [46] L. Daniel, A. Bonakdarpour, D. P. Wilkinson, *J. Power Sources* **2020**, 471, 228418.
- [47] P. C. Lee, T. H. Han, D. O. Kim, J. H. Lee, S. J. Kang, C. H. Chung, Y. Lee, S. M. Cho, H. G. Choi, T. Kim, E. Lee, J. Do Nam, *J. Membr. Sci.* **2008**, 322, 441.
- [48] P. C. Lee, J. E. Hyun, S. K. Jeoung, J. Do Nam, T. Hwang, K. J. Kim, K. C. Solasa, *Smart Mater. Struct.* **2019**, 28, 054003.
- [49] P. Millet, M. Pineri, R. Durand, *J. Appl. Electrochem.* **1989**, 19, 162.
- [50] D. G. Bessarabov, W. Michaels, R. D. Sanderson, *J. Membr. Sci.* **2000**, 179, 221.
- [51] H. Ito, T. Maeda, A. Nakano, H. Takenaka, *Int. J. Hydrogen Energy* **2011**, 36, 10527.
- [52] L. Daniel, A. Bonakdarpour, D. P. Wilkinson, *ACS Appl. Nano Mater.* **2019**, 2, 3127.
- [53] S. Dadashi, R. Poursalehi, H. H. Delavari, *Comput. Methods Biomech. Biomed. Eng.: Imaging Visualization* **2019**, 7, 420.
- [54] O. Rabin, J. M. Perez, J. Grimm, G. Wojtkiewicz, R. Weissleder, *Nat. Mater.* **2006**, 5, 118.
- [55] D. Gardoni, A. Vailati, R. Canziani, *Ozone: Sci. Eng.* **2012**, 34, 233.
- [56] J. Staehelin, J. Holgné, *Environ. Sci. Technol.* **1982**, 16, 676.
- [57] J. L. Sotelo, F. J. Beltran, F. J. Benitez, J. Beltran-heredia, *Ind. Eng. Chem. Res.* **1987**, 26, 39.
- [58] N. A. Saliba, Y. L. Tsai, C. Panja, B. E. Koel, *Surf. Sci.* **1999**, 419, 79.
- [59] H. Angerstein-Kozłowska, B. E. Conway, W. B. A. Sharp, *Chem* **1973**, 43, 9.
- [60] H. Freundlich, *Z. Phys. Chem.* **1907**, 57U, 385.
- [61] I. Langmuir, *J. Franklin Inst.* **1917**, 184, 721.
- [62] K. P. Burnham, D. R. Anderson, *Wildl. Res.* **2001**, 28, 111.
- [63] E. J. Wagenmakers, S. Farrell, *Psychon. Bull. Rev.* **2004**, 11, 192.
- [64] O. Redlich, D. L. Peterson, *J. Phys. Chem.* **1959**, 63, 1024.
- [65] R. Gutiérrez-Climente, A. Gómez-Caballero, N. Unceta, M. Aránzazu Goicolea, R. J. Barrio, *Electrochim. Acta* **2016**, 196, 496.
- [66] R. Sips, *J. Chem. Phys.* **1948**, 16, 490.
- [67] G. K. Rajahmundry, C. Garlapati, P. S. Kumar, R. S. Alwi, D. V. N. Vo, *Chemosphere* **2021**, 276, 130176.
- [68] Q. Wang, C. S. Cha, J. Lu, L. Zhuang, *Phys. Chem. Chem. Phys.* **2009**, 11, 679.
- [69] G. E. P. Box, R. D. Meyer, *Technometrics* **1986**, 28, 11.
- [70] C. J. Wu, M. S. Hamada, *Experiments: Planning, Analysis, and Optimization*, John Wiley & Sons, Hoboken, NJ **2011**.
- [71] G. E. P. Box, D. R. Cox, *J. R. Stat. Soc., Ser. B* **1964**, 26, 211.
- [72] J. Schindelin, I. Arganda-Carreras, E. Frise, V. Kaynig, M. Longair, T. Pietzsch, S. Preibisch, C. Rueden, S. Saalfeld, B. Schmid, J. Y. Tinevez, D. J. White, V. Hartenstein, K. Eliceiri, P. Tomancak, A. Cardona, *Nat. Methods* **2012**, 9, 676.
- [73] R. Grimmig, P. Gillemot, S. Stucki, K. Günther, H. Baltruschat, S. Witzleben, *Sep. Purif. Technol.* **2022**, 292, 121063.
- [74] O. C. Keller, J. Buffle, *Anal. Chem.* **2000**, 72, 936.

- [75] H. Yang, S. K. Kang, C. A. Choi, H. Kim, D. H. Shin, Y. S. Kim, Y. T. Kim, *Lab Chip* **2004**, 4, 42.
- [76] S. Yao, M. Wang, M. Madou, *J. Electrochem. Soc.* **2001**, 148, H29.
- [77] M. Wang, S. Yao, M. Madou, *Sens. Actuators, B* **2002**, 81, 313.
- [78] Z. Zhu, X. Liu, Z. Ye, J. Zhang, F. Cao, J. Zhang, *Sens. Actuators, B* **2018**, 255, 1974.
- [79] R Core Team, *R: A language and environment for statistical computing*. R Foundation for Statistical Computing Vienna, Austria **2020**, <https://www.R-project.org/>.
- [80] B. D. Ripley, W. N. Venables, *Modern Applied Statistics with S*, Springer, New York **2002**.
- [81] D. C. Montgomery, *Design and Analysis of Experiments*, John Wiley & Sons, Hoboken, NJ **2017**.

Paper: Operating an ozone-evolving PEM electrolyser in tap water: A case study of water and ion transport

Roman Grimmig, Philipp Gillemot, Samuel Stucki, Klaus Günther, Helmut Baltruschat, Steffen Witzleben

published in

Separation and Purification Technology, Volume 292, 121063, **2022**

DOI: 10.1016/j.seppur.2022.121063



Operating an ozone-evolving PEM electrolyser in tap water: A case study of water and ion transport

Roman Grimmig^{a,*}, Philipp Gillemot^a, Samuel Stucki^b, Klaus Günther^c, Helmut Baltruschat^d, Steffen Witzleben^a

^a Bonn-Rhein-Sieg University of Applied Sciences, Department of Natural Sciences, von-Liebig-Str. 20, 53359 Rheinbach, Germany

^b Innovatec Gerätetechnik GmbH, von-Liebig-Str. 6, 53359 Rheinbach, Germany

^c Research Centre Jülich, Institute for Bio- and Geosciences (IBG-2), Wilhelm-Johnen-Straße, 52428 Jülich, Germany

^d University of Bonn, Institute of Physical and Theoretical Chemistry, Römerstr. 164, 53117 Bonn, Germany

ARTICLE INFO

Keywords:

Mass transport
Nafion™
Ozone
PEM electrolysis
Permeation
Tap water

ABSTRACT

While PEM water electrolysis could be a favourable technique for *in situ* sanitization with ozone, its application is mainly limited to the use of ultrapure water to achieve a sufficient long-time stability. As additional charge carriers influence the occurring transport phenomena, we investigated the impact of different feed water qualities on the performance of a PEM tap water electrolyser for ozone evolution. The permeation of water and the four most abundant cations (Na^+ , K^+ , Ca^{2+} , Mg^{2+}) is characterised during stand-by and powered operation at different charge densities to quantify underlying transport mechanisms. Water transport is shown to linearly increase with the applied current ($95 \pm 2 \text{ mmol A}^{-1} \text{ h}^{-1}$) and occurs decoupled from ion permeation. A limitation of ion permeation is given by the transfer of ions in water to the anode/PEM interface. The unstabilized operation of a PEM electrolyser in tap water leads to a pH gradient which promotes the formation of magnesium and calcium carbonates and hydroxides on the cathode surface. The introduction of a novel auxiliary cathode in the anolytic compartment has shown to suppress ion permeation by close to 20%.

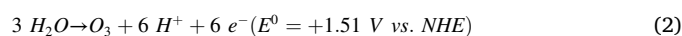
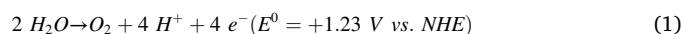
1. Introduction

Proton exchange membranes (PEM) present versatile constituents that enable efficient electrolyser and fuel cell systems [1–4]. Their sizes and applications range from miniaturized products for domestic use [5,6] to industrial scale applications for chemical energy storage [7–9]. Within the electrochemical cell design, a solid polymer electrolyte features the option to spatially separate both half-cells [10,11], permitting to deal safely even with consumed or evolving gaseous reactants.

Modified electrodes can be used in PEM water electrolyzers to enable anodic ozone evolution and *in situ* treatment of an anodic water feed [12–15] or in wastewater treatment [16,17]. These electrochemical cells contain a PEM as a solid polymer electrolyte onto which oppositely charged electrodes are firmly pressed, forming a membrane-electrode assembly (MEA) [12,18–21]. Water is supplied to both reaction compartments and electrolytically decomposed at the surfaces of the electrodes [18,22]. Anodically, water molecules are oxidized to both oxygen and ozone gas (eq. (1) and (2)) which can immediately dissolve in the surrounding electrolyte. The remaining protons are subsequently

transported through the PEM, discharged, and recombine at the cathode surface to form hydrogen gas (eq. (3)). As the anodic formation of O_2 during PEM water electrolysis is thermo-dynamically preferential, significant amounts of O_3 can only be generated when a specific catalytically active anode surface with a high overpotential for O_2 evolution is chosen (e.g. $\beta\text{-PbO}_2$) [23].

Anode:



Cathode:



Within the cell the current is transported by ionic conduction in the solid polymer electrolyte, which most often consists of a Nafion™ membrane [24,25]. Following the cluster-network model, initially proposed by Hsu and Gierke, the Nafion™ bulk material consists of a

* Corresponding author.

E-mail address: roman.grimmig@h-brs.de (R. Grimmig).

<https://doi.org/10.1016/j.seppur.2022.121063>

Received 27 January 2022; Received in revised form 27 March 2022; Accepted 10 April 2022

Available online 11 April 2022

1383-5866/© 2022 The Author(s). Published by Elsevier B.V. This is an open access article under the CC BY license (<http://creativecommons.org/licenses/by/4.0/>).

hydrophobic PFSA backbone and functional sulfonate groups, which self-organize to form hydrophilic spheres (inverted micelles) of about 4 nm in diameter, connected by cylindrical channels of about 1 nm in diameter [26,27]. All mass transport through the PEM occurs within these ion channels [28,29]. As a result of the large number of sulfonate side-groups in its chemical structure, Nafion™ shows a selective permeability to cationic species, while anions are not actively transported due to Donnan exclusion [24,30] and thus acts as an ion-selective barrier.

Previously, the transport of water, gases and ions in PEM cells has been characterised during the operation of fuel cells [31–33], redox flow batteries [34–36] and chlor-alkali electrolysis [37]. However, in recent literature, these phenomena are mostly investigated by means of simulation studies only. All mass transport processes occurring in PFSA membranes strongly depend on local and global membrane properties, as e.g. the polymer structure or hydration state of the membrane [38]. As described by the Nernst-Planck model [39,40], the overall ion transport is mainly comprised of two superimposed mechanisms, schematically depicted in Fig. 1: Diffusion (Fig. 1(a)) through the membrane via ion exchange (for H^+ also referred to as “proton hopping” or Grotthuss mechanism) and additional ion migration (Fig. 1(b)) induced by the electric field gradient across the membrane [28,41]. In operation, both these driving forces act upon all permeating ions.

As tap water contains additional charge carriers, such as mono- and bivalent cations (Na^+ , K^+ , Ca^{2+} , Mg^{2+}), they may equally be transported through the membrane due to their physicochemical properties and the electric field applied during electrolysis [32,33,42]. However, strong interactions between these cations and the sulfonate groups in the membrane may prevent a regular vehicular transport if the membrane exhibits a low local water content. This state then leads to a different “hopping” mechanism being more related to site-to-site hopping processes as observed in solids [43]. Nevertheless, as the membrane is continuously exposed to water on both sides, an insufficient hydration state can be considered unlikely when dealing with a PEM water electrolyser.

Despite dragging water electro-osmotically across the membrane into the catholytic compartment [24,30,44], this permeation behaviour leads to an accumulation of ions in the catholyte and ultimately results in the formation of precipitates, impairing the performance of both membrane and electrodes. As the long-term stability of the PEM electrolyser depends on the elemental composition of the supplying water, the application of this technology has been limited to the *in situ* ozonation of ultrapure water distribution systems only.

Therefore, this study covers the permeation behaviour of both water and the four most abundant cations in tap water within an ozone-

evolving PEM electrolyser under different operation conditions to account for different water feed qualities and demands for disinfection. Special emphasis is put on the unique characteristics during the batch-like operation in stagnant water supplies and its relations to pH environment, precipitation formation and constructional mitigation of ion permeation. As a result, preferential operational modes to enhance the long-term stability of such a sanitization device are identified and amended by physicochemical parameters which can be directly used for scaled-up applications.

2. Materials and methods

To investigate both ion and water permeation during the operation of a PEM tap water electrolyser, the setup depicted in Fig. 2 was used for all experiments. Within a PVC housing a hexagonally arranged structured membrane-electrode assembly (SMEA) is mounted, consisting of up to seven pairs of PbO_2 -coated porous titanium anodes ($A_{geo} = 0.2 \text{ cm}^2$ per electrode) and porous titanium cathodes (all Innovatec Gerätetechnik GmbH, Rheinbach, Germany). Individual water supplies for each half-cell allow for an independent study of both the cathodic and anodic water cycle, separated by a Nafion™ 117 membrane (DuPont, Wilmington, Delaware, USA) as PEM material (total membrane area exposed to solution: $A_{geo} = 33.2 \text{ cm}^2$). For experiments with technical suppression of permeation an additional titanium auxiliary cathode was placed inside the anolytic compartment and electrically connected to the other cathodes placed in the catholytic compartment. Due to a PTFE spacer only the SMEA array of electrodes is in direct contact with the PEM.

The compositions for synthetic tap water samples for anolytic circulation are demonstrated in Table 1 and account for different levels of water hardness. All solutions were prepared in accordance with the German Detergents and Cleaning Products Act (German designation WRMG [45]) using p.a. grade $NaCl$, $MgCl_2 \cdot 6 H_2O$ (both Carl Roth, Karlsruhe, Germany), KCl , $CaCl_2 \cdot 2 H_2O$ (both Merck, Darmstadt, Germany) and $18.2 \text{ M}\Omega$ ultrapure water using ELGA Purelab Flex (VWS, High Wycombe, UK).

To avoid precipitation within the catholytic water cycle, a 100 mmol L^{-1} HAc / NH_4Ac buffer system ($pH = 4.7$) (Carl Roth, Karlsruhe, Germany) was used. Before every experiment, the PEM was regenerated without electrodes and converted to its H^+ form by boiling it in 1 mol L^{-1} H_2SO_4 (Carl Roth, Karlsruhe, Germany) for 1 h and equilibrated in deionized water.

Standard operation parameters of the electrolysis cell were set to a current density of 1.00 A cm^{-2} , referring to a geometric anode surface of 1.4 cm^2 , medium water as the anolyte and 8 h of operation. For the

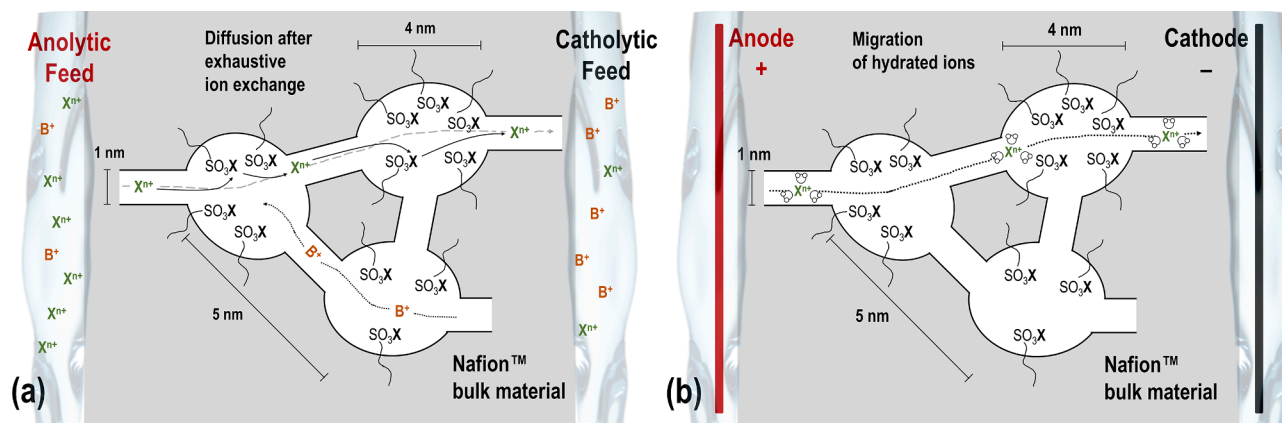


Fig. 1. (a) Diffusive ion transport via dynamic ion exchange driven by a concentration gradient. With no current applied, diffusing ions (X^{n+}) have to be compensated by back-diffusion of buffer ions (B^+) to maintain electroneutrality. After reaching ion exchange equilibrium, all SO_3 groups are associated with X^{n+} ions. Further permeating ions experience a dynamic exchange and pass the membrane through ion channels. (b) Migration through the membrane by vehicular transport. In the electric field, hydrated ions cross the PEM towards the anode. Own drawing, adapted from [27].

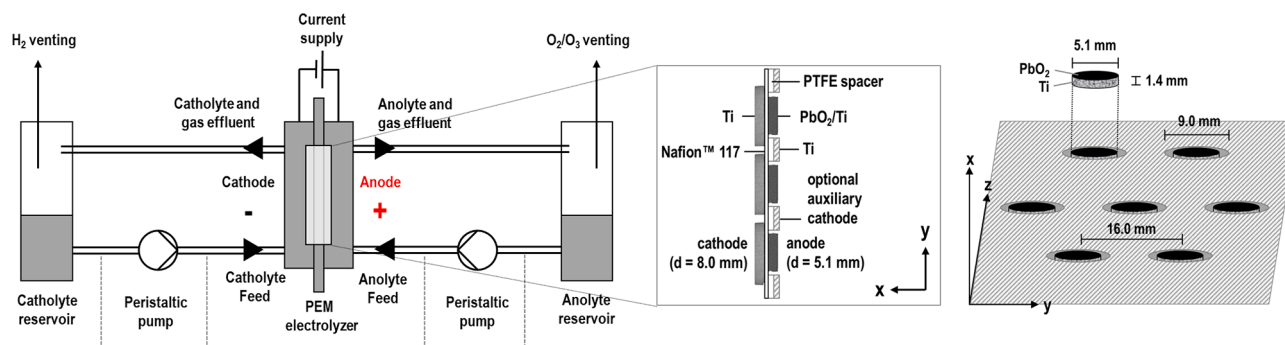


Fig. 2. Scheme of the experimental setup (left) and arrangement of the SMEA (right). Synthetic tap water from the reservoir is pumped through the anodic half-cell of the PEM electrolyser, with ions permeating into the buffered cathodic water cycle. For selected operation modes, the electrolyser can be equipped with an auxiliary cathode in the analytical compartment.

Table 1

Composition of synthetic tap water samples with varying cation concentrations used for permeation experiments, given as mass concentrations β_{ion} and equivalent concentrations $c_{\text{ion, eq}}$ (expressed in milliequivalents (mEq) per litre) as well as molar equivalent fractions $x_{\text{ion, eq}}$.

Water hardness level	soft		medium		hard		$x_{\text{ion, eq}}$ / %
	β_{ion} / mg L ⁻¹	$c_{\text{ion, eq}}$ / mEq L ⁻¹	β_{ion} / mg L ⁻¹	$c_{\text{ion, eq}}$ / mEq L ⁻¹	β_{ion} / mg L ⁻¹	$c_{\text{ion, eq}}$ / mEq L ⁻¹	
Na ⁺	20.0	0.87	40.0	1.74	80.0	3.48	24.2
K ⁺	2.5	0.06	5.0	0.13	10.0	0.26	1.8
Mg ²⁺	8.0	0.66	16.0	1.32	32.0	2.63	18.3
Ca ²⁺	40.0	2.00	80.0	3.99	160.0	7.98	55.6
Σ	70.5	3.59	141.0	7.18	282.0	14.35	100.0

aforementioned water hardness levels, permeation during electrolysis was observed for current densities applied from 0.25 to 1.25 A cm⁻² (denoted “powered operation”). In order to simulate a typical stand-by operation in a low-power mode, an additional level of 0.01 A cm⁻² (for anodic protection of the catalytically active PbO₂ layer) was evaluated.

After defined time intervals, 5 mL of the catholyte were sampled for subsequent quantification of permeated ions, which was carried out using an ARCOS ICP-OES system (Spectro, Kleve, Germany) in radial configuration, equipped with a standard Scott spray chamber, a cross-flow nebulizer and certified elemental standards (Carl Roth, Karlsruhe, Germany). Operation conditions for ICP-OES measurements are listed in Table 2.

Water permeation was quantified gravimetrically using a Ranger 3000 balance (Ohaus, Parsippany, New Jersey, USA) with a data acquisition rate of 6 Hz.

During pH experiments both the anolytic and catholytic compartments were continuously purged with Argon 4.8 gas (Westfalen AG, Münster, Germany) at 30 mL min⁻¹ to minimize atmospheric influences within the open setup.

Non-buffered long-term experiments related to the investigation of scale formation were carried out applying a current density of 1.00 A

Table 2

Operation conditions for ICP-OES measurements in radial configuration.

Parameter	
Incident power / W	1,400
Cooling gas flow rate / L min ⁻¹	13.0
Auxiliary gas flow rate / L min ⁻¹	1.5
Nebulizer gas flow rate / L min ⁻¹	0.70
Rinse time / s	60
Integration time / s	12
Number of replicates	4

cm⁻² and using hard model water prepared as stated above. Experiments were conducted for 500 operating hours before disassembly and subsequent analysis.

X-ray diffraction (XRD) analysis and characterisation of scale particles were carried out on a D2 PHASER diffractometer and using TOPAS 5.0 software (both Bruker, Billerica, Massachusetts, USA). Analyses were performed at U = 30 kV and I = 10 mA within a 2 θ range from 5° to 65° using a Cu-K α radiation source ($\lambda = 1.54 \text{ \AA}$).

For identification of the cathodic surface composition, an X-Supreme 8000 (Oxford Instruments, Abingdon, United Kingdom) X-ray fluorescence (XRF) spectrometer was used at U = 15 kV, I = 10 μ A and 180 s integration time.

The spatial distribution of characteristic elements on the cathode surfaces was determined using a JEOL 7200F field-emission scanning electron microscope (SEM) at U = 10 kV. Corresponding elemental mapping analyses were obtained using a Bruker XFlash® 6|60 EDX detector.

3. Results and discussion

3.1. Water transport within a PEM electrolyser

During the operation of a PEM electrolyser in water, positive charge carriers are transported from the anolytic to the catholytic compartment through the PEM. As cations in aqueous solution are present in hydrated form, the ion transport is accompanied by an electro-osmotic flow of water, i.e. an increase of the water volume within the catholytic compartment. Fig. 3(a) shows that the amount of permeated water $n_{\text{H}_2\text{O}}$ increases linearly ($R^2 > 0.99$ for $J > 0.25 \text{ A cm}^{-2}$, $R^2 = 0.95$ for $J = 0.25 \text{ A cm}^{-2}$) with the operating time of the electrolyser. While no significant water permeation was measured in stand-by operation, a raise in current density is directly accompanied by increased levels of permeating water. This observation strongly suggests that substantial water transport is occurring predominantly due to ion migration and electro-osmosis between the electrodes. With a higher current density, more charge carriers are produced and transported per unit time, thus leading to an expedited increase in catholytic water volume.

By linear regression of $n_{\text{H}_2\text{O}}$ in Fig. 3(a) water permeation rates $\dot{n}_{\text{H}_2\text{O}}$ can be obtained to quantify the occurring electro-osmotic drag. The data given in Table 3 yield an excellent fit to a linear function to describe the observed correlation. Thereof, the change in water permeation rate was determined to $95 \pm 2 \text{ mmol A}^{-1}\text{h}^{-1}$ and indicates that the amount of permeating water does not depend on the size of the contacted electrode surface area but is merely proportional to the experimental time and current flow within the PEM electrolyser. However, smaller variations in water transport may also result from the state of the Nafion™ membrane, as the electro-osmotic drag (EOD) coefficient is influenced by local hydration state, even under fully hydrated conditions at comparable temperatures [46].

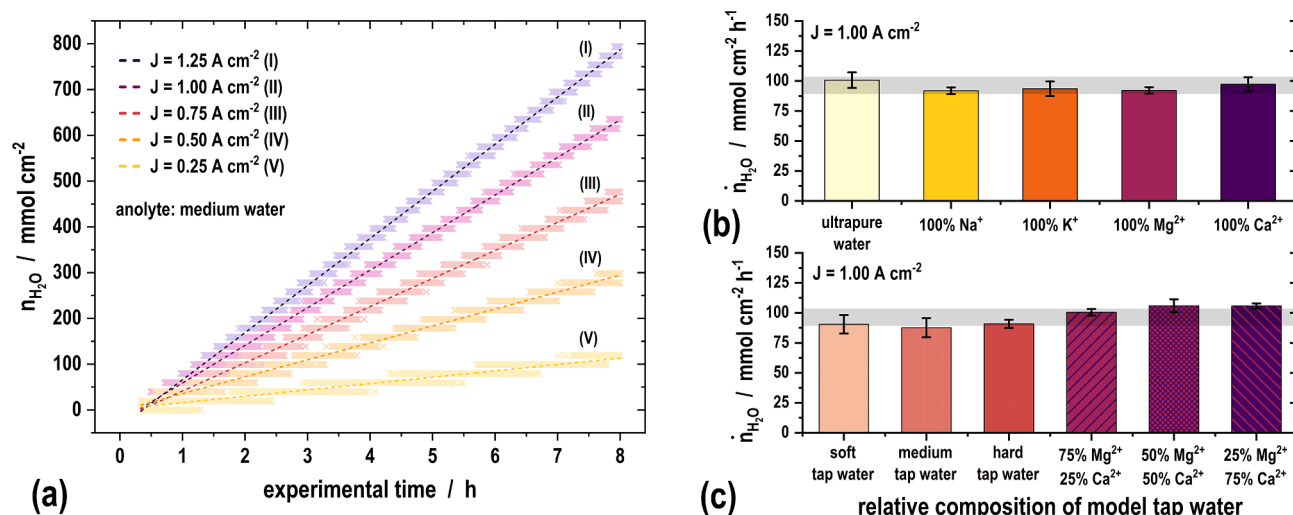


Fig. 3. (a) Cumulated amount of permeated water n_{H_2O} during representative experiments for different current density levels. A linear increase in water permeation can be observed with progressing experimental time and elevating current density. Measured data points form a step profile due to limitations by the balance resolution of 0.5 g (corresponding to 28 mmol H₂O). (b) Water permeation rates \dot{n}_{H_2O} for experiments with varying relative ion composition but equal cationic strength. (c) Permeation rates for different Mg²⁺ and Ca²⁺ containing mixtures as well as different water hardness levels representing varying equivalent concentrations. No significant deviation from an average value of 96 ± 5 mmol cm⁻² h⁻¹ is observed for anolytic feed waters with individual ion species, mixtures of different elements or even differing water hardness levels.

Table 3

Water permeation rates \dot{n}_{H_2O} and total ion permeation rates $\sum \dot{n}_{ion, eq}$ for all current densities under investigation.

$J / A\ cm^{-2}$		0.01	0.25	0.50	0.75	1.00	1.25	R ²
$\dot{n}_{H_2O} / mmol\ cm^{-2}\ h^{-1}$		0.0 ± 2.5	14.0 ± 2.5	37.1 ± 3.1	61.4 ± 2.5	87.6 ± 7.9	107.2 ± 7.8	0.9948
$\sum \dot{n}_{ion, eq} / \mu Eq\ cm^{-2}\ h^{-1}$	soft	4.0 ± 0.1	7.6 ± 0.2	8.0 ± 0.4	8.0 ± 0.3	10.0 ± 0.3	10.4 ± 0.3	0.8471
	medium	7.0 ± 0.1	11.0 ± 0.2	14.3 ± 0.3	16.5 ± 0.2	16.4 ± 0.3	20.9 ± 0.3	0.9408
	hard	13.2 ± 0.2	24.5 ± 0.5	27.1 ± 0.3	31.4 ± 0.9	40.1 ± 1.2	43.5 ± 1.1	0.9644

As the electrical charge can only be transported across the membrane by cationic species, the occurring mass transport behaviour must be ascertained for different cation compositions in order to reliably establish this technique for tap water disinfection in regions with diverging levels of water hardness. Fig. 3(b) allows for a comparison of \dot{n}_{H_2O} for anolyte feeds of varying composition and indicates that no significant differences in water permeation are observed with all three water hardness levels under investigation. Consequently, \dot{n}_{H_2O} can be considered as a function independent of the total anolytic cation concentration.

Furthermore, Fig. 3(b) and (c) depict water permeation rates \dot{n}_{H_2O} which were determined for model waters of varying relative ion composition but with equal normality (equivalent concentrations), i.e. all solutions contained the same cationic strength of $7.18\ meq\ L^{-1}$, corresponding to medium tap water used in this study. This enables to identify whether certain elements contribute in particular to the water transport during the PEM operation as equal amounts of equivalents can be transported by permeating tap water cations (other than H⁺) present in the anolytic solutions. For a fixed current density level of $1.00\ A\ cm^{-2}$ maintained in all experiments, no significant influence was observed when altering the anolytic composition to individual monovalent or bivalent ion species or systematic mixtures thereof. In contrast, previous studies have found considerable differences in the amount of water transported with each permeating charge carrier when the PFSA membrane had been pre-exchanged with different alkali cations before use [47,48]. As a tap water electrolyser makes use of an H⁺ form NafionTM membrane in dilute ion solutions, only a partial exchange with tap water cations will take place. Hence, the influence of the state of the membrane is minimized and therefore of minor relevance for the application. Thus, the relative composition of the anolytic feed water appears to be of no significance for the water permeation and can be expected to hold

also true for further ions beyond the scope of this study. Hence, the water permeation rates \dot{n}_{H_2O} for all experiments with standard operation at $J = 1.00\ A\ cm^{-2}$ were averaged and yielded a mean value of $96 \pm 5\ mmol\ cm^{-2}\ h^{-1}$, which is in perfect accordance with the findings obtained from Fig. 3(a).

The observed water flux can further be expressed as a net EOD coefficient for each transported charge carrier during cell operation. The obtained mean value of 2.55 ± 0.05 molecules H₂O per charge carrier is in accordance with literature data for various fuel cell and water electrolysis applications which typically range from 2.5 to 2.9 when using fully hydrated NafionTM 117 membranes [46,49,50]. The common interpretation of an EOD > 1 suggests that the transport of water and ions occurs via a vehicular mechanism, meaning that fast-moving ions drag their hydration sphere into the catholyte. As has been previously reported, proton hopping or related structural diffusion phenomena do not allow for a net transport of water [51]. Following these implications, it is suggested that diffusive processes do not contribute to water transport under electrolysis conditions. Nonetheless, the correlation of the EOD coefficient with distinct transport phenomena is dealt with controversially in the literature [38,52,53].

3.2. Ion diffusion and migration during powered and stand-by operation

For the investigation into the permeation behaviour of the cationic species, ICP OES measurements were conducted to determine shifting ion concentrations within the catholyte. In order to assess the reliability of the so-obtained data in a first step, all selected methods were examined with respect to the analytical performance of the conducted calibrations. Therefore, limits of detection (LOD) and quantification (LOQ), linearity, precision and accuracy were evaluated for all elements of

interest (see [supplementary table A.1](#) in the appendix).

For most of the observed elements, calibrations yield LOD values below $40 \mu\text{g L}^{-1}$, with a minimal value of $11.9 \mu\text{g L}^{-1}$ for Ca. Given that all relevant components can be quantified to trace levels of less than 0.25 mg L^{-1} , confident monitoring of ion migration and diffusion during PEM electrolyser operation is possible. The obtained values for LOD and LOQ are in the same order of magnitude as reported in previous works [54,55], confirming that the chosen methodology is not limiting the analyses of the datasets.

Apart from that, all calibrations were fitted to linear functions with coefficients of determination $R^2 \geq 0.9996$ and precision coefficients of less than 4%. With this method, artificial samples differing in analyte concentrations of merely 0.1 mg L^{-1} can be significantly distinguished.

In a first approach, the obtained ICP OES data enables quantifying the cationic permeation behaviour during standard electrolysis operation in medium tap water, which is depicted in [Fig. 4\(a\)](#). Herein, the molar concentrations of all four observed cations are depicted and illustrate a strictly monotonous increase with experimental time. Notably, the transport behaviour is sufficiently linear for all analytes ($R^2 > 0.995$) within the observed timeframe. As a consequence of the original composition of the analytic model water, the obtained regression functions for different cationic species deviate significantly in their slope values. Exemplarily, the full dataset for medium water hardness and a current density of 1.00 A cm^{-2} is depicted in [Fig. A.1](#) the appendix.

In order to identify trends in transport selectivity through the PEM in [Fig. 4\(b\)](#), the calculated ion permeation rates were normalized by the original molar fractions within the anolyte. The so-obtained values correspond to expected total ion permeation rates if all cations were of one distinct species. It can be seen that transport rates increase significantly for elevated ion concentrations, i.e. increased levels of water hardness. For an ideal limiting current regime, transport is unselective as all ions reaching the anode/PEM interface immediately permeate through the membrane. In the present study, the observations for medium and soft water show that ion selectivities of Na^+ , Mg^{2+} , Ca^{2+} are in a comparable order of magnitude whereas K^+ shows an increased permeability. Even further, for a hard model water, a 15.8% increased permeability of K^+ could be determined while the permeability of Na^+ decreased by 11.6%. To further assess whether these trends in relative

ion transport are consistent throughout all water hardness levels, ion permeation rates have also been normalized by their initial equivalent concentrations $c_{\text{ion, eq}}$ in the anolyte (see [Table 1](#)) and averaged for all investigated water hardness levels. Comparing these permeation values to the respective ion mobility in aqueous media ([Fig. 4\(c\)](#), reference values derived from [56]), a considerable congruence can be noted, when ion concentrations are sufficiently high to unveil significant deviations. This may be a direct consequence of concentration polarization, which causes a local depletion of tap water abundant ions at the PEM/anode interface. When ions from the bulk anolyte diffuse towards the interface, they are discriminated by their respective ion mobility in water.

In consequence, the ion transport selectivity appears to be caused by both the ion mobility in water and the composition of the anolytic feed. Thus, the transfer of ions in water to the anode/PEM interface limits the ion permeation under the given operation conditions in tap water.

To approximate the correlation of water and ion permeation via diffusion and migration respectively, the occurring mass transport behaviour was measured at different current density levels, with the corresponding permeation rates given in [Table 3](#).

Both water and ion permeation increase when a higher current density is applied. However, when characterizing the relationship by a linear function, it becomes obvious that for water transport a satisfying correlation can be drawn ($R^2 = 0.9948$) while this is only partially given for ion permeation. With increasing water hardness, R^2 improves from 0.85 to 0.96, referring to an increasingly linear relationship between ion permeation and current density. While water permeation only occurs during powered operation ($J \geq 0.25 \text{ A cm}^{-2}$), i.e. when ion transport is also subject to migration, a significant ion transport can be also observed during stand-by operation ($J = 0.01 \text{ A cm}^{-2}$). In this operational mode, a possible water transport by diffusion across the entire PEM surface could not be observed within the experimental limitations and must therefore be smaller than $105 \mu\text{mol H}_2\text{O h}^{-1} \text{ cm}^{-2}$. Hence, water transport appears to be predominantly mediated by migration and not by structural diffusion, in contrast to the joint mechanism model for ion permeation.

In stand-by operation, ions from the anolytic compartment infiltrate the PEM mainly by slow diffusive processes and occasionally get exchanged at the SO_3 groups within the membrane, gradually

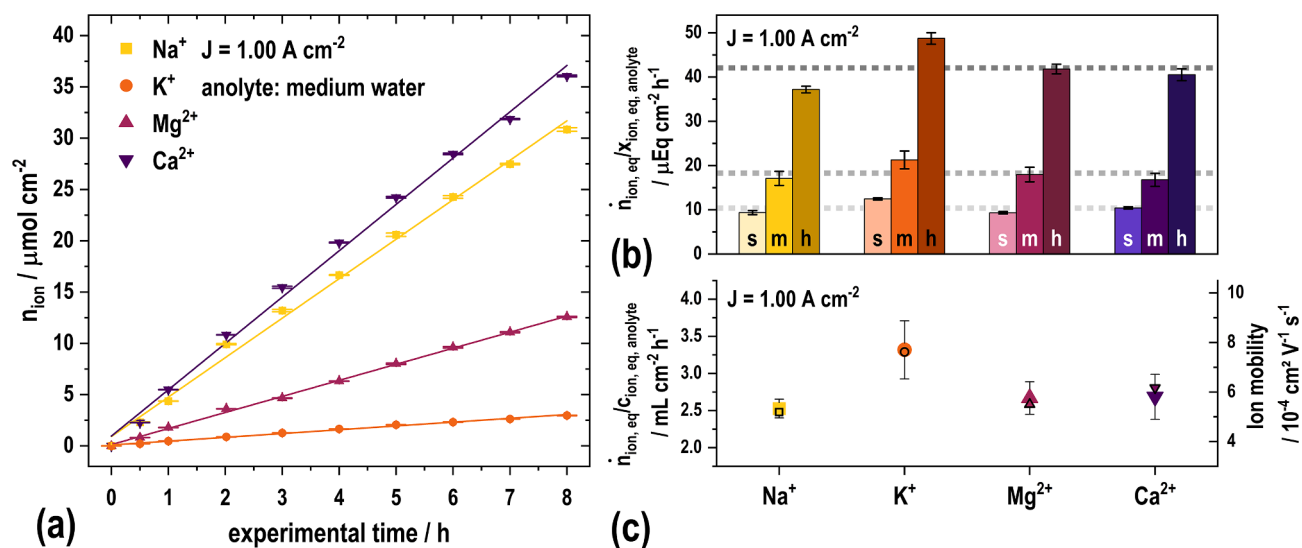


Fig. 4. (a) Observed amounts of mono- and bivalent ions, transported from anolytic tap water to the catholytic loop of the PEM electrolyser setup. During electrolysis, a linear transport of all ions can be observed. Corrections for permeation-induced dilution and sampling have been applied. (b) Ion transport rates normalized by their molar fractions $x_{\text{ion, eq}}$ (see [Table 1](#)) under standard conditions. With increasing water hardness, more tap water cations are transported per time unit. While for medium and soft water hardness transport appears quasi-unselective, a more obvious discrimination can be observed for hard tap water, where K^+ is preferably transported by approx. 15% over the average transportation rates (dashed lines). (c) Ion transport rates normalized by their initial concentration in the anolyte under standard conditions. For all water hardness levels, the ionic permeation trends (left axis) can be related to their respective ion mobility in water (values derived from [56], right axis).

converting it from its initially charged H^+ -form to its X^{n+} -form. Once the ion exchange capacity of the membrane is exhausted [57,58], further ions get transported to the catholyte by diffusion. This is a direct consequence of using a highly concentrated buffer solution as a catholyte causing a concentration gradient across the membrane. Furthermore, when a low current is present, a superimposed migration process occurs, attractive electrostatic forces act upon the charge carriers and drag them towards the anode. By increasing the current density in powered operation, this mechanism becomes dominant.

In the observed time frame, a successive ion exchange of the membrane is represented by an attenuated ion cross-over from the anolytic to the catholytic compartment. The overall ion transport is compensated by buffer cations permeating into the anolytic compartment due to back-diffusion. As the ion exchange capacity of the PEM is limited for the given geometry, it can easily be exhausted by high ion concentrations in hard water. In order to evaluate ion diffusion, it is thus indicated to compare the powered and stand-by operation of the PEM electrolyser (see Fig. 5).

As previously indicated in Fig. 4(a) for all four ions under investigation, the total ion transport depicted in Fig. 5(a) shows an approximate linear correlation (all $R^2 > 0.99$) with experimental time, independent of water hardness. However, a different picture can be drawn when the stand-by operation is closely looked at (Fig. 5(b)). We observe a delayed onset of the ion transport which differs dramatically from the ideal linear behaviour, especially for soft and medium water. This can be recognized most prominently for magnesium, as e.g. in soft water this ion species could only be detected in the catholyte after 4 h have passed. Its breakthrough time decreases with increasing water hardness level, indicating a successive ion exchange of the PEM. In the case of hard water, these effects are barely noticeable as the retardation time is limited to a minimum, thus allowing to describe the overall ion permeation process by a linear function, analogous to powered operation.

The retarded onset in stand-by operation might be due to a more stable Mg^{2+} -NafionTM interaction caused by the hydration sphere of the elements involved [59,60], hence leading to a delayed transport through the PEM. For the given geometry, the ion exchange capacity of the PEM equals 1.22 mEq [61], which offers sufficient capacities to temporarily delay Mg^{2+} diffusion. However, this effect becomes negligible under electrolysis conditions.

3.3. Batch-like operation in stagnant feed water

In various applications, pipe systems for tap water are not regularly flushed and are consequently prone to the formation and accumulation of pathogens which may pose a potential health threat [62,63]. To draw potable water on demand at any given point, it is necessary to continuously sanitize stagnant water storage or line systems. This corresponds to a batch-like treatment of defined water volumes which can be performed using an ozone-evolving PEM electrolyser setup as presented in this study.

Since the transport of hydrated cations leads to an increase in water volume of the catholyte, it is necessary to characterise the influence of the responsible charge carriers. When operating a PEM electrolyser in tap water, a rapid change in pH value of both catholyte and anolyte can be noted (see Fig. 6), which affects the SMEA performance [64,65]. After only 2 h of operation in a closed system, the anolytic pH value has dropped below 3 while the pH value of the catholyte has increased to 10. When a buffer is used in the catholytic compartment, the pH value of the catholyte remains constant during both stand-by and powered operation as long as the buffer capacity is sufficient.

During powered operation the cathodic H_2 evolution is supplied by protons permeating from the anolytic compartment through the PEM. However, if an insufficient amount of H^+ ions is transported due to the presence of additional charge carriers (e.g. Na^+), the equivalent shortage in protons is overcome by additional cathodic water splitting, leading to an accumulation of OH^- anions in the catholyte.

In an open system, ultrapure water slowly acidifies due to successive CO_2 dissolution which was partially reduced by argon purging. In stand-by operation, this could be observed for both anolyte and catholyte. However, once the electrolyser is in powered operation, this effect becomes negligible as the change in pH value increases dramatically due to additional ion permeation.

Comparing stand-by and powered operation, it can be noted that the total ion permeation differs by a much lower quantity than expected for a 100-times increased current density. Considering the aforementioned concentration gradient in the present setup, it is indicated that diffusion is the dominating process at low current densities. Transported cations diffusing from the membrane into the catholyte will exchange with available positive charge carriers across the entire PEM surface. While in buffered systems this can be due to (dissociating) buffer ions, ultrapure

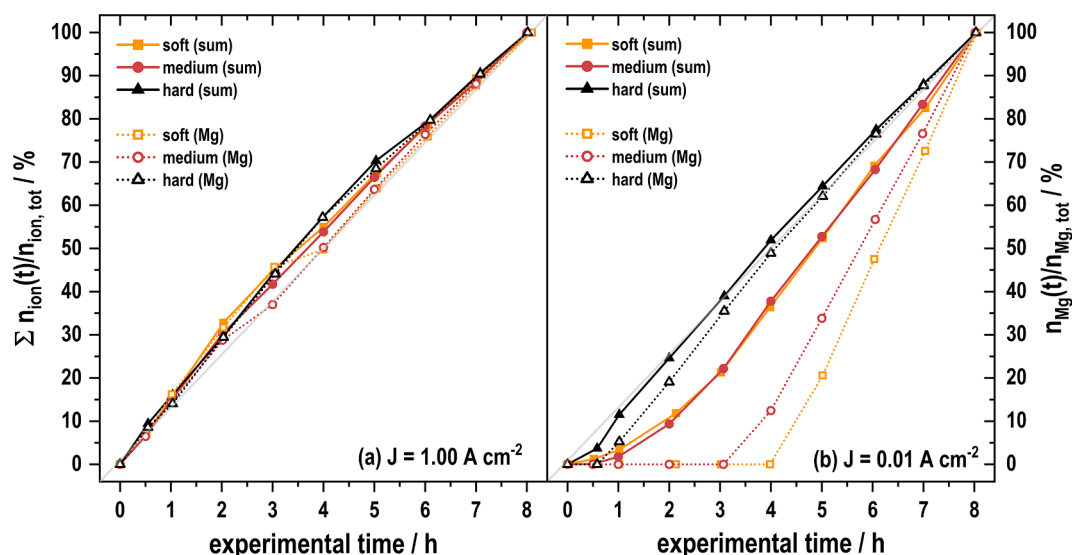


Fig. 5. Total ion transport as a function of the experimental time. Normalization has been performed regarding the total ion concentration after 8 h of the respective experiments to allow for an identification of ion discrimination. (a) During powered operation of the electrolyser, a linear transport behaviour can be observed independent of water hardness. (b) In contrast to that, during stand-by operation, the total ion transport from the anolytic to the catholytic compartment is delayed. This is especially prominent for magnesium, which is held back for shorter periods of time with increasing water hardness levels (dotted lines).

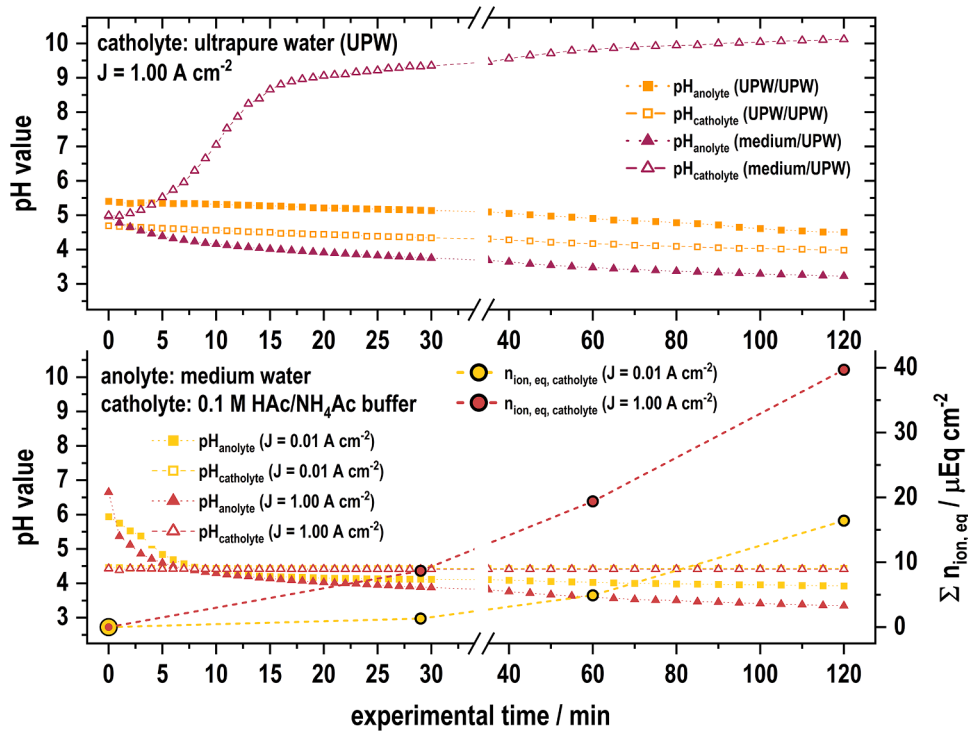


Fig. 6. During electrolysis, the pH values within the anolytic and catholytic compartments diverge adversatively from their respective starting values when charge carriers apart from protons in ultrapure water (UPW) are present in tap water (top). When using a catholytically buffered system and medium water, an analytical acidification is observed in both electrolysis and stand-by operation (bottom). In addition, ion permeation can be observed in both experiments.

water requires proton liberation, i.e. by autoprotolysis.

So far it has been shown that the permeation of ions occurs during both powered and stand-by operation of a PEM electrolyser with the given setup. Yet, the transport of any charge carrier apart from H^+ through the PEM (denoted $\sum n_{ion,eq}$ for Na^+ , K^+ , Mg^{2+} and Ca^{2+}) leads to a loss in H^+ transport effectiveness, represented by its current share χ_{H^+} (eq. (4)) [66,67]. In operation, a value close to 100% is desired as this means that only a minimal amount of hardeners is transported across the PEM, influencing both the pH value and the active surface area of the electrodes.

$$\chi_{H^+} = 1 - \left(\frac{\sum n_{ion,eq} \cdot F}{I \cdot t} \right) \quad (4)$$

For all water hardness levels and current densities in powered operation, the observed current shares are depicted in Fig. 7.

Even in hard tap water, protons constitute the vast majority of ionic conductors due to their anodic generation according to eq. (1) and (2). This justifies the previous observations in section 3.1 that no significant influence of different charge carriers on water transport was found. It becomes apparent that with increasing current density, the current share for H^+ transport approaches a maximum close to 100% which would equal an ideal electrolyte. The most efficient operation setting could be observed for soft water applying the highest current density $J = 1.25 \text{ A cm}^{-2}$ with a current share of $99.4 \pm 0.1\%$. In contrast to that, when applying low current densities and using hard water, the permeation-induced loss in χ_{H^+} led to values of only $93.5 \pm 0.4\%$. The data shows that the effect of actual water hardness can partially be compensated by increasing the current density.

3.4. Formation of precipitates and mitigation of ion permeation

If a PEM tap water electrolyser is operated in a non-buffered system, the observed pH gradient is accompanied by permeation of tap water cations, which infiltrate the catholyte and are likely to form insoluble compounds under the developing alkaline conditions. In Fig. 8 the

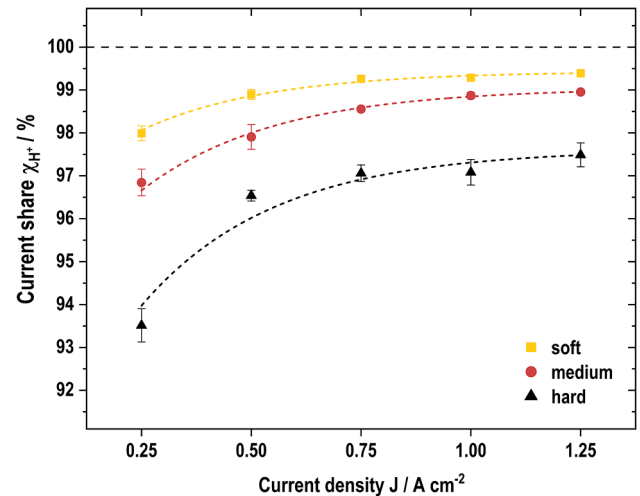


Fig. 7. H^+ transport-related current share χ_{H^+} of the electrolysis cell for different current densities and water hardness levels. When hard water is used, permeating ions affect the current share the most. The application of high currents partially compensates for that effect.

catholytic formation of precipitates during long-term operation is depicted.

Before electrolysis operation in tap water, the freshly installed titanium electrodes (Fig. 8(a)) show a shiny, porous surface without any visual contaminations, which is confirmed by EDX measurements. After 500 h of operation in hard water, the electrodes are covered with a white coating (Fig. 8(b)) which could not be observed during buffered operation. For post-operational investigations, the electrodes were recollected and reveal that the layer of scale (Fig. 8(c)) contains both magnesium and calcium, with the latter being found predominantly on the outer regions of the electrode. As the oppositely positioned anodes

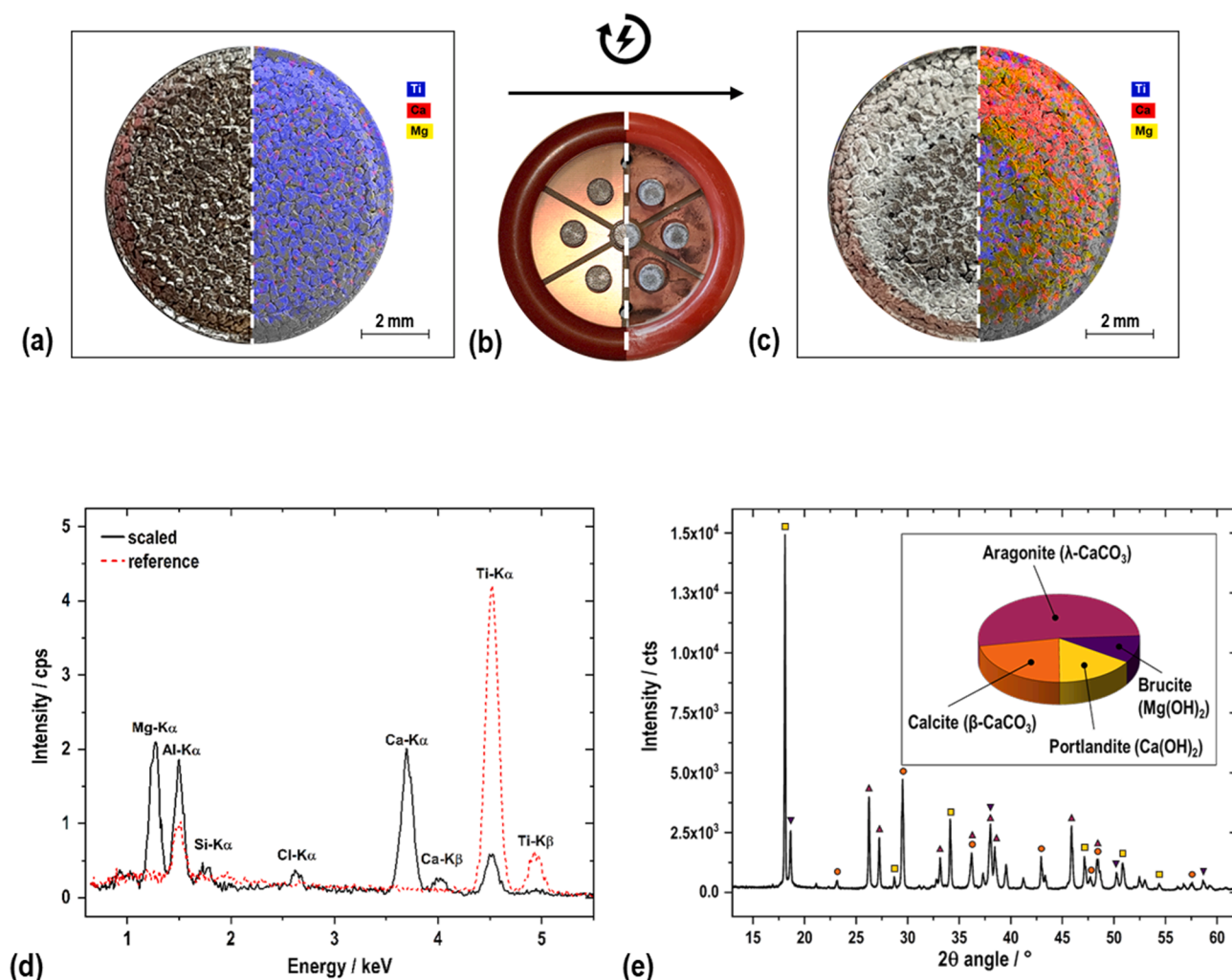


Fig. 8. (a) Top view on the cathodic PEM contacting site **before** its usage in the electrolyser (non-buffered operation). Optical imaging (left) and SEM-EDX elemental mapping (right) show the absence of scaling. (b) Pre- (left) and post-operation (right), the catholytic compartment shows significant build-up of scale on the cathodes. (c) Top view on the cathodic PEM contacting site **after** its usage in the electrolyser (non-buffered operation). Optical imaging (left) and SEM-EDX elemental mapping (right) show the presence of scaling and enrichment of calcium and magnesium in areas affected by scaling. (d) XRF spectra of the pre- (red dashed lines) and post-operational (solid black line) cathodes. Signals related to the elements of interest are highlighted. (e) Diffraction pattern of the cathodic scale with signals assigned to the identified crystalline phases (\blacktriangle = Aragonite, β -CaCO $_3$; \bullet = Calcite, λ -CaCO $_3$; \blacksquare = Portlandite, Ca(OH) $_2$; \blacktriangledown = Brucite, Mg(OH) $_2$). The detail picture illustrates the relative scale composition.

are smaller in diameter, there is a defined center region where both the electric field as well as the ionic flux are expected to be the highest and where titanium signals are detected most prominently, hence indicating a nearly uncovered cathode surface. Scale formation and build-up between the cathode/PEM interface could result in a decreasingly available contact area, leading to higher local current densities which may eventually cause membrane stress and failure. A comparison of the pre- and post-operational XRF spectra of the cathodes (Fig. 8(d)) emphasizes the layered precipitate formation on the electrode surface, as titanium signals partially disappear whereas signals related to the hardeners emerge. XRD measurements (Fig. 8(e)) indicate that nearly all signals can be explained with the presence of hydroxides and carbonates of magnesium and calcium, namely Aragonite (β -CaCO $_3$), Calcite (λ -CaCO $_3$), Portlandite (Ca(OH) $_2$) and Brucite (Mg(OH) $_2$). An approximation of the relative composition was performed using Rietveld refinement [68]. As both detected calcium carbonate allotropes make up for roughly 75% of the scale, the absorption of CO $_2$ and subsequent dissolution and carbonatization in the catholyte under unbuffered conditions must be considered.

An approach to mitigate ion permeation is the introduction of an auxiliary cathode within the anolytic, ozone-evolving compartment. In

order to assess its influence, ion permeation is evaluated for experiments with the auxiliary cathode connected to and disconnected from negative potential (Fig. 9).

With the auxiliary cathode connected, a mean current of $I = 42 \pm 11$ mA could be measured between the anode and the auxiliary cathode, which equals $3 \pm 1\%$ of the total current applied. Using this modified operation mode, a decrease in total ion permeation of $18 \pm 4\%$ was found without preference for any cationic species involved. As the applied current remained unchanged, an equal amount of anodically produced ozone can be expected. At every point during the experiments, the total ion permeation was suppressed significantly as indicated by the summed-up permeation values that differ by their respective margins of error.

Consequently, the auxiliary cathode appears to introduce an electric field that is opposed to the field caused during powered operation of the PEM electrolyser. Ions are therefore less attracted to the anode/PEM interface and can be expected to cause a less prominent pH gradient across the membrane during batch-like operation, eventually leading to a reduced risk of precipitation in the catholytic compartment and thus increase the expected lifetime of the electrolyser setup.

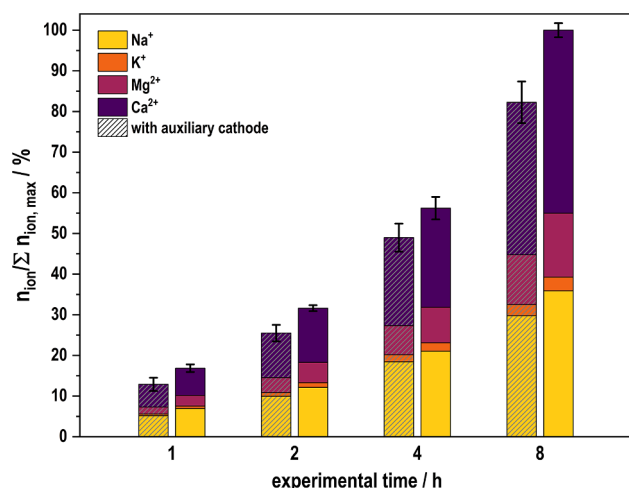


Fig. 9. Cumulated ion permeation as a function of the experimental time, normalized to its highest total value. Error bars referring to the summed-up ion permeation result from the propagation of uncertainty for each ion permeation involved. During both operational modes under standard conditions, ion permeation increases monotonously. A mean and indiscriminate permeation suppression of $18 \pm 4\%$ was determined.

4. Conclusion

In the present work, a specific PEM electrolyser setup for ozone evolution is characterised during its application as a tap water electrolyser. Both ion and water transport were modeled for different water hardness levels and current densities representing varying performance requirements for ozone evolution. During operation, a significant water transport of $95 \pm 2 \text{ mmol A}^{-1} \text{ h}^{-1}$ from the anolyte to the catholyte can be noticed which is directly proportionate to the applied current and needs to be considered for scaled-up applications. The water transport was found to be decoupled from the ion permeation. The latter also takes place in stand-by operation and increases with an elevated water hardness level of the anolytic feed as well as with current density. The transport of ions correlates with their ion mobility in water, leading to the conclusion that their transport to the anode/PEM interface is limited. Especially for a batch-like operation e.g. in a stagnant water, a high proton efficiency is desired and can be achieved by the application of increased current density. As carbonates make up for about 75% of the cathodic scale, the dosing of an acidic buffer is recommended to ensure long-term stability of the SMEA. Thus, this technique can be applied in regions with soft tap water, without requiring any further pre-processing of the water feed. However, as hard feed water is related to a higher risk of precipitations, the use of an upstream water softening unit can be recommended. Furthermore, an auxiliary cathode can be used to suppress ion permeation by nearly 20%.

The obtained models allow for a differentiated ion and water transport assessment during tap water electrolysis of any water quality. Future studies can improve by focusing on the influence of tap water ions on the efficiency of electrochemical ozone evolution and consider the anodic treatment of anions to allow for an even more comprehensive insight into tap water electrolysis employing a structured PEM electrolyser.

CRediT authorship contribution statement

Roman Grimmig: Conceptualization, Methodology, Formal analysis, Investigation, Data curation, Visualization, Writing – original draft. **Philipp Gillemot:** Conceptualization, Methodology, Formal analysis, Data curation, Visualization, Writing – original draft. **Samuel Stucki:** Conceptualization, Writing – review & editing. **Klaus Günther:** Supervision, Writing – review & editing. **Helmut Baltruschat:** Supervision,

Writing – review & editing. **Steffen Witzleben:** Funding acquisition, Resources, Supervision, Writing – review & editing.

Declaration of Competing Interest

The authors declare that they have no known competing financial interests or personal relationships that could have appeared to influence the work reported in this paper.

Acknowledgements

The authors gratefully acknowledge the support by Innovatec Gerätetechnik GmbH in providing materials and resources for PEM tap water electrolyser setups. In addition, we thank Amelia Heiner (Department of Material Science and Engineering, University of Utah, Salt Lake City, UT, USA) for proofreading.

Funding

This work was supported and financed by the Federal Ministry of Education and Research programs “KMU-Innovativ” project “OzonArray” (grant number: 02WQ1373B) and “FHprofUnt” project “ReDeX” (grant number: 13FH107PX8).

Conflicts of Interest

Samuel Stucki works as scientific consultant for Innovatec Gerätetechnik GmbH which provided resources for the present study. All other authors declare no conflict of interest.

Appendix A. Supplementary material

Supplementary data to this article can be found online at <https://doi.org/10.1016/j.seppur.2022.121063>.

References

- [1] S. Giancola, M. Zatoń, Á. Reyes-Carmona, M. Dupont, A. Donnadio, S. Cavaliere, J. Rozière, D.J. Jones, Composite short side chain PFSA membranes for PEM water electrolysis, *J. Memb. Sci.* 570–571 (2019) 69–76, <https://doi.org/10.1016/j.memsci.2018.09.063>.
- [2] N. Lüttem, A. Karouach, S. Tveitan, Thermo-economic study of waste heat recovery from condensing steam for hydrogen production by PEM electrolysis, *Energy Convers. Manag.* 185 (2019) 21–34, <https://doi.org/10.1016/j.enconman.2019.01.095>.
- [3] S. Grigoriev, V. Porembsky, V. Fateev, Pure hydrogen production by PEM electrolysis for hydrogen energy, *Int. J. Hydrogen Energy* 31 (2) (2006) 171–175, <https://doi.org/10.1016/j.ijhydene.2005.04.038>.
- [4] T. Lickert, M.L. Kiermaier, K. Bromberger, J. Ghinaiya, S. Metz, A. Fallisch, T. Smolinka, On the influence of the anodic porous transport layer on PEM electrolysis performance at high current densities, *Int. J. Hydrogen Energy* 45 (11) (2020) 6047–6058, <https://doi.org/10.1016/j.ijhydene.2019.12.204>.
- [5] N. Hermes, G. Knupp, Transformation of atrazine, bisphenol A and chlorendic acid by electrochemically produced oxidants using a lead dioxide electrode, *Environ. Sci. Water Res. Technol.* 1 (6) (2015) 905–912.
- [6] J. Wenk, G.A. Zoumpoulis, J.Y.M. Chew, Ozonation in the Framework of Sustainable Future Water Management, in: *Front. Water-Energy-Nexus—Nature-Based Solut. Adv. Technol. Best Pract. Environ. Sustain.*, Royal Society of Chemistry, 2019, pp. 99–102, https://doi.org/10.1007/978-3-030-13068-8_24.
- [7] J.M. Stansberry, J. Brouwer, Experimental dynamic dispatch of a 60 kW proton exchange membrane electrolyzer in power-to-gas application, *Int. J. Hydrogen Energy* 45 (2020) 9305–9316, <https://doi.org/10.1016/j.ijhydene.2020.01.228>.
- [8] S. Stucki, G.G. Scherer, S. Schlagowski, E. Fischer, PEM water electrolyzers: evidence for membrane failure in 100 kW demonstration plants, *J. Appl. Electrochem.* 28 (1998) 1041–1049, <https://doi.org/10.1023/A:1003477305336>.
- [9] M. Espinosa-López, C. Darras, P. Poggi, R. Glises, P. Baucour, A. Rakotondrainibe, S. Besse, P. Serre-Combe, Modelling and experimental validation of a 46 kW PEM high pressure water electrolyzer, *Renew. Energy* 119 (2018) 160–173, <https://doi.org/10.1016/j.renene.2017.11.081>.
- [10] K. Onda, T. Murakami, T. Hikosaka, M. Kobayashi, R. Notu, K. Ito, Performance Analysis of Polymer-Electrolyte Water Electrolysis Cell at a Small-Unit Test Cell and Performance Prediction of Large Stacked Cell, *J. Electrochem. Soc.* 149 (8) (2002) A1069, <https://doi.org/10.1149/1.1492287>.

- [11] H. Takenaka, E. Torikai, Y. Kawami, N. Wakabayashi, Solid polymer electrolyte water electrolysis, *Int. J. Hydrogen Energy* 7 (5) (1982) 397–403, [https://doi.org/10.1016/0360-3199\(82\)90050-7](https://doi.org/10.1016/0360-3199(82)90050-7).
- [12] S. Stucki, G. Theis, R. Köt, H. Devantay, H.J. Christen, In Situ Production of Ozone in Water Using a Membrel Electrolyzer, *J. Electrochem. Soc.* 132 (2) (1985) 367–371, <https://doi.org/10.1149/1.2113840>.
- [13] S. Stucki, H. Baumann, H.J. Christen, R. Köt, Performance of a pressurized electrochemical ozone generator, *J. Appl. Electrochem.* 17 (4) (1987) 773–778, <https://doi.org/10.1007/BF01007814>.
- [14] L.M. Da Silva, L.A. De Faria, J.F.C. Boodts, Green processes for environmental application. electrochemical ozone production, *Pure Appl. Chem.* 73 (2001) 1871–1884, <https://doi.org/10.1351/pac200173121871>.
- [15] S. Stucki, D. Schulze, D. Schuster, C. Stark, Ozonization of purified water systems, *Pharm. Eng.* 25 (2005) 1–7.
- [16] Z. Zhang, G. Yi, P. Li, X. Wang, X. Wang, C. Zhang, Y. Zhang, Recent progress in engineering approach towards the design of PbO₂-based electrodes for the anodic oxidation of organic pollutants, *J. Water Process Eng.* 42 (2021) 102173, <https://doi.org/10.1016/j.jwpe.2021.102173>.
- [17] M. Rodríguez-Peña, J.A. Barrios Pérez, J. Lobato, C. Saez, C.E. Barrera-Díaz, M. A. Rodrigo, Scale-up in PEM electro-ozonizers for the degradation of organics, *Sep. Purif. Technol.* 284 (2022) 120261, <https://doi.org/10.1016/j.seppur.2021.120261>.
- [18] M. Paidar, V. Fateev, K. Bouzek, Membrane electrolysis—History, current status and perspective, *Electrochim. Acta.* 209 (2016) 737–756, <https://doi.org/10.1016/j.electacta.2016.05.209>.
- [19] A.A. Babak, R. Amadelli, A. De Battisti, V.N. Fateev, Influence of Anions on Oxygen/Ozone Evolution on PbO₂/spe and PbO₂/Ti Electrodes in Neutral pH Media, *Electrochim. Acta* 39 (11–12) (1994) 1597–1602, [https://doi.org/10.1016/0013-4686\(94\)85141-7](https://doi.org/10.1016/0013-4686(94)85141-7).
- [20] R. Amadelli, L. Armelao, A.B. Velichenko, N.V. Nikolenko, D.V. Girenko, S. V. Kovalyov, F.I. Danilov, Oxygen and ozone evolution at fluoride modified lead dioxide electrodes, *Electrochim. Acta* 45 (4–5) (1999) 713–720, [https://doi.org/10.1016/S0013-4686\(99\)00250-9](https://doi.org/10.1016/S0013-4686(99)00250-9).
- [21] M. Rodríguez-Peña, J.A. Barrios Pérez, J. Llanos, C. Saez, C.E. Barrera-Díaz, M. A. Rodrigo, Electrochemical generation of ozone using a PEM electrolyzer at acidic pHs, *Sep. Purif. Technol.* 267 (2021) 118672, <https://doi.org/10.1016/j.seppur.2021.118672>.
- [22] R. Amadelli, A.B. Velichenko, Lead dioxide electrodes for high potential anodic processes, *J. Serbian Chem. Soc.* 66 (11–12) (2001) 835–845, <https://doi.org/10.2298/JSC0112835A>.
- [23] R. Köt, S. Stucki, B. Carcer, Electrochemical waste water treatment using high overvoltage anodes. part I: physical and electrochemical properties of SnO₂ anodes, *J. Appl. Electrochem.* 21 (1991) 14–20.
- [24] H. Ito, T. Maeda, A. Nakano, H. Takenaka, Properties of Nafion membranes under PEM water electrolysis conditions, *Int. J. Hydrogen Energy* 36 (17) (2011) 10527–10540, <https://doi.org/10.1016/j.ijhydene.2011.05.127>.
- [25] P. Trinke, B. Bensmann, R. Hanke-Rauschenbach, Current density effect on hydrogen permeation in PEM water electrolyzers, *Int. J. Hydrogen Energy* 42 (21) (2017) 14355–14366, <https://doi.org/10.1016/j.ijhydene.2017.03.231>.
- [26] K. Schmidt-Rohr, Q. Chen, Parallel cylindrical water nanochannels in Nafion fuel-cell membranes, *Nat. Mater.* 7 (1) (2008) 75–83, <https://doi.org/10.1038/nmat2074>.
- [27] W.Y. Hsu, T.D. Gierke, Ion transport and clustering in nafion perfluorinated membranes, *J. Memb. Sci.* 13 (3) (1983) 307–326, [https://doi.org/10.1016/S0376-7388\(00\)81563-X](https://doi.org/10.1016/S0376-7388(00)81563-X).
- [28] C. Yin, J. Li, Y. Zhou, H. Zhang, P. Fang, C. He, Phase separation and development of proton transport pathways in metal oxide nanoparticle/nafion composite membranes during water uptake, *J. Phys. Chem. C* 122 (17) (2018) 9710–9717, <https://doi.org/10.1021/acs.jpcc.8b02535>.
- [29] M.B. Karimi, F. Mohammadi, K. Hooshyari, Recent approaches to improve Nafion performance for fuel cell applications: a review, *Int. J. Hydrogen Energy* 44 (54) (2019) 28919–28938, <https://doi.org/10.1016/j.ijhydene.2019.09.096>.
- [30] M. Schalenbach, Proton Conduction and Gas Permeation through Polymer Electrolyte Membranes during Water Electrolysis, *Forschungszentrum Jülich, Jülich*, 2018. <https://doi.org/10.18154/RWTH-2018-226600>.
- [31] J. Hu, H. Zhang, W. Xu, Z. Yuan, X. Li, Mechanism and transfer behavior of ions in Nafion membranes under alkaline media, *J. Memb. Sci.* 566 (2018) 8–14, <https://doi.org/10.1016/j.memsci.2018.08.057>.
- [32] R.A. Rozendal, H.V.M. Hamelers, C.J.N. Buisman, Effects of membrane cation transport on pH and microbial fuel cell performance, *Environ. Sci. Technol.* 40 (17) (2006) 5206–5211, <https://doi.org/10.1021/es060387r10.1021/es060387r.s001>.
- [33] K.J. Chae, M. Choi, F.F. Ajayi, W. Park, I.S. Chang, I.S. Kim, Mass transport through a proton exchange membrane (Nafion) in microbial fuel cells, *Energy and Fuels* 22 (1) (2008) 169–176, <https://doi.org/10.1021/ef700308u>.
- [34] C. Sun, J. Chen, H. Zhang, X.i. Han, Q. Luo, Investigations on transfer of water and vanadium ions across Nafion membrane in an operating vanadium redox flow battery, *J. Power Sources* 195 (3) (2010) 890–897, <https://doi.org/10.1016/j.jpowsour.2009.08.041>.
- [35] J.S. Lawton, A. Jones, T. Zawodzinski, Concentration dependence of VO₂⁺ crossover of nafion for vanadium redox flow batteries, *J. Electrochem. Soc.* 160 (4) (2013) A697–A702, <https://doi.org/10.1149/2.004306jes>.
- [36] C. Lutz, S. Hampel, X.i. Ke, S. Beuermann, T. Turek, U. Kunz, A. Guilherme Buzanich, M. Radtke, U.E.A. Fittschen, Evidence for redox reactions during vanadium crossover inside the nanoscopic water-body of Nafion 117 using X-ray absorption near edge structure spectroscopy, *J. Power Sources* 483 (2021) 229176, <https://doi.org/10.1016/j.jpowsour.2020.229176>.
- [37] M. Carmo, D.L. Fritz, J. Mergel, D. Stolten, A comprehensive review on PEM water electrolysis, *Int. J. Hydrogen Energy* 38 (12) (2013) 4901–4934, <https://doi.org/10.1016/j.ijhydene.2013.01.151>.
- [38] A. Kusoglu, A.Z. Weber, New insights into perfluorinated sulfonic-acid ionomers, *Chem. Rev.* 117 (3) (2017) 987–1104, <https://doi.org/10.1021/acs.chemrev.6b00159>.
- [39] R. Kodým, V. Fila, D. Šnita, K. Bouzek, Poisson–Nernst–Planck model of multiple ion transport across an ion-selective membrane under conditions close to chlor-alkali electrolysis, *J. Appl. Electrochem.* 46 (6) (2016) 679–694, <https://doi.org/10.1007/s10800-016-0945-1>.
- [40] R.R. Sijabat, M.T. de Groot, S. Moshtarikah, J. van der Schaaf, Maxwell-Stefan model of multicomponent ion transport inside a monolayer Nafion membrane for intensified chlor-alkali electrolysis, *J. Appl. Electrochem.* 49 (4) (2019) 353–368, <https://doi.org/10.1007/s10800-018-01283-x>.
- [41] B. Schwenzler, J. Zhang, S. Kim, L. Li, J. Liu, Z. Yang, Membrane development for vanadium redox flow batteries, *ChemSusChem* 4 (10) (2011) 1388–1406, <https://doi.org/10.1002/cssc.201100068>.
- [42] G.Q. Lu, F.Q. Liu, C.Y. Wang, Water transport through Nafion 112 membrane in DMFCs, *Electrochem. Solid-State Lett.* 8 (2005) 6–9, <https://doi.org/10.1149/1.1825312>.
- [43] Z. Zou, Y. Li, Z. Lu, D.a. Wang, Y. Cui, B. Guo, Y. Li, X. Liang, J. Feng, H. Li, C.-W. Nan, M. Armand, L. Chen, K. Xu, S. Shi, Mobile ions in composite solids, *Chem. Rev.* 120 (9) (2020) 4169–4221, <https://doi.org/10.1021/acs.chemrev.9b00760>.
- [44] J. Peng, M. Tian, N.M. Cantillo, T. Zawodzinski, The ion and water transport properties of K⁺ and Na⁺ form perfluorosulfonic acid polymer, *Electrochim. Acta* 282 (2018) 544–554, <https://doi.org/10.1016/j.electacta.2018.06.035>.
- [45] Gesetz über die Umweltverträglichkeit von Wasch- und Reinigungsmitteln (WRMG), 2017.
- [46] M. Ise, K.D. Kreuer, J. Maier, Electroosmotic drag in polymer electrolyte membranes: an electrophoretic NMR study, *Solid State Ionics* 125 (1–4) (1999) 213–223, [https://doi.org/10.1016/S0167-2738\(99\)00178-2](https://doi.org/10.1016/S0167-2738(99)00178-2).
- [47] T. Okada, G. Xie, O. Gorseth, S. Kjelstrup, N. Nakamura, T. Arimura, Ion and water transport characteristics of Nafion membranes as electrolytes, *Electrochim. Acta* 43 (24) (1998) 3741–3747, [https://doi.org/10.1016/S0013-4686\(98\)00132-7](https://doi.org/10.1016/S0013-4686(98)00132-7).
- [48] J. Peng, K. Lou, G. Goenaga, T. Zawodzinski, Transport properties of perfluorosulfonate membranes ion exchanged with cations, *ACS Appl. Mater. Interfaces* 10 (44) (2018) 38418–38430, <https://doi.org/10.1021/acsami.8b12403>.
- [49] T.A. Zawodzinski, M. Neeman, L.O. Sillerud, S. Gottesfeld, Determination of water diffusion coefficients in perfluorosulfonate ionomeric membranes, *J. Phys. Chem.* 95 (15) (1991) 6040–6044, <https://doi.org/10.1021/j100168a060>.
- [50] T.A. Zawodzinski, C. Derouin, S. Radzinski, R.J. Sherman, V.T. Smith, T. E. Springer, S. Gottesfeld, Water uptake by and transport through nafion® 117 membranes, *J. Electrochem. Soc.* 140 (4) (1993) 1041–1047, <https://doi.org/10.1149/1.2056194>.
- [51] B.S. Pivovar, W.H. Smyrl, E.L. Cussler, Electro-osmosis in nafion 117, polystyrene sulfonic acid, and polybenzimidazole, *J. Electrochem. Soc.* 152 (1) (2005) A53, <https://doi.org/10.1149/1.1827599>.
- [52] P. Berg, M. Stornes, Towards a consistent interpretation of electro-osmotic drag in polymer electrolyte membranes, *Fuel Cells* 16 (6) (2016) 715–724.
- [53] S. Feng, G.A. Voth, Proton solvation and transport in hydrated nafion, *J. Phys. Chem. B* 115 (19) (2011) 5903–5912, <https://doi.org/10.1021/jp2002194>.
- [54] T. Cantlay, D.J. Bain, J. Curet, R.F. Jack, B.C. Dickson, P. Basu, J.F. Stolz, Determining conventional and unconventional oil and gas well brines in natural sample II: cation analyses with ICP-MS and ICP-OES, *J. Environ. Sci. Heal. - Part A Toxic/Hazard. Subst. Environ. Eng.* 55 (1) (2020) 11–23, <https://doi.org/10.1080/10934529.2019.1666561>.
- [55] V.V. Rosen, O.G. Garber, Y. Chen, Magnesium deficiency in tap water in Israel: the desalination era, *Desalination* 426 (2018) 88–96, <https://doi.org/10.1016/j.desal.2017.10.027>.
- [56] P. Atkins, J. de Paula, Physical chemistry, 8th ed., Oxford University Press, 2006. [https://doi.org/10.1016/0016-0032\(53\)90803-5](https://doi.org/10.1016/0016-0032(53)90803-5).
- [57] M. Ozmaian, R. Naghdabadi, Modeling and simulation of the water gradient within a Nafion membrane, *Phys. Chem. Chem. Phys.* 16 (2014) 3173–3186, <https://doi.org/10.1039/c3cp54015d>.
- [58] T.Y. Chen, J. Leddy, Ion exchange capacity of Nafion and Nafion composites, *Langmuir* 16 (2000) 2866–2871, <https://doi.org/10.1021/la991094x>.
- [59] J. Zhu, J. Tan, Q. Pan, Z. Liu, Q. Hou, Effects of Mg²⁺ contamination on the performance of proton exchange membrane fuel cell, *Energy* 189 (2019) 116135, <https://doi.org/10.1016/j.energy.2019.116135>.
- [60] C. Agarwal, S. Chaudhury, A.K. Pandey, A. Goswami, Kinetic aspects of Donnan dialysis through Nafion-117 membrane, *J. Memb. Sci.* 415–416 (2012) 681–685, <https://doi.org/10.1016/j.memsci.2012.05.049>.
- [61] Y.-S. Ye, W.-Y. Chen, Y.-J. Huang, M.-Y. Cheng, Y.-C. Yen, C.-C. Cheng, F.-C. Chang, Preparation and characterization of high-durability zwitterionic crosslinked proton exchange membranes, *J. Memb. Sci.* 362 (1–2) (2010) 29–37, <https://doi.org/10.1016/j.memsci.2010.06.004>.
- [62] M. Asadi-Ghalhari, R. Aali, COVID-19: Reopening public spaces and secondary health risk potential via stagnant water in indoor pipe networks, *Indoor Built Environ.* 29 (8) (2020) 1184–1185, <https://doi.org/10.1177/1420326X20943257>.
- [63] L. Zlatanović, J.P. van der Hoek, J.H.G. Vreeburg, An experimental study on the influence of water stagnation and temperature change on water quality in a full-scale domestic drinking water system, *Water Res.* 123 (2017) 761–772, <https://doi.org/10.1016/j.watres.2017.07.019>.
- [64] T.H.J.A. Sleutels, H.V.M. Hamelers, R.A. Rozendal, C.J.N. Buisman, Ion transport resistance in microbial electrolysis cells with anion and cation exchange

- membranes, *Int. J. Hydrogen Energy* 34 (9) (2009) 3612–3620, <https://doi.org/10.1016/j.ijhydene.2009.03.004>.
- [65] E.A. Hernández-Pagán, N.M. Vargas-Barbosa, T. Wang, Y. Zhao, E.S. Smotkin, T. E. Mallouk, Resistance and polarization losses in aqueous buffer-membrane electrolytes for water-splitting photoelectrochemical cells, *Energy Environ. Sci.* 5 (2012) 7582–7589, <https://doi.org/10.1039/c2ee03422k>.
- [66] Ö.F. Selamet, F. Becerikli, M.D. Mat, Y. Kaplan, Development and testing of a highly efficient proton exchange membrane (PEM) electrolyzer stack, *Int. J. Hydrogen Energy* 36 (17) (2011) 11480–11487, <https://doi.org/10.1016/j.ijhydene.2011.01.129>.
- [67] P. Millet, N. Mbemba, S.A. Grigoriev, V.N. Fateev, A. Aukauloo, C. Etévant, Electrochemical performances of PEM water electrolysis cells and perspectives, *Int. J. Hydrogen Energy* 36 (6) (2011) 4134–4142, <https://doi.org/10.1016/j.ijhydene.2010.06.105>.
- [68] H.M. Rietveld, A profile refinement method for nuclear and magnetic structures, *J. Appl. Crystallogr.* 2 (1969) 65–71, <https://doi.org/10.1107/s0021889869006558>.

Danksagung

An allererster Stelle möchte ich mich bei Herrn Prof. Dr. Helmut Baltruschat dafür bedanken, dass Sie die Betreuung dieser Arbeit als Erstgutachter übernommen hat. Vielen Dank dafür, dass ich als externer Doktorand Teil dieser erfahrenen Arbeitsgruppe sein durfte und von diesem Erfahrungsschatz profitieren konnte. Ihre stete Bereitschaft zur Diskussion, Hilfestellung, aber auch Freiheit bei der Ausgestaltung ließen diese Arbeit erst gelingen.

Mein Dank gilt auch Herrn Prof. Dr. Klaus Günther für die Übernahme des Zweitgutachtens, den kreativen Input und Ihren unerschütterlichen Glauben an das Gelingen dieser Arbeit.

Bedanken möchte ich mich ebenfalls bei Frau Prof. Dr. Margit Schulze und Herrn Prof. Dr. Robert Glaum für ihren Einsatz, der Promotionskommission angehören zu wollen.

Ein besonderer Dank gebührt an dieser Stelle Dr. Samuel Stucki, der keine fachliche und noch so grundsätzliche Diskussion scheute und den Fortschritt dieser Arbeiten stets aufmerksam durch die Brille eines Referees betrachtete. Danke dir lieber Samuel, dass du mich auf diesem Weg begleitet hast und ich an deinem unerschöpflichen Erfahrungs- und Wissensschatz teilhaben durfte.

Ein großer Dank geht auch an Prof. Dr. Steffen Witzleben für die Vermittlung des Themas, den Zugriff auf weite Teile der Laborinfrastruktur und auch die Zusammenarbeit in der Lehre.

Dankeschön an meine ehemaligen Kollegen von der Hochschule Bonn-Rhein-Sieg: an Alex, Markus, Dominik, Katharina, Jessica, Tung, René, Jonas, Benedikt und ganz besonders Philipp. Ich danke euch für eine tolle Atmosphäre und tatkräftige Unterstützung im Laboralltag und auch die Zeit abseits der Arbeit. Danke auch an Esther und Johannes für euren Support in der Schlussphase der Arbeit!

Danke an Dirk Schulze von der Innovatec Gerätetechnik GmbH für die spontane Bereitstellung von Räumlichkeiten nach dem Hochwasser 2021, sodass ich meine experimentellen Arbeiten doch noch abschließen konnte. Danke an Daniel, Florian, Ph-e-lipp, Jonas und Henk, die mir die Zeit geschafft haben, um die Arbeit letztlich dann auch schreiben zu können. Danke auch an Kathi und Jo, die mir in der Schreibphase Arbeit abnehmen konnten und an alle anderen Kollegen der Innovatec, durch die ich jeden Tag Spaß an meiner Arbeit habe.

Nicht zuletzt gebührt absolute Dankbarkeit meiner Familie und Freunden für die permanente Unterstützung auf diesem Weg. Für die Geduld und auch Aufmunterung, als es nötig wurde. Danke, dass ihr an mich geglaubt habt.

Und am wichtigsten: Danke Marina! Danke dafür, dass du die Zeit hinter mir gestanden hast und mich zu jeder Zeit bedingungslos unterstützt hast!